Direct and Quantitative Absorptive Spectroscopy of Nanowires
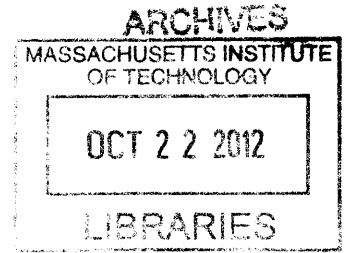
by

Jonathan Kien-Kwok Tong

Submitted to the Department of Mechanical Engineering in partial
fulfillment of the requirements for the degree of

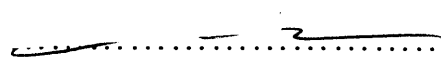Master of Science in Mechanical Engineering

at the

MASSACHUSETTS INSTITUTE OF TECHNOLOGY

September 2012

Author...
Department of Mechanical Engineering
August 7, 2012

Certified by...
Gang Chen
Carl Richard Soderberg Professor of Power Engineering
Thesis Supervisor

Accepted by...
David E. Hardt
Chairman, Department Committee on Graduate Students

Direct and Quantitative Absorptive Spectroscopy of Nanowires

by

Jonathan Kien-Kwok Tong

Abstract

Photonic nanostructures exhibit unique optical properties that are attractive in many different applications. However, measuring the optical properties of individual nanostructures, in particular the absorptive properties, remains a significant challenge. Conventional methods typically provide either an indirect or qualitative measure of absorption. The objective of this thesis is to therefore demonstrate a method capable of directly and quantitatively measuring the absorptive properties of individual nanostructures. This method is based on atomic force microscope (AFM) cantilever thermometry where a bimorph cantilever is used as a heat flux sensor. These sensors operate on the principle of a thermomechanical bending response and by virtue of their dimensionality, are capable of picowatt sensitivity. To validate the use of this technique, a single silicon nanowire is measured. By attaching a silicon nanowire to a cantilever and illuminating the sample with monochromatic light, the absolute absorptance spectrum of the nanowire was measured and shown to match well with theory. This spectroscopic technique can conceivably be used to measure even smaller samples, samples which cannot be characterized using conventional methods.

Thesis Supervisor: Gang Chen
Title: Carl Richard Soderberg Professor of Power Engineering

Acknowledgements

The fact that I'm writing these acknowledgements, which I've left as the very last thing to finish on this thesis, really comes as a bit of a shock. To think that not too long ago I thought this project was akin to putting a man on Mars really puts into perspective all the highs and lows I've experienced these past few years. And as I'm reminiscing, I can't help but think of all the individuals who have given me their support and encouragement to keep me going. Simply put, if it wasn't for these individuals, you (the reader) would not be here now reading this thesis.

That said I hope to include everyone who has helped me along the way. First I'd like to thank Prof. Gang Chen for the opportunity to work with him. His patience and guidance over these past few years were invaluable. I'd also like to thank Dr. Sheng Shen for his mentorship during my first year. He not only helped me get situated at MIT and the NanoEngineering group, but also passed on a great deal of his knowledge to me for this project. Speaking of which, I must also thank Poetro Sambegoro, Dr. Anastassios Mavrokefalos, Edi Hsu, Dr. Brian Burg and Dr. Sang Eon Han for all the help and discussion we've had to make this project work. I'd also like to thank Daniel Kraemer for his help in the integration of my setup into the vacuum system and his generosity in allowing me to monopolize the chamber for extended periods of time. In addition, I want to thank the pump-probe group (Dr. Austin Minnich, Kimberlee Collins, Maria Luckyanova, Lingping Zeng) for all the optics and equipment I've "borrowed" over the years. I would also like to thank Mr. Edward Jacobson who not only helped process my many purchase orders over the years, but also helped me get situated here at MIT. I'd also like to thank the NanoEngineering group as a whole. I couldn't have asked to work with a more humble, selfless group of labmates and officemates and for that, I'm quite grateful.

In addition, I'd like to thank Dr. Gregory McMahon at the Integrated Sciences Cleanroom and Nanofabrication Facility at Boston College for his help and encouragement over the many months and long hours I spent trying to attach a nanowire to a cantilever. I'd also like to thank Prof. George Barbastathis and his group for lending me some optics for the calibration experiments.

And last but not least, I'd like to thank my family and my friends for their enduring patience and support these past few years.

Table of Contents

List of Figures

into contact with the nanowire such that the tip of the nanowire is immersed in the glue. The glue is then cured by enlarging the beam spot size and increasing magnification. (d) The result after breaking the nanowire free from the wafer. (e) The cantilever is then coated with glue to attach the free end of the nanowire. (f) The nanowire is then carefully lowered until contact is made with the cantilever. The glue is once again cured. (g) To break the nanowire free, a second probe tip is used to shear the nanowire from the first probe tip. (h) An additional layer of glue is applied on top of the nanowire to ensure the nanowire is fully anchored to the cantilever. 74

List of Tables

Chapter 1

Introduction

The control of light has been a pursuit of many researchers over the years and has led to the development of many optics-based technologies such as fiber optics, energy efficient windows and solar cells. As these technologies continue to evolve, the need to more precisely engineer photonic nanostructures, structures which exhibit characteristic dimensions on the order of the wavelength of light or even smaller, is greater than ever. By designing structures at this scale, it is possible to manipulate optical properties to an extent previously inconceivable. In fact, recent studies have created structures which have demonstrated the possibility of optical cloaking, perfect lenses and optical computing.[1-5]

However, one of the biggest challenges in this field is measuring the broadband absorptive properties of individual structures. As will be discussed in Sec. 1.1, conventional spectroscopic techniques can only indirectly or qualitatively measure the spectral absorptance of such structures. The purpose of this thesis is to therefore demonstrate a method capable of directly and quantitatively characterizing the absorptive properties of individual nanostructures. This method is based on the use of atomic force microscope (AFM) cantilever thermometry. Although the measurement platform can be used to characterize a variety of photonic structures, we strictly focus on silicon nanowires due to their relative ease of measurement and potential impact.

1.1 Background on Particle Measurements

1.1.1 Definitions

In this study, the spectral absorptivity of an individual structure is characterized by its absorption efficiency. The absorption efficiency is a normalized representation of the effective absorption cross section viewed by the light source. Since this parameter is wavelength dependent, the following can be written,

$$Q_{abs}(\lambda) = \frac{C_{abs}(\lambda)}{G}$$ (1.1)

where Q_{abs} is the absorption efficiency, C_{abs} is the absorption cross section and G is the geometric cross section in the direction perpendicular to the incident radiation. In addition, we can also define the scattering efficiency in the same manner,

$$Q_{sca}(\lambda) = \frac{C_{sca}(\lambda)}{G}$$ (1.2)

where Q_{sca}, the scattering efficiency, is also the effective scattering cross section of the particle viewed by the light source. The sum of these two quantities is called the extinction efficiency,

$$Q_{ext}(\lambda) = Q_{abs}(\lambda) + Q_{sca}(\lambda)$$ (1.3)

which represents the absorbed and scattering losses from the incident field due to the presence of the particle. The parameters in (1.1-1.3) will be derived from Mie theory in much greater detail in Ch. 2. The purpose of introducing these parameters now is to provide some context for the previous techniques that have been used to measure these efficiencies.

1.1.2 Nephelometry

The motivation behind the optical characterization of micro and nanostructures, namely particulates of varying shapes and sizes with a characteristic length on the order of microns and nanometers, has evolved over the past several decades and so too the methods employed in these measurements. Perhaps the oldest and most well known technique is nephelometry which has been used extensively since the 1970's to characterize particulates either in a gas or a liquid. The concept of nephelometry is based on the measurement of scattered light spectra from a suspended particle or stream of particles illuminated by a light source. In this method the scattering and extinction efficiency can be quantitatively measured. The scattering efficiency can be measured by summing the intensities of the scattered light at all angles around the particle. To measure the extinction efficiency, the optical theorem is used which states that only the intensity in the shadow of the particle needs to be measured. It is in this manner that the absorption efficiency can be determined from (1.3).[6]

This technique has primarily found use in the detection of aerosols and other pollutants for air quality characterization. However, several studies have been conducted on single particles

to confirm the results obtained by Mie theory. In 1970, Phillips *et al.* utilized this technique to measure the refractive index and diameter of single polystyrene spheres.[7] Polystyrene spheres were specifically chosen due to their use as light scattering standards at the time. The diameter chosen ranged from 400 to 4000 nm. The spherical particles were nebulized from a water suspension when introduced into the system so that the particles retain a charge. They were then held in position via an electric field and illuminated by a pulsed argon ion laser (514.5 nm). Although in this study they do not explicitly calculate the efficiencies, since their intention was to demonstrate the accuracy of this method in sizing the individual particles, they nonetheless obtain the scattering intensity as a function of the scattered angle. They then utilize Mie theory to fit these results to back out the refractive index and diameter (1099 nm) to within 1% error.

In 1976, Marshall *et al.* improved this method by enabling the rapid measurement of the full 360° light scattering pattern.[8] Their system utilized a rotating aperture at 3600 rpm to measure the pattern in less than 20 ms which meant that the particles themselves no longer needed to be suspended. They once again measured the refractive index and diameter of polystyrene spheres, which flowed through the system in an aerosol stream. Here they illuminated the particles with a He-Ne laser (632.8 nm) and were able to observe very sharp resonance peaks as predicted by Mie theory. In 1980, Bartholdi *et al.* constructed an alternate system that utilized an array of photodetectors to rapidly measure the scattering pattern of individual polystyrene particles for size analysis.[9]

In 1981, Schuerman *et al.* conducted a more systematic study to assess the validity of Mie theory for different particle shapes.[10] To facilitate control over the particle shape, a microwave analog was used which enabled the researchers to use particles with dimensions on the order of centimeters. The particles studied consisted of spheres, cylinders, prolate spheroids, oblate spheroids and disks made from polymethyl methacrylate (PMMA) which has a refractive index in the microwave wavelength range similar to silicates in the optical wavelength range. These particles were illuminated by 3.18 cm radiation. The results presented in this work were averaged over all particle orientations. To determine the extinction and scattering cross sections, the researchers measured the Stokes vector, which requires measuring the intensity of the scattered light at different incident polarizations. The results for the spheres and cylinders were fitted using Mie theory while the other particle shapes required a separate calculation. It was thus

shown that for nonspherical particles, the true size of the particles was significantly underestimated when using Mie theory for data fitting.

Overall these methods were shown to exhibit exceptional accuracy with relative errors well within 10%. Experimentally, this is due to the use of a high intensity laser as this leads to a strong scattering response. Furthermore, the size and refractive index of the particles were obtained by fitting the scattering response to theory. For these particles, the scattered intensity as a function of the scattering angle was generally a smooth, slowly changing curve. Therefore, fitting naturally smeared out any variations exhibited during experiment. By contrast, in the present study, a broadband light source in the visible wavelength range is used. These sources generally exhibit a lower intensity which inherently makes measurements on individual particles more challenging. In addition, the method used will not require any fitting.

As one can clearly see, the majority of the studies conducted in this era were motivated by applications aimed towards the detection of particles, such as the presence of aerosol particulates. More recently, the focus has shifted towards the study of highly confined optical modes and resonant effects in these particles, as will be discussed in the next section.

1.1.3 Current Methods

The study of highly confined optical modes and resonant modes has attracted substantial attention recently due to their potential to significantly enhance the absorption efficiency of particles. In brief, this enhancement originates from the coupling of light to modes supported by the particle. This includes highly confined optical modes, phonon polariton modes and plasmon polariton modes. When light couples to these modes, an electromagnetic field is created within the particle that extends beyond its boundaries; hence, these modes are referred to as leaky mode resonances. The resulting interaction of this leaky field with incoming light can lead to interference effects which produce scattering and absorption efficiencies greater than 1, i.e. the effective cross section viewed by the light source is much larger than the geometric cross section. For many materials, these modes exist in the visible and infrared wavelength spectrum which is useful for many applications, as will be discussed in Sec 1.2.

In many of these studies, a dark-field illumination scheme is used which is once again based on the concept of measuring scattered light spectra to determine the extinction and scattering efficiencies. Dark-field illumination is a common technique to image samples where

the unscattered beam is excluded from the final image. Since the image is formed by scattered light only, this image can be analyzed spectrally to obtain the extinction and scattering efficiencies.

In 2002, Sönnichsen et al. used this method to study the reduction of plasmon damping in gold nanoparticles.[11] A conventional optical microscope with a high aperture dark-field condenser, an oil immersion objective and a halogen lamp as the light source is used to clearly distinguish individual gold nanoparticles on a substrate. The scattered light from individual particles is then focused onto an entrance slit of a spectrometer where a CCD camera is used as the detector. Based on the scattered spectra from a single particle, they were able to measure the plasmon resonance peak for single gold nanosphere and nanorod. By assessing the strength and the shape of peak, they were able to determine that nanorods exhibit a much greater reduction in plasmon damping resulting in a higher scattering efficiency. In 2003, McFarland et al. studied the shift in the plasmon resonance when a self-assembled monolayer is formed onto a single silver nanoparticle.[12] It was shown that the absorption of less than 60,000 adsorbate particles on the silver nanoparticle led to a shift in the plasmon wavelength of 40.7 nm in real-time. In 2004, Nehl et al. studied the scattering spectra of gold nanoshells using a scanning electron microscope (SEM) and atomic force microscopy (AFM) to confirm that Mie theory can be used to fit this data.[13] From this study they were able to support the assertion that the broadening of the plasmon resonance is due to inhomogeneous broadening from variations in particle size and shape. In 2006, Nehl et al. also conducted a study on star-shaped gold nanoparticles which showed the presence of multiple plasmon resonances corresponding to the different tips of the nanoparticle.[14] As a result, this particle exhibited polarization dependent multidirectional scattering spectra which the authors postulate could be used to determine the three-dimensional orientation of the particles. In 2010, Brönstrup et al. measured the scattering and absorption efficiencies of silicon nanowires as a function of the polarization and incident angle of the illuminating light source as well as the size of the nanowires.[15] It was shown that the absorption efficiencies are stronger for TM polarization when the wire diameter is less than 160 nm. The behavior is opposite for thicker nanowires. In addition, the incident angle of the illuminating light source did not significantly deviate from measurements at normal incidence. In 2011, Cao et al. followed up this work with a study on the coupling effects between adjacent silicon nanowires.[16] It was shown that these coupling effects are substantially stronger

compared to coupled microresonators resulting in strong scattering peaks as the spacing between the wires was reduced.

The methods discussed thus far have comprised a family of techniques that enable the indirect, yet quantitative measure of the absorption efficiency on individual particles. Alternatively, several studies have also been conducted that directly, yet qualitatively measure the absorption efficiency of individual semiconductor nanowires. In 2009 and 2010, Cao et al. measured the photocurrent generated by silicon and germanium nanowires when illuminated by monochromatic light in the visible wavelength spectrum.[17, 18] To measure the photocurrent response, an individual nanowire was placed onto an insulating substrate. Two electrical contacts were then deposited on both ends of the nanowire made from aluminum and platinum to form an Ohmic contact and Schottky contact, respectively. This asymmetric configuration provided a built-in potential to drive photoexcited carriers and also suppressed the effects of dark-field current in the measurement. Based on their measured photocurrent spectra, they were able to correlate their results with Mie theory which showed good agreement in predicting distinct optical features for different size nanowires.

Although not directly related, it should not go without mention that photoluminescence and Raman spectroscopy measurements are also commonly used to characterize the emissive properties of individual nanostructures by probing the electronic structure of the material. Ng et al. and Yang et al. both characterized ZnO nanowires excited using a He-Cd laser as a function size, crystallinity and growth conditions.[19, 20] Ng et al. measured the resulting emission using a UV resonant Raman spectrometer and Yang et al. near-field scanning optical microscope. Gudiksen et al. conducted a similar study on superlattice nanowires made from II-V and IV materials.[21] Qi et al., Sham et al. and Cao et al. conducted studies on silicon nanowires.[22-24] Cao et al. also included measurements on silicon nanocone structures. Qi et al. excited the samples using a XeCl laser and measured the resulting photoluminescence using a CCD camera. Sham et al. conducted a soft x-ray excited optical luminescence excitation and measured the emission with an x-ray emission spectrometer. Cao et al. also utilized a Raman spectrometer and modeled the scattered emission based on Mie theory. More recently, Laffont et al. measured the intrinsic electrical conductivity of gold and nickel nanowires using electron energy loss spectroscopy using scanning transmission electron microscopy.[25]

To summarize, current methods either provide an indirect and quantitative measurement or direct and qualitative measurement of absorption. This is indicative of the difficulty inherent in absorption measurements. However, as will be shown in this study, the use of cantilever thermometry can circumvent these limitations. This method is believed to be the only method available to directly and quantitatively measure the absorptive properties of nanostructures.

1.1.4 Cantilever Thermometry

In this study, we use a different approach based on AFM cantilever thermometry. Beginning in the mid-90's and onwards, the use of AFM bimorph cantilevers as a measurement platform has continually grown due to the robustness and high sensitivity characteristics when used as a sensor.[26] This has been primarily motivated by physical, biological and chemical sensing applications. Though perhaps not as prevalent as the aforementioned fields, AFM cantilevers have also found a niche in thermal sensing applications. In 1994, Gimzewski *et al.* originally used a bimorph cantilever as a calorimeter to sense the catalytic conversion of H_2+O_2 to H_2O by measuring fluctuations in heat flow via oscillations in the cantilever.[26] In this work, they were able to achieve a temperature sensitivity of 10^{-5} K and a power sensitivity of 1 nW by simply using an AFM head as their measurement platform. This was followed in 1994 by Barnes *et al.* who made numerous modifications to the measurement platform, including the introduction of a light source and a lock-in amplifier, to create the first photothermal detector based on the bimorph principle.[27, 28] In their work, they were able to achieve a power resolution as low as 100 pW. In 1997, Lai *et al.* and Varesi *et al.* further optimized this measurement platform and the design of the cantilever, achieving a power sensitivity of 50 pW and temperature sensitivity of 10^{-6} K.[29, 30] More recently, in 2005, LeMieux *et al.* developed a polymer-silicon cantilever with a thermal sensitivity one order of magnitude higher than standard metallic-silicon cantilevers.[31] In 2008, Shen *et al.* introduced a clever method to directly measure the thermal conductance of a bimorph cantilever. This enabled the simultaneous measurement of temperature and heat flux at the tip.[32] In 2011, Narayanswamy *et al.* further showed that it is possible to measure the heat transfer coefficient ($h = 3400$ W/m^{2}K) when the cantilever is operated in air.[33] Most recently, Sadat *et al.* designed an optimized cantilever with a power resolution as low as 4 pW, which is currently the highest sensitivity reported.[34]

The continual advancement of bimorph cantilevers as thermal sensors has also brought forth numerous applications. In 1994, Nakabeppu *et al.* used a bimorph cantilever to conduct scanning thermal imaging of surfaces with submicron resolution via heat conduction from the surface to the AFM tip.[35] In 1996, Berger *et al.* physically attached a solid mass of n-alkane (C_nH_{2n+2}) to the cantilever and then locally heated the sample using a heater to measure the enthalpy of the phase transition of the material.[36] In 2000, Li *et al.* used a multilayer reed, which is essentially a larger cantilever, as a photothermal chemical detector.[37] A chemically selective layer is used as a substrate to deposit thin-films of specific chemicals. The absorptance spectrum can then be measured by illuminating the sample with different wavelengths of light. In 2002, Zhao *et al.* developed an IR imaging system based on an array of cantilevers which functioned as individual pixels.[38] More recently in 2008, Narayanaswamy *et al.* utilized a bimorph cantilever to measure the near-field radiative transfer between two objects placed in close proximity.[39] This work demonstrated that near-field radiative transfer can exceed Planck's blackbody limit. In 2010, Shen *et al.* used a bimorph cantilever to measure the thermal conductivity of individually drawn polyethylene nanofibers.[40] It was demonstrated that the thermal conductivity of polyethylene could be as high as 104 W/mK. In 2010, Kjoller *et al.* utilized a unique measurement setup based on atomic force microscopy that allowed the simultaneous measurement of thermal and mechanical properties for a thin-film illuminated by infrared radiation.[41] In addition, Kwon *et al.* conducted a study to assess the sensitivity of various commercial cantilevers in application to infrared spectroscopy.[42] This was followed in 2012 by another study from Kwon *et al.* which looked into the dynamic thermomechanical response of a bimaterial cantilever under periodic heating conditions.[43]

Given the versatility and high sensitivity of these cantilever sensors, the work presented in this thesis will be based on a configuration where an AFM bimorph cantilever is used as a photothermal detector. The idea is to use the cantilever to directly and quantitatively measure the radiative energy absorbed by a micron or even nanometer sized particle when illuminated by monochromatic light. Further discussion will be provided in Ch. 3.

1.2 Applications of Particles

The evolution of the measurement techniques employed to characterize the optical properties of individual nanostructure has coincided with a shift in the intended applications of these studies.

Whereas the studies from decades earlier were motivated by the detection of particulates in air, recent work has been motivated by the optimization and use of the enhanced optical properties observed in these individual nanostructures. In particular, semiconductor nanostructures have drawn significant interest due to both the optical properties, as mentioned, as well as the electronic properties which can be tailored for different applications. Despite being a bit dated, Law *et al.* provides a nice review of the various methods for fabrication and property characterization as well as a variety of applications where such materials could find use.[44] Although the applications of these materials are numerous, a brief review of some of these technologies will be discussed.

In the microelectronics industry, silicon is the most widely used material due its performance and abundance. However, in photonics applications, the indirect bandgap of silicon has limited its use due to its poor absorptive properties. But, as discussed in Sec. 1.1, the nanostructuring of many materials, including silicon, can lead to dramatic improvement in the optical properties. Cao *et al.* utilized this behavior to demonstrate the color tunability of silicon nanowires.[45] Since resonant scattered light is a strong function of size, changing the diameter of the wire can shift the wavelength of the scattered light across the entire visible wavelength spectrum. Therefore, silicon nanowires can be used strictly as a scatterer of white light which would be useful in a variety of display technologies. Alternatively, Huang *et al.* proposed the integration of silicon nanowires in conjunction with III-V and II-VI nanowires to form a nanoLED constructed from a bottoms up approach.[46] The motivation for this is to combine materials and structures which are typically incompatible using conventional fabrication techniques. Here, the silicon nanowires are p-type and the other direct band gap materials are n-type thus forming a junction. As a result, the n-type nanowires function as the emitters. Despite the complexity, the small footprint of these nanoLEDs can be useful in many applications such as high density optical storage, lab-on-a-chip systems and chemical/biological analysis.

Perhaps one of the more sought after applications is in photovoltaic cells where the enhanced optical properties of semiconductor nanostructures could provide improved efficiency with lower material usage. Several studies have been conducted where vertically oriented silicon nanowire arrays were used for light trapping. Hu *et al.* conducted a theoretical analysis on the optical absorption a periodically arranged silicon nanowire array.[47] It was shown that at moderate filling ratios, the array exhibited enhanced absorption at high frequencies. At lower

frequencies, the absorption was worse than a thin film. Given that the structure studied was unoptimized, the ultimate efficiency only approached that of a thin film. However, more recently, Huang et al. conducted a more systematic study that optimized the nanowire array.[48] By optimizing the spacing and the diameter at a given length, it was shown that the ultimate efficiency can exceed a thin film for several materials from 100 nm to 100 μm. Tsakalakos et al. experimentally measured the optical properties of silicon nanowires synthesized by both chemical vapor deposition and wet etching using an integrating sphere spectrometer.[49] It was shown that the absorption across the entire solar spectrum was improved compared to a thin film of equivalent thickness. Tian et al. coated a single doped silicon nanowire with silicon shell to form a p-n junction which was then connected in series to an electrical to power a logic gate.[50] Garnett et al. coated a doped silicon nanowire array with a doped silicon shell to form a p-n junction.[51] Despite the enhancement in absorption, surface recombination limited the device performance. Furthermore, Baxter et al. also used ZnO nanowires to create a dye-sensitized solar cell where the nanowires replaced conventional TiO2 nanoparticles.[52] These nanowires were coated with dye thus function as both the absorber and a conduction path for electrons to migrate across the cell.

The use of semiconductor nanowires has also found application in the development of new photodetectors. As mentioned in Sec 1.2, Cao et al. developed a platform to measure the photocurrent generated by a single nanowire when illuminated by light.[17, 18] This platform is, in essence, a photodetector. Once again, the small footprint of the device and its polarization dependent optical properties lends itself to lower cost and new applications. VJ et al. provides a nice review on this subject matter.[53]

1.3 Objectives

The objective of this work is to experimentally measure the absorption efficiency of an individual silicon nanowire directly and quantitatively. This will be achieved by illuminating a nanowire with monochromatic light at various wavelengths and measuring the heat absorbed by the nanowire using an AFM bimorph cantilever as a photothermal detector. Theoretical results obtained by Mie theory will be used to validate experimental results. Ultimately, the goal is to demonstrate that this platform will provide a new means of probing the unique optical properties of various nanostructures to an extent previously unattainable with conventional methods.

1.4 Organization of Thesis

In this thesis, the hope is to provide a comprehensive picture of the project which includes the theoretical foundation from which this study is based off of and the measurement technique employed to measure the spectral absorption efficiency of individual. Therefore, Chapter 2 will consist of a complete derivation of Mie theory for infinitely long cylinders in addition to theoretical results for the particular case of a silicon nanowire. In Chapter 3, an overview of the experiment will be provided including the synthesis of nanowires, sample fabrication, the experimental setup and the various calibrations needed to extract absorptivity data. Chapter 4 will provide a discussion on experimental results including additional modifications to the theory to account for experimental limitations. And finally, Chapter 5 will summarize the results in this study and provide an outlook on future work in this field.

Chapter 2

Theoretical Background

The theoretical foundation for this study is based on examining the interaction of electromagnetic waves with a freely suspended particle. In this chapter, the theoretical solutions to the absorption efficiency for an infinitely long cylinder illuminated by a monochromatic plane wave will be derived. This derivation constitutes the well-known Mie theory, aptly named after Gustav Mie and his seminal work in 1908 on electromagnetic scattering by small particles.[54] In the interest of providing future readers a complete understanding of the theory, a full derivation will be conducted. Then, a solution will be presented for the specific case of a Si nanowire followed by an analysis detailing its unique optical characteristics.

2.1 Mie Theory

The theoretical basis for particles exhibiting strong optical absorption is evident when considering spherical particles operating in the Rayleigh limit.[6, 55] In this limit, the characteristic length of the particle is much smaller than the wavelength of the incident field. The absorption efficiency can be approximated to be,

$$Q_{abs} \cong 4x\mathrm{Im}\left(\frac{\varepsilon-1}{\varepsilon+2}\right); \text{ for } x = ka \ll 1 \qquad (2.1)$$

where x is the size parameter, k is the wave vector, a is the particle radius and ε is the dielectric permittivity. From (2.1), we can clearly see that when the real part of the permittivity is equal to -2, the absorption efficiency will be strongly enhanced. The frequency at which this occurs is known as the Fröhlich frequency. However, the efficiency will not diverge to infinity for real materials as (2.1) may suggest due to finite damping from the imaginary component in the dielectric permittivity. Nonetheless, many real materials, including both metals and insulators do exhibit absorption efficiencies greater than 1 at certain frequencies.

This optical phenomenon originates from the coupling of light at a frequency matching electromagnetic modes supported by the particle. The fields generated by this coupling can

extend beyond the boundaries of the particle, making them leaky. There are several types of leaky modes as briefly mentioned in Ch. 1, Sec. 1.1.3. Highly confined optical modes are analogous to modes supported in optical fibers and microresonators.[17] The existence of these modes can be determined based on classical waveguide theory where certain conditions on the radius and the dielectric constants must be satisfied. Another type of leaky mode is based on the coupling of light to the charge carriers (electrons and ions) in the material. This mode coupling is known as either a plasmon polariton or phonon polariton for electrons and phonons, respectively. In general, these modes exist as surfaces waves which decay over short distances. However, when these surface waves are confined within a nanoparticle or nanowire, the charge carriers will resonate with the incident field, resulting in a radiating dipole-like field at the same frequency. For electrons, this characteristic frequency typically occurs in the ultraviolet regime. Likewise, for ions exhibiting lattice vibrations, or phonons, such frequencies are generally in the infrared regime due to the higher mass of the ions. Generally, these frequencies are shape dependent. For example the surface plasmon frequency will differ for a flat plate and a sphere by factors of $\sqrt{2}$ and $\sqrt{3}$, respectively.[6] The resulting interference between the leaky field and the incident field can cause a concentrating effect where the energy of the surrounding field, the Poynting vector, is redirected towards the particle. This is shown visually in Fig. 2.1,
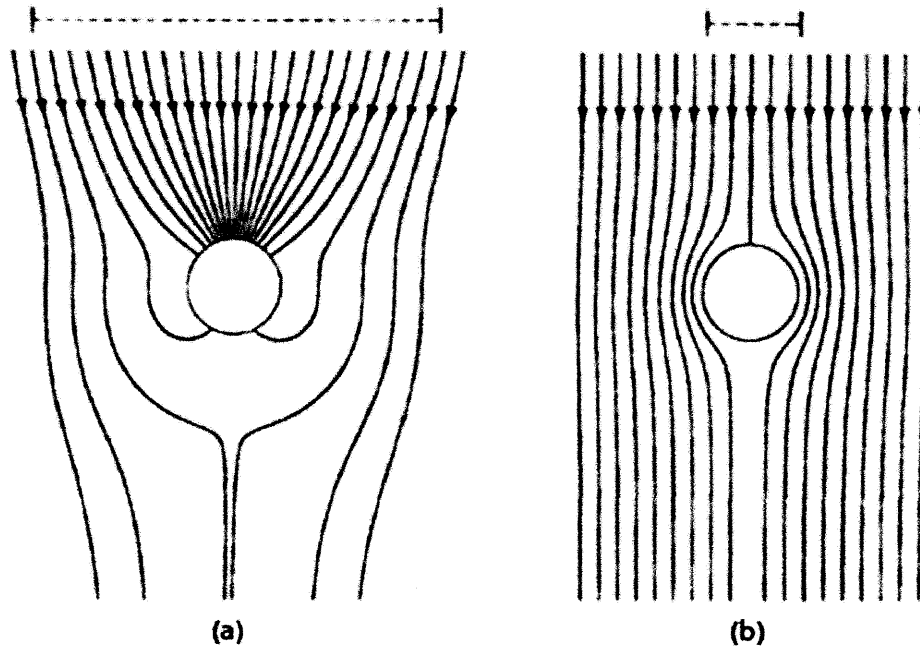
Figure 2.1: (a) The Poynting vector field distribution when the particle is illuminated by light corresponding to the resonant frequency. (b) The Poynting vector field distribution when the particle is illuminated by light at an off-resonant frequency. The dashed line corresponds to the effective absorption cross section of the particle.

In our definition of efficiency, we always normalize with respect to the incident geometric cross section. Therefore, if such a concentrating effect is present, the absorption efficiency will naturally be greater than 1.

In this project, we use the more general Mie theory to study infinitely long cylinders with an arbitrary size parameter to determine the regions of interest, as a function of both the wavelength of light and the particle radius, where such enhancement may be observed without the limitations imposed by the Rayleigh approximation. Thus, the remainder of Sec. 2.1 is devoted to the derivation of the Mie theory efficiencies and Sec. 2.2 will provide a discussion on theoretical results for silicon nanowires. However, given the inherent complexity in the mathematics of Mie theory, it would first be pertinent to outline the steps in this derivation so as to avoid becoming lost in a myriad of formulas. Note that for the remainder of the chapter, the wavelength of light will be used rather than the frequency. The following derivation can also be found in Bohren and Huffman.[6]

2.1.1 Outline of Derivation for an Infinitely Long Cylinder

To begin, a harmonic plane wave is incident on an infinitely long cylinder suspended in vacuum as shown in Fig. 2.2,
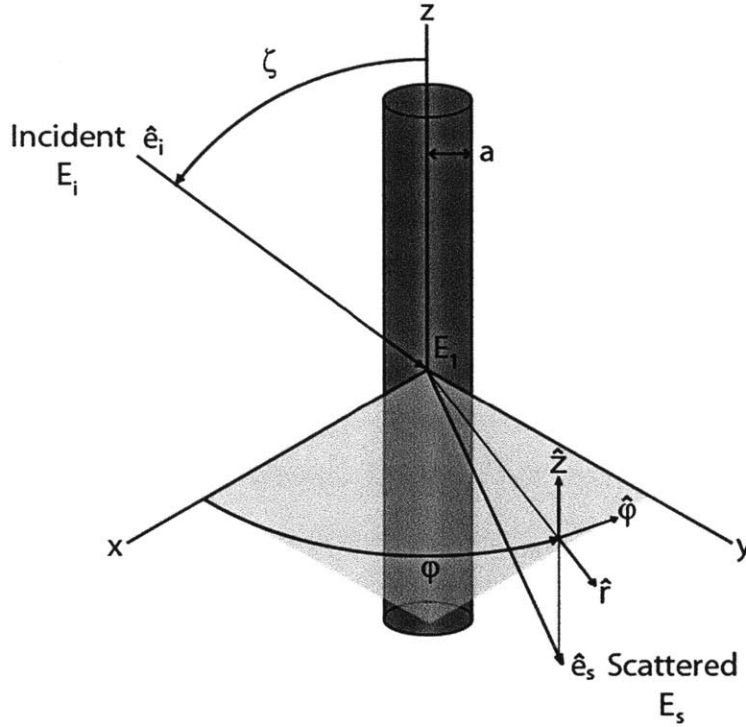
Figure 2.2: Definition of fields, geometry and coordinate system used in the analysis. Note the scattered field is treated separately. Subsequent interference with the incident field will be accounted for when calculating the Poynting vector.

where $\mathbf{E_1}$ is the field inside the particle, $\mathbf{E_i}$ is the incident field, $\mathbf{E_s}$ is the scattered field, a is the radius of the cylinder, φ is the azimuthal angle and ζ is the polar angle of incidence relative to the cylinder axis. Note that we take $\mathbf{E_2}$, the field in the medium surrounding the particle, to be the superposition of the incident and scattered fields,

$$\mathbf{E}_2 = \mathbf{E}_i + \mathbf{E}_s \tag{2.2}$$

$$\mathbf{H}_2 = \mathbf{H}_i + \mathbf{H}_s \tag{2.3}$$

Because the object in question is a cylinder, there will be a polarization dependence on the efficiencies. Two incident fields must therefore be defined in order to account for all relevant polarization states. For convenience, we choose these incident fields to be either parallel or

perpendicular with the cylinder axis. Harmonic plane waves are more naturally represented in Cartesian coordinates, thus,

$$\mathbf{E}_{i,I} = E_0 \left(\sin\zeta\, \hat{\mathbf{z}} - \cos\zeta\, \hat{\mathbf{x}} \right) e^{-ik(r\sin\zeta\cos\varphi + z\cos\zeta)} \tag{2.4}$$

$$\mathbf{E}_{i,II} = E_0\, \hat{\mathbf{y}}\, e^{-ik(r\sin\zeta\cos\varphi + z\cos\zeta)} \tag{2.5}$$

Here we use I to denote parallel polarization and II to denote perpendicular polarization. The components in the propagation direction in (2.4) and (2.5) are merely projections onto the x-z plane in a cylindrical coordinate system. To convert the polarization components from Cartesian coordinates to cylindrical coordinates, we use the unit vector definitions,

$$\hat{\mathbf{x}} = \cos\varphi\, \hat{\mathbf{r}} - \sin\varphi\, \hat{\boldsymbol{\varphi}}$$

$$\hat{\mathbf{y}} = \sin\varphi\, \hat{\mathbf{r}} + \cos\varphi\, \hat{\boldsymbol{\varphi}}$$

$$\hat{\mathbf{z}} = \hat{\mathbf{z}}$$

Thus, (2.4) and (2.5) become,

$$\mathbf{E}_{i,I} = E_0 \left(-\cos\zeta\cos\varphi\, \hat{\mathbf{r}} + \cos\zeta\sin\varphi\, \hat{\boldsymbol{\varphi}} + \sin\zeta\, \hat{\mathbf{z}} \right) e^{-ik(r\sin\zeta\cos\varphi + z\cos\zeta)} \tag{2.6}$$

$$\mathbf{E}_{i,II} = E_0 \left(\sin\varphi\, \hat{\mathbf{r}} + \cos\varphi\, \hat{\boldsymbol{\varphi}} \right) e^{-ik(r\sin\zeta\cos\varphi + z\cos\zeta)} \tag{2.7}$$

In the following sections, all derivation will be done only for case I. A summary of the results for case II will be presented in Sec. 2.1.7. We emphasize here that the mathematics will differ slightly between both cases, however the methodology will remain the same.

Given the complex nature of the mathematics involved in the derivation, the following sections are structured to emphasize the overarching steps taken in this derivation. Sec. 2.1.2 first provides a brief review of the electromagnetics relevant to this derivation. Sec. 2.1.3 discusses the derivation of the vector harmonics which will be used as a new basis to express all field solutions in the problem. As will be shown, use of these harmonics will drastically simplify the problem. Sec. 2.1.4 discusses the form and the expansion of the fields in terms of the vector harmonics. Sec. 2.1.5 utilizes the expanded forms of the fields in the system and applies boundary conditions to solve all field solutions. And finally, Sec. 2.1.6 will discuss the derivation of the efficiencies from the field solutions derived in Sec. 2.1.5.

30

2.1.2 Review of Electromagnetic Theory

Maxwell Equations

Before delving into the mathematical details of the derivation, it would be worthwhile to first provide a brief review of electromagnetic theory relevant to the problem at hand. As mentioned in the previous section, a macroscopic approach is taken in describing light interacting with a particle. Appropriately, we begin with the macroscopic Maxwell equations,

$$
\begin{aligned}
\nabla \cdot \mathbf{D} &= \rho \\
\nabla \cdot \mathbf{B} &= 0
\end{aligned}
\quad ; \text{Gauss's Law} \tag{2.8}
$$

$$
\nabla \times \mathbf{E} = -\frac{\partial \mathbf{B}}{\partial t} \quad ; \text{Faraday's Law} \tag{2.9}
$$

$$
\nabla \times \mathbf{H} = \mathbf{J} + \frac{\partial \mathbf{D}}{\partial t} \quad ; \text{Ampere's Law} \tag{2.10}
$$

where $\mathbf{D}$ is the electric displacement, $\mathbf{E}$ is the electric field, $\mathbf{B}$ is the magnetic induction, $\mathbf{H}$ is the magnetic field, ρ is the charge density and $\mathbf{J}$ is the current density. We can further relate the field parameters using the constitutive relations,

$$
\begin{aligned}
\mathbf{D} &= \varepsilon_P \mathbf{E} \\
\mathbf{B} &= \mu \mathbf{H} \\
\mathbf{J} &= \sigma \mathbf{E}
\end{aligned} \tag{2.11}
$$

where ε_P is the dielectric permittivity which includes the polarizability, μ is the magnetic permeability, and σ is the electrical conductivity. In general, these phenomenological coefficients are a tensor. However, for this analysis, we assume these phenomenological coefficients are field independent (the medium is linear), independent of position (the medium is homogeneous) and independent of direction (the medium is isotropic). Since the current density is a function of the electric field, the permittivity can be written to include the electrical conductivity as an imaginary term.[6, 56] This will be shown in the following section when using harmonic representation for the fields. For simplicity we assume the system is charge free ($\rho = 0$).

31

Time Harmonic Fields

In this analysis, we make use of time harmonic fields of the form,

$$\mathbf{E} = \mathbf{E}_0\, e^{i\mathbf{k}\cdot\mathbf{x}-i\omega t}$$
$$\mathbf{H} = \mathbf{H}_0\, e^{i\mathbf{k}\cdot\mathbf{x}-i\omega t} \tag{2.12}$$

If we use the fields in (2.12), substitute in the constitutive relations (2.11) and assume a source-free system, the Maxwell equations (2.8-2.10) become,

$$\nabla\cdot\mathbf{E} = 0 \tag{2.13}$$

$$\nabla\cdot\mathbf{H} = 0 \tag{2.14}$$

$$\nabla\times\mathbf{E} = i\omega\mu\,\mathbf{H} \tag{2.15}$$

$$\nabla\times\mathbf{H} = -i\omega\varepsilon\,\mathbf{E} \tag{2.16}$$

where ε is the complex permittivity,

$$\varepsilon = \varepsilon_P + i\frac{\sigma}{\omega}$$

Now if we take the curl of (2.15) and (2.16) using the identity,

$$\nabla\times\left(\nabla\times\mathbf{A}\right) = \nabla\left(\nabla\cdot\mathbf{A}\right) - \nabla^2\mathbf{A}$$

and use the divergence free property of the fields (2.13 and (2.14), we obtain the vector wave equations for $\mathbf{E}$ and $\mathbf{H}$,

$$\nabla^2\mathbf{E} + k^2\,\mathbf{E} = 0 \tag{2.17}$$

$$\nabla^2\mathbf{H} + k^2\,\mathbf{H} = 0 \tag{2.18}$$

where $k^2 = \omega^2\varepsilon\mu$. From (2.17) and (2.18), any divergence free vector field that satisfies the vector wave equation is an acceptable field. The corresponding magnetic field, $\mathbf{H}$, can be determined by the curl of $\mathbf{E}$.

Boundary Conditions

When solving problems of this nature, we generally solve (2.17) and (2.18) to determine the fields at all positions both internally and externally to the particle. In order to account for fields transitioning from one medium to another, we must impose boundary conditions at the interface. In electromagnetics, we require the tangential components of the field to be continuous at the interface,

$$\left(\mathbf{E}_2 - \mathbf{E}_1\right)\times\hat{\mathbf{n}} = 0 \tag{2.19}$$

32

$$(\mathbf{H}_2 - \mathbf{H}_1) \times \hat{n} = 0 \tag{2.20}$$

where $\hat{n}$ is the outward normal of the interface. For a particle, this condition is applied on its surface.

From the Maxwell equations (2.13-2.16), the wave equations (2.17, 2.18) and the boundary conditions (2.19, 2.20), we now have the foundation to solve the problem of a harmonic plane wave illuminating a cylinder.

2.1.3 Cylindrical Vector Harmonics

Theoretical Basis of Vector Harmonics

In general, because we require field solutions at all positions in our domain, we must solve the vector wave equations (2.17) and (2.18) derived in the previous section. However, directly solving these equations presents an intractable problem. Instead, we can utilize a set of vector harmonics to write the field solutions in a new basis concentric with the particle shape. As will be shown, this will greatly simplify the problem. To establish a complete basis capable of describing an electromagnetic field, two vector harmonics are defined,

$$\mathbf{M} = \nabla \times (\hat{c}\psi) \tag{2.21}$$

$$\mathbf{N} = \frac{\nabla \times \mathbf{M}}{k} \tag{2.22}$$

where $\mathbf{M}$ and $\mathbf{N}$ are the vector harmonics, ψ is a scalar function, $\hat{c}$ is the pilot vector and k is the wave vector. We note that $\hat{c}$ is an arbitrary constant vector that is orthogonal to $\mathbf{M}$. It is typically chosen to be along one of the coordinate axes for mathematical simplicity. These harmonics must exhibit the properties inherent in electromagnetic fields: (1) $\mathbf{M}$ and $\mathbf{N}$ must be divergence free, (2) $\mathbf{M}$ and $\mathbf{N}$ must be related to one another via the curl operator and (3) $\mathbf{M}$ and $\mathbf{N}$ must be solutions to a vector wave equation. For (1), we note that that divergence of a curl of any vector will equal zero. Thus,

$$\nabla \cdot \mathbf{M} = 0$$

$$\nabla \cdot \mathbf{N} = 0$$

To satisfy (2), we note that $\mathbf{M}$ and $\mathbf{N}$ can be further related by,

$$\nabla \times \mathbf{N} = k\mathbf{M} \tag{2.23}$$

33

As for (3), we can derive a corresponding wave equation for $\mathbf{M}$ and $\mathbf{N}$ as we did before for $\mathbf{E}$ and $\mathbf{H}$,

$$\nabla \times (\nabla \times \mathbf{M}) = \underbrace{\nabla(\nabla \cdot \mathbf{M})}_{0} - \nabla \cdot (\nabla \mathbf{M}) = -\nabla^2 \mathbf{M}$$

$$\nabla \times (\nabla \times \mathbf{M}) = k \cdot (\nabla \times \mathbf{N}) = k^2 \mathbf{M}$$

Thus,

$$\nabla^2 \mathbf{M} + k^2 \mathbf{M} = 0 \qquad (2.24)$$

Similarly, for $\mathbf{N}$,

$$\nabla^2 \mathbf{N} + k^2 \mathbf{N} = 0 \qquad (2.25)$$

Therefore, these harmonics exhibit all the properties needed to describe an electromagnetic field. Now if we were to substitute (2.21) into (2.24), we can derive the following,

$$\nabla^2 \mathbf{M} + k^2 \mathbf{M} = \nabla^2 (\nabla \times \hat{\mathbf{c}} \psi) + k^2 (\nabla \times \hat{\mathbf{c}} \psi)$$

We note that the Laplace operator, ∇^2, is a scalar operator. Hence, we can rearrange this to be,

$$\nabla^2 \mathbf{M} + k^2 \mathbf{M} = \nabla \times (\nabla^2 (\hat{\mathbf{c}} \psi) + k^2 (\hat{\mathbf{c}} \psi)) = \nabla \times \left(\underbrace{\psi \nabla^2 \hat{\mathbf{c}}}_{0} + \hat{\mathbf{c}} \nabla^2 \psi + \hat{\mathbf{c}} k^2 \psi \right)$$

$$\nabla^2 \mathbf{M} + k^2 \mathbf{M} = \nabla \times \left[\hat{\mathbf{c}} (\nabla^2 \psi + k^2 \psi) \right] \qquad (2.26)$$

From (2.24) and (2.26), we can then show that,

$$\nabla^2 \psi + k^2 \psi = 0 \qquad (2.27)$$

Using (2.21), we can conclude that a solution to the scalar wave equation (2.27) will also be a solution to the vector wave equations (2.17, 2.18), which considerably simplifies the problem. Note that (2.27) can also be derived using (2.25).

The geometry of the particle will dictate the form of the scalar wave equation to be solved. Furthermore, since we use separation of variables to solve (2.27), the geometries we can consider are limited to the coordinate system used to define the Laplacian. In this case, we choose a cylindrical coordinate system to describe an infinitely long cylinder.

Cylindrical Vector Harmonics

For an infinitely long cylinder, the scalar wave equation becomes,

$$\frac{1}{r}\frac{\partial}{\partial r}\left(r\frac{\partial\psi}{\partial r}\right)+\frac{1}{r^2}\frac{\partial^2\psi}{\partial\varphi^2}+\frac{\partial^2\psi}{\partial z^2}+k^2\psi=0 \tag{2.28}$$

From separation of variables, we assume ψ has a solution of the form,

$$\psi(r,\varphi,z)=R(r)\Phi(\phi)Z(z) \tag{2.29}$$

Upon substituting (2.29) into (2.28), we obtain,

$$\frac{1}{r}\frac{\partial}{\partial r}\left(r\frac{\partial R}{\partial r}\right)\frac{1}{R}+\frac{1}{r^2}\frac{\partial^2\Phi}{\partial\varphi^2}\frac{1}{\Phi}+\frac{\partial^2 Z}{\partial z^2}\frac{1}{Z}+k^2=0$$

In order to solve each coordinate function in (2.29), we isolate and group terms according to the coordinate variable and lump all other terms into a separation constant. This is done in an order that is most convenient,

For $Z(z)$:

$$\frac{\partial^2 Z}{\partial z^2}\frac{1}{Z}=-\frac{1}{r}\frac{\partial}{\partial r}\left(r\frac{\partial R}{\partial r}\right)\frac{1}{R}-\frac{1}{r^2}\frac{\partial^2\Phi}{\partial\varphi^2}\frac{1}{\Phi}-k^2=-h^2$$

$$\rightarrow\frac{\partial^2 Z}{\partial z^2}+h^2 Z=0 \tag{2.30}$$

For $\Phi(\phi)$:

$$h^2=\frac{1}{r}\frac{\partial}{\partial r}\left(r\frac{\partial R}{\partial r}\right)\frac{1}{R}+\frac{1}{r^2}\frac{\partial^2\Phi}{\partial\varphi^2}\frac{1}{\Phi}+k^2$$

$$\frac{\partial^2\Phi}{\partial\varphi^2}\frac{1}{\Phi}=-r\frac{\partial}{\partial r}\left(r\frac{\partial R}{\partial r}\right)\frac{1}{R}-r^2\left(k^2-h^2\right)=-n^2$$

$$\rightarrow\frac{\partial^2\Phi}{\partial\varphi^2}+n^2\Phi=0 \tag{2.31}$$

For $R(r)$:

$$n^2=r\frac{\partial}{\partial r}\left(r\frac{\partial R}{\partial r}\right)\frac{1}{R}+r^2\left(k^2-h^2\right)$$

$$r\frac{\partial}{\partial r}\left(r\frac{\partial R}{\partial r}\right)+\left[r^2\left(k^2-h^2\right)-n^2\right]R=0$$

If we introduce a change of variables, $\rho = r\sqrt{k^2 - h^2}$, the expression becomes,

$$\rho \frac{\partial}{\partial \rho}\left(\rho \frac{\partial R}{\partial \rho}\right) + \left[\rho^2 - n^2\right]R = 0$$

Expanding the differential terms we obtain the following,

$$\rho^2 \frac{\partial^2 R}{\partial \rho^2} + \rho \frac{\partial R}{\partial \rho} + \left[\rho^2 - n^2\right]R = 0$$

This is Bessel's differential equation. Therefore, we replace R with Z_n to denote a solution of order n,

$$\rho^2 \frac{\partial^2 Z_n}{\partial \rho^2} + \rho \frac{\partial Z_n}{\partial \rho} + \left[\rho^2 - n^2\right]Z_n = 0 \tag{2.32}$$

Solving (2.30-2.32), we will find,

$$R = Z_n$$

$$\Phi = e^{in\varphi} \tag{2.33}$$

$$Z = e^{ihz}$$

where all of these functions are normalized. The separation constant h is dependent on the form of the incident field in the system and will be determined in Sec. 2.1.4. For the separation constant n, we require that ψ be a single-valued function with respect to the azimuthal angle, φ,

$$\lim_{v \to 2\pi} \psi(\varphi + v) = \psi(\varphi) \quad ; \text{for all } \varphi$$

Therefore, the separation constant n must equal to zero or an integer to satisfy this condition. The solution to the scalar wave equation using (2.33) is thus,

$$\psi_n(r,\varphi,z) = Z_n(\rho)e^{in\varphi}e^{ihz} \quad ; n = 0, \pm 1, \pm 2,... \tag{2.34}$$

From (2.34) we can now solve for the vector harmonics $\mathbf{M}_n$ and $\mathbf{N}_n$ of order n according to their definitions (2.21, 2.22),

$$\mathbf{M}_n = \nabla \times (\hat{\mathbf{z}}\psi_n) = \left[\frac{1}{r}\frac{\partial}{\partial \varphi}(\psi_n)\right]\hat{\mathbf{r}} + \left[-\frac{\partial}{\partial r}(\psi_n)\right]\hat{\boldsymbol{\varphi}}$$

Applying a change variables from r to ρ from before,

$$\mathbf{M}_n = \left[\frac{\sqrt{k^2 - h^2}}{\rho}\frac{\partial}{\partial \varphi}(\psi_n)\right]\hat{\mathbf{r}} + \left[-\sqrt{k^2 - h^2}\frac{\partial}{\partial \rho}(\psi_n)\right]\hat{\boldsymbol{\varphi}}$$

36

Thus,

$$\mathbf{M}_n = \left[\sqrt{k^2 - h^2}\, \frac{in}{\rho} Z_n(\rho) e^{i(n\varphi + hz)} \right] \hat{\mathbf{r}} + \left[-\sqrt{k^2 - h^2}\, Z_n'(\rho) e^{i(n\varphi + hz)} \right] \hat{\boldsymbol{\varphi}}$$

$$\rightarrow \mathbf{M}_n = \sqrt{k^2 - h^2} \left[i \frac{n}{\rho} Z_n(\rho) \hat{\mathbf{r}} - Z_n'(\rho) \hat{\boldsymbol{\varphi}} \right] e^{i(n\varphi + hz)} \qquad (2.35)$$

Similarly for $\mathbf{N}_n$,

$$\mathbf{N}_n = \frac{\nabla \times \mathbf{M}_n}{k} = \frac{1}{k} \left\{ \left[-\frac{\partial \mathbf{M}_{n,\varphi}}{\partial \varphi} \right] \hat{\mathbf{r}} + \left[\frac{\partial \mathbf{M}_{n,r}}{\partial z} \right] \hat{\boldsymbol{\varphi}} + \left[\frac{1}{r} \frac{\partial (r \mathbf{M}_{n,\varphi})}{\partial r} - \frac{1}{r} \frac{\partial \mathbf{M}_{n,r}}{\partial \varphi} \right] \hat{\mathbf{z}} \right\}$$

Applying a change of variables, $\rho = r\sqrt{k^2 - h^2}$,

$$\mathbf{N}_n = \frac{\nabla \times \mathbf{M}_n}{k} = \frac{1}{k} \left\{ \left[-\frac{\partial \mathbf{M}_{n,\varphi}}{\partial \varphi} \right] \hat{\mathbf{r}} + \left[\frac{\partial \mathbf{M}_{n,r}}{\partial z} \right] \hat{\boldsymbol{\varphi}} + \sqrt{k^2 - h^2} \left[\frac{1}{\rho} \frac{\partial (\rho \mathbf{M}_{n,\varphi})}{\partial \rho} - \frac{1}{\rho} \frac{\partial \mathbf{M}_{n,r}}{\partial \varphi} \right] \hat{\mathbf{z}} \right\}$$

Thus,

$$\mathbf{N}_n = \frac{1}{k} \left\{ \left[\sqrt{k^2 - h^2}\, ihZ_n'(\rho) e^{i(n\varphi + hz)} \right] \hat{\mathbf{r}} - \left[\sqrt{k^2 - h^2}\, nh \frac{Z_n(\rho)}{\rho} e^{i(n\varphi + hz)} \right] \hat{\boldsymbol{\varphi}} + \ldots \right.$$

$$\left. \ldots + \frac{\sqrt{k^2 - h^2}}{\rho} \left[-Z_n'(\rho) - \rho Z_n''(\rho) + \frac{n^2}{\rho} Z_n(\rho) \right] e^{i(n\varphi + hz)} \hat{\mathbf{z}} \right\}$$

For the z component, we can substitute (2.32) to simplify,

$$\rightarrow \mathbf{N}_n = \frac{\sqrt{k^2 - h^2}}{k} \left[ihZ_n'(\rho) \hat{\mathbf{r}} - nh \frac{Z_n(\rho)}{\rho} \hat{\boldsymbol{\varphi}} + \sqrt{k^2 - h^2}\, Z_n(\rho) \hat{\mathbf{z}} \right] e^{i(n\varphi + hz)} \qquad (2.36)$$

From (2.35) and (2.36), we now have the mathematical form of the vector harmonics. We note that these harmonics are orthogonal in the sense that,

$$\int_0^{2\pi} \mathbf{M}_n \cdot \mathbf{M}_m^* \, d\varphi = \int_0^{2\pi} \mathbf{N}_n \cdot \mathbf{N}_m^* \, d\varphi = \int_0^{2\pi} \mathbf{M}_n \cdot \mathbf{N}_m^* \, d\varphi = 0 \quad ; \quad n \neq m \qquad (2.37)$$

These cylindrical vector harmonics thus provide us the means to expand all fields in the system in a cylindrical basis. Although these harmonics are rather complex mathematically, it will be shown that the steps taken to solve the problem are now considerably simpler.

2.1.4 Field Expansion

General Form of Field Expansion Coefficients

The incident fields (2.4) and (2.5) can now be expanded using the derived vector harmonics (2.35) and (2.36). Since the radial component of the scalar solution (2.34) contains a Bessel function, we should ideally use a Hankel function so that all solutions to the Bessel differential equation are included. However, for the incident field, the direction of propagation is towards the center of the cylinder. Therefore, we must exclude the Bessel function of the second kind to avoid a singularity at $r = 0$. The expansion of the incident field can then be generally written as,

$$\mathbf{E}_i = \sum_{n=-\infty}^{\infty} \left[A_n \mathbf{M}_n^{(1)} + B_n \mathbf{N}_n^{(1)} \right] \tag{2.38}$$

where A_n and B_n are unknown coefficients and the superscript (1) denotes use of the Bessel function of the first kind. In order to solve for A_n and B_n, we can utilize the orthogonality of the vector harmonics (2.37) to show that,

$$\sum_{m=-\infty}^{\infty} \int_0^{2\pi} \left(\mathbf{E}_i \cdot \mathbf{M}_m^{(1)*} \right) d\varphi = \sum_{n=-\infty}^{\infty} \sum_{m=-\infty}^{\infty} \left[\underbrace{\int_0^{2\pi} \left(A_n \mathbf{M}_n^{(1)} \cdot \mathbf{M}_m^{(1)*} \right) d\varphi}_{= \ 0 \ \text{unless} \ n=m} + \underbrace{\int_0^{2\pi} \left(B_n \mathbf{N}_n^{(1)} \cdot \mathbf{M}_m^{(1)*} \right) d\varphi}_{= \ 0 \ \text{unless} \ n=m} \right]$$

where we have applied an integral of a dot product with $\mathbf{M}_m^{(1)*}$. Therefore,

$$\sum_{n=-\infty}^{\infty} \int_0^{2\pi} \left(\mathbf{E}_i \cdot \mathbf{M}_n^{(1)*} \right) d\varphi = \sum_{n=-\infty}^{\infty} \left[A_n \int_0^{2\pi} \left(\mathbf{M}_n^{(1)} \cdot \mathbf{M}_n^{(1)*} \right) d\varphi + B_n \int_0^{2\pi} \left(\mathbf{N}_n^{(1)} \cdot \mathbf{M}_n^{(1)*} \right) d\varphi \right]$$

For a particular n,

$$\underbrace{\int_0^{2\pi} \left(\mathbf{E}_i \cdot \mathbf{M}_n^{(1)*} \right) d\varphi}_{5} = A_n \underbrace{\int_0^{2\pi} \left(\mathbf{M}_n^{(1)} \cdot \mathbf{M}_n^{(1)*} \right) d\varphi}_{1} + B_n \underbrace{\int_0^{2\pi} \left(\mathbf{N}_n^{(1)} \cdot \mathbf{M}_n^{(1)*} \right) d\varphi}_{2} \tag{2.39}$$

We can derive a second expression in a similar manner by applying a dot product with $\mathbf{N}_m^{(1)*}$,

$$\underbrace{\int_0^{2\pi} \left(\mathbf{E}_i \cdot \mathbf{N}_n^{(1)*} \right) d\varphi}_{6} = A_n \underbrace{\int_0^{2\pi} \left(\mathbf{M}_n^{(1)} \cdot \mathbf{N}_n^{(1)*} \right) d\varphi}_{3} + B_n \underbrace{\int_0^{2\pi} \left(\mathbf{N}_n^{(1)} \cdot \mathbf{N}_n^{(1)*} \right) d\varphi}_{4} \tag{2.40}$$

The numbers below each term correspond to the order in which these terms are solved in the next section.

38

Solutions to the Field Expansion Coefficients

In order to solve for A_n and B_n, we must solve the integrals contained in (2.39) and (2.40). To start, let's solve the integrals containing only the vector harmonics:

Equation 1: $\int\limits_{0}^{2\pi} \left(\mathbf{M}_n^{(1)} \cdot \mathbf{M}_n^{(1)*} \right) d\varphi$

$$\int\limits_{0}^{2\pi} \left(\mathbf{M}_n^{(1)} \cdot \mathbf{M}_n^{(1)*} \right) d\varphi = \int\limits_{0}^{2\pi} \sqrt{k^2 - h^2} \left[in \frac{J_n(\rho)}{\rho} \hat{\mathbf{r}} - J_n'(\rho) \hat{\boldsymbol{\varphi}} \right] e^{i(n\varphi + hz)} \cdots$$

$$\cdots \sqrt{k^2 - h^2} \left[-in \frac{J_n(\rho)}{\rho} \hat{\mathbf{r}} - J_n'(\rho) \hat{\boldsymbol{\varphi}} \right] e^{-i(n\varphi + hz)} d\varphi$$

$$= \left(k^2 - h^2 \right) \int\limits_{0}^{2\pi} \left[n^2 \frac{J_n^2(\rho)}{\rho^2} + J_n'^2(\rho) \right] d\varphi$$

$$\rightarrow \int\limits_{0}^{2\pi} \left(\mathbf{M}_n^{(1)} \cdot \mathbf{M}_n^{(1)*} \right) d\varphi = 2\pi \left(k^2 - h^2 \right) \left[\frac{n^2}{\rho^2} J_n^2(\rho) + J_n'^2(\rho) \right] \tag{2.41}$$

Equation 2: $\int\limits_{0}^{2\pi} \left(\mathbf{N}_n^{(1)} \cdot \mathbf{M}_n^{(1)*} \right) d\varphi$

$$\int\limits_{0}^{2\pi} \left(\mathbf{N}_n^{(1)} \cdot \mathbf{M}_n^{(1)*} \right) d\varphi = \int\limits_{0}^{2\pi} \frac{\sqrt{k^2 - h^2}}{k} \left[ihJ_n'(\rho)\hat{\mathbf{r}} - nh \frac{J_n(\rho)}{\rho} \hat{\boldsymbol{\varphi}} + \sqrt{k^2 - h^2} J_n(\rho)\hat{\mathbf{z}} \right] e^{i(n\varphi + hz)} \cdots$$

$$\cdots \sqrt{k^2 - h^2} \left[-in \frac{J_n(\rho)}{\rho} \hat{\mathbf{r}} - J_n'(\rho) \hat{\boldsymbol{\varphi}} \right] e^{-i(n\varphi + hz)} d\varphi$$

$$= \frac{\left(k^2 - h^2 \right)}{k} \int\limits_{0}^{2\pi} \left[\frac{nh}{\rho} J_n(\rho) J_n'(\rho) + \frac{nh}{\rho} J_n(\rho) J_n'(\rho) \right] d\varphi$$

$$\rightarrow \int\limits_{0}^{2\pi} \left(\mathbf{N}_n^{(1)} \cdot \mathbf{M}_n^{(1)*} \right) d\varphi = 4\pi \frac{\left(k^2 - h^2 \right)}{k} \frac{nh}{\rho} J_n(\rho) J_n'(\rho) \tag{2.42}$$

Equation 3: $\int\limits_{0}^{2\pi} \left(\mathbf{M}_n^{(1)} \cdot \mathbf{N}_n^{(1)*} \right) d\varphi$

$$\int\limits_{0}^{2\pi} \left(\mathbf{M}_n^{(1)} \cdot \mathbf{N}_n^{(1)*} \right) d\varphi = \int\limits_{0}^{2\pi} \left(\mathbf{N}_n^{(1)} \cdot \mathbf{M}_n^{(1)*} \right) d\varphi = 4\pi \frac{\left(k^2 - h^2 \right)}{k} \frac{nh}{\rho} J_n(\rho) J_n'(\rho) \tag{2.43}$$

39

Equation 4: $\int\limits_0^{2\pi} \left(\mathbf{N}_n^{(1)} \cdot \mathbf{N}_n^{(1)*} \right) d\varphi$

$$\int\limits_0^{2\pi} \left(\mathbf{N}_n^{(1)} \cdot \mathbf{N}_n^{(1)*} \right) d\varphi = \int\limits_0^{2\pi} \frac{\sqrt{k^2 - h^2}}{k} \left[ihJ_n'(\rho)\hat{\mathbf{r}} - nh\frac{J_n(\rho)}{\rho}\hat{\boldsymbol{\varphi}} + \sqrt{k^2 - h^2}\,J_n(\rho)\hat{\mathbf{z}} \right] e^{i(n\varphi + hz)} \cdot \ldots$$

$$\ldots \cdot \frac{\sqrt{k^2 - h^2}}{k} \left[-ihJ_n'(\rho)\hat{\mathbf{r}} - nh\frac{J_n(\rho)}{\rho}\hat{\boldsymbol{\varphi}} + \sqrt{k^2 - h^2}\,J_n(\rho)\hat{\mathbf{z}} \right] e^{-i(n\varphi + hz)} d\varphi$$

$$= \frac{\left(k^2 - h^2\right)}{k^2} \int\limits_0^{2\pi} \left[h^2 J_n'^2(\rho) + \frac{n^2 h^2}{\rho^2} J_n^2(\rho) + \left(k^2 - h^2\right) J_n^2(\rho) \right] d\varphi$$

$$\rightarrow \int\limits_0^{2\pi} \left(\mathbf{N}_n^{(1)} \cdot \mathbf{N}_n^{(1)*} \right) d\varphi = 2\pi \frac{\left(k^2 - h^2\right)}{k^2} \left[h^2 J_n'^2(\rho) + \frac{n^2 h^2}{\rho^2} J_n^2(\rho) + \left(k^2 - h^2\right) J_n^2(\rho) \right] \quad (2.44)$$

Now, let's solve terms 5 and 6 which contain the incident field, $\mathbf{E}_i$, for case I. Note that now we change the subscript for the expansion coefficients to be $A_{n,I}$ and $B_{n,I}$ to reflect case I,

Equation 5: $\int\limits_0^{2\pi} \left(\mathbf{E}_{i,I} \cdot \mathbf{M}_n^{(1)*} \right) d\varphi$

$$\int\limits_0^{2\pi} \left(\mathbf{E}_{i,I} \cdot \mathbf{M}_n^{(1)*} \right) d\varphi = \int\limits_0^{2\pi} E_0 \left(-\cos\zeta\cos\varphi\,\hat{\mathbf{r}} + \cos\zeta\sin\varphi\,\hat{\boldsymbol{\varphi}} + \sin\zeta\,\hat{\mathbf{z}} \right) e^{-ik(r\sin\zeta\cos\varphi + z\cos\zeta)} \cdot \ldots$$

$$\ldots \cdot \sqrt{k^2 - h^2} \left[-in\frac{J_n(\rho)}{\rho}\hat{\mathbf{r}} - J_n'(\rho)\hat{\mathbf{j}} \right] e^{-i(n\varphi + hz)} d\varphi$$

$$= E_0 \cos\zeta \sqrt{k^2 - h^2}\; e^{-i(kz\cos\zeta + hz)} \left[in\frac{J_n(\rho)}{\rho} \underbrace{\int\limits_0^{2\pi} \cos\varphi \cdot e^{-i(kr\sin\zeta\cos\varphi + n\varphi)} d\varphi}_{\alpha_n^{(2)}} - \ldots \right.$$

$$\left. \ldots - J_n'(\rho) \underbrace{\int\limits_0^{2\pi} \sin\varphi \cdot e^{-i(kr\sin\zeta\cos\varphi + n\varphi)} d\varphi}_{\alpha_n^{(3)}} \right]$$

Because $A_{n,I}$ and $B_{n,I}$ must be independent of all coordinate variables, we can observe that $h = -k\cos\zeta$ from the exponential term. Thus,

$$\rightarrow \int_0^{2\pi} \left(\mathbf{E}_{i,I} \cdot \mathbf{M}_n^{(1)*}\right) d\varphi = E_0 k \sin\zeta \cos\zeta \left[in \frac{J_n(\rho)}{\rho} \alpha_n^{(2)} - J_n'(\rho) \alpha_n^{(3)} \right] \tag{2.45}$$

Equation 6: $\displaystyle\int_0^{2\pi} \left(\mathbf{E}_{i,I} \cdot \mathbf{N}_n^{(1)*}\right) d\varphi$

$$\int_0^{2\pi} \left(\mathbf{E}_{i,I} \cdot \mathbf{N}_n^{(1)*}\right) d\varphi = \int_0^{2\pi} E_0 \left(-\cos\zeta\cos\varphi\,\hat{\mathbf{r}} + \cos\zeta\sin\varphi\,\hat{\boldsymbol{\varphi}} + \sin\zeta\,\hat{\mathbf{z}}\right) e^{-ik(r\sin\zeta\cos\varphi + z\cos\zeta)} \cdot \ldots$$

$$\ldots \cdot \frac{\sqrt{k^2 - h^2}}{k} \left\{ ihZ_n'(\rho)\hat{\mathbf{r}} - nh\frac{Z_n(\rho)}{\rho}\hat{\boldsymbol{\varphi}} + \sqrt{k^2 - h^2}\,Z_n(\rho)\hat{\mathbf{z}} \right\} e^{i(n\varphi + hz)} d\varphi$$

$$= E_0 \frac{\sqrt{k^2 - h^2}}{k} e^{-i(kz\cos\zeta + hz)} \left[ih\cos\zeta J_n'(\rho) \underbrace{\int_0^{2\pi} \cos\varphi \cdot e^{-i(kr\sin\zeta\cos\varphi + n\varphi)} d\varphi}_{\alpha_n^{(2)}} - \ldots \right.$$

$$\ldots - hn\cos\zeta \frac{J_n(\rho)}{\rho} \underbrace{\int_0^{2\pi} \sin\varphi \cdot e^{-i(kr\sin\zeta\cos\varphi + n\varphi)} d\varphi}_{\alpha_n^{(3)}} + \ldots$$

$$\left. \ldots + \sin\zeta\sqrt{k^2 - h^2}\,J_n(\rho) \underbrace{\int_0^{2\pi} e^{-i(kr\sin\zeta\cos\varphi + n\varphi)} d\varphi}_{\alpha_n^{(1)}} \right]$$

$$\rightarrow \int_0^{2\pi} \left(\mathbf{E}_{i,I} \cdot \mathbf{N}_n^{(1)*}\right) d\varphi = E_0 k \sin\zeta \left[-i\cos^2\zeta J_n'(\rho) \alpha_n^{(2)} + n\cos^2\zeta \frac{J_n(\rho)}{\rho} \alpha_n^{(3)} \ldots \right.$$

$$\left. \ldots + \sin^2\zeta J_n(\rho) \alpha_n^{(1)} \right] \tag{2.46}$$

As we can see from (2.45) and (2.46), we must solve integrals of the form,

$$\alpha_n^{(1)} = \int_0^{2\pi} e^{-i(\rho\cos\varphi + n\varphi)} d\varphi$$

$$\alpha_n^{(2)} = \int_0^{2\pi} \cos\varphi \cdot e^{-i(\rho\cos\varphi + n\varphi)} d\varphi$$

41

$$\alpha_n^{(3)} = \int\limits_0^{2\pi} \sin\varphi \cdot e^{-i(\rho\cos\varphi + n\varphi)} d\varphi$$

where $\rho = r\sqrt{k^2 - h^2} = kr\sin\zeta$. To do so, we make use of the integral representation of the Bessel function,

$$J_n(\rho) = \frac{1}{2\pi(i)^n} \int\limits_0^{2\pi} e^{i(\rho\cos\varphi + n\varphi)} d\varphi$$

We can use the complex conjugate noting that $J_n(\rho)$ must be real,

$$J_n(\rho) = \frac{1}{2\pi(-i)^n} \int\limits_0^{2\pi} e^{-i(\rho\cos\varphi + n\varphi)} d\varphi \tag{2.47}$$

$\alpha_n^{(1)}$: From (2.47),

$$\alpha_n^{(1)} = 2\pi(-i)^n J_n(\rho) \tag{2.48}$$

$\alpha_n^{(2)}$: To determine $\alpha_n^{(2)}$, we can take the derivative of $\alpha_n^{(1)}$,

$$\frac{d\left(\alpha_n^{(1)}\right)}{d\rho} = -i \int\limits_0^{2\pi} \cos\varphi \cdot e^{-i(\rho\cos\varphi + n\varphi)} d\varphi = -i\alpha_n^{(2)} = 2\pi(-i)^n J_n'(\rho)$$

$$\alpha_n^{(2)} = 2\pi\, i(-i)^n J_n'(\rho) \tag{2.49}$$

$\alpha_n^{(3)}$: For $\alpha_n^{(3)}$, we can derive the following expression,

$$\alpha_{n-1}^{(1)} - \alpha_{n+1}^{(1)} = \int\limits_0^{2\pi} e^{-i(\rho\cos\varphi + n\varphi)} \cdot e^{i\varphi} d\varphi - \int\limits_0^{2\pi} e^{-i(\rho\cos\varphi + n\varphi)} \cdot e^{-i\varphi} d\varphi$$

$$= \int\limits_0^{2\pi} e^{-i(\rho\cos\varphi + n\varphi)} \cdot (\cos\varphi + i\sin\varphi) d\varphi - \int\limits_0^{2\pi} e^{-i(\rho\cos\varphi + n\varphi)} \cdot (\cos\varphi - i\sin\varphi) d\varphi$$

$$= 2i \int\limits_0^{2\pi} e^{-i(\rho\cos\varphi + n\varphi)} \cdot \sin\varphi\, d\varphi = 2i\alpha_n^{(3)}$$

$$\rightarrow \alpha_{n-1}^{(1)} - \alpha_{n+1}^{(1)} = 2i\alpha_n^{(3)} \tag{2.50}$$

If we use (2.50) with the following recurrence relation,

$$\frac{2nJ_n(\rho)}{\rho} = J_{n-1}(\rho) + J_{n+1}(\rho)$$

42

we find that,

$$2i\alpha_n^{(3)} = 2\pi(-i)^{n-1} J_{n-1}(\rho) - 2\pi(-i)^{n+1} J_{n+1}(\rho)$$

$$2i\alpha_n^{(3)} = 2\pi i(-i)^n \cdot \left[\frac{2nJ_n(\rho)}{\rho} - J_{n+1}(\rho) \right] + 2\pi i(-i)^n J_{n+1}(\rho)$$

$$\alpha_n^{(3)} = 2\pi(-i)^n \frac{n}{\rho} J_n(\rho) \tag{2.51}$$

Using (2.48), (2.49) and (2.51), and the definition for h, we can now write all the solutions to the integral terms to be,

Equation 1: $\int_0^{2\pi} \left(\mathbf{M}_n^{(1)} \cdot \mathbf{M}_n^{(1)*} \right) d\varphi$

$$\int_0^{2\pi} \left(\mathbf{M}_n^{(1)} \cdot \mathbf{M}_n^{(1)*} \right) d\varphi = 2\pi k^2 \sin^2\zeta \left[\frac{n^2}{\rho^2} J_n^2(\rho) + J_n'^2(\rho) \right] \tag{2.52}$$

Equation 2: $\int_0^{2\pi} \left(\mathbf{N}_n^{(1)} \cdot \mathbf{M}_n^{(1)*} \right) d\varphi$

$$\int_0^{2\pi} \left(\mathbf{N}_n^{(1)} \cdot \mathbf{M}_n^{(1)*} \right) d\varphi = -4\pi k^2 \sin^2\zeta \cos\zeta \frac{n}{\rho} J_n(\rho) J_n'(\rho) \tag{2.53}$$

Equation 3: $\int_0^{2\pi} \left(\mathbf{M}_n^{(1)} \cdot \mathbf{N}_n^{(1)*} \right) d\varphi$

$$\int_0^{2\pi} \left(\mathbf{M}_n^{(1)} \cdot \mathbf{N}_n^{(1)*} \right) d\varphi = -4\pi k^2 \sin^2\zeta \cos\zeta \frac{n}{\rho} J_n(\rho) J_n'(\rho) \tag{2.54}$$

Equation 4: $\int_0^{2\pi} \left(\mathbf{N}_n^{(1)} \cdot \mathbf{N}_n^{(1)*} \right) d\varphi$

$$\int_0^{2\pi} \left(\mathbf{N}_n^{(1)} \cdot \mathbf{N}_n^{(1)*} \right) d\varphi = 2\pi k^2 \sin^2\zeta \left[\cos^2\zeta J_n'^2(\rho) + \frac{n^2}{\rho^2} \cos^2\zeta J_n^2(\rho) + \sin^2\zeta J_n^2(\rho) \right] \tag{2.55}$$

Equation 5: $\int_0^{2\pi} \left(\mathbf{E}_{i,I} \cdot \mathbf{M}_n^{(1)*} \right) d\varphi$

$$\int_0^{2\pi} \left(\mathbf{E}_{i,I} \cdot \mathbf{M}_n^{(1)*} \right) d\varphi = E_0 k \sin\zeta \cos\zeta \left[-2\pi(-i)^n \frac{n}{\rho} J_n(\rho) J_n'(\rho) - 2\pi(-i)^n \frac{n}{\rho} J_n'(\rho) J_n(\rho) \right]$$

$$\rightarrow \int_0^{2\pi} \left(\mathbf{E}_{i,I} \cdot \mathbf{M}_n^{(1)*} \right) d\varphi = -4\pi E_0 k \sin\zeta \cos\zeta (-i)^n \frac{n}{\rho} J_n(\rho) J_n'(\rho) \tag{2.56}$$

Equation 6: $\int_0^{2\pi} \left(\mathbf{E}_{i,I} \cdot \mathbf{N}_n^{(1)*} \right) d\varphi$

$$\int_0^{2\pi} \left(\mathbf{E}_{i,I} \cdot \mathbf{N}_n^{(1)*} \right) d\varphi = E_0 k \sin\zeta \left[2\pi\cos^2\zeta (-i)^n J_n'^2(\rho) + 2\pi\cos^2\zeta (-i)^n \frac{n^2}{\rho^2} J_n^2(\rho) + \dots \right.$$

$$\left. \dots + 2\pi\sin^2\zeta (-i)^n J_n^2(\rho) \right]$$

$$\rightarrow \int_0^{2\pi} \left(\mathbf{E}_{i,I} \cdot \mathbf{N}_n^{(1)*} \right) d\varphi = 2\pi E_0 k \sin\zeta (-i)^n \left[\cos^2\zeta J_n'^2(\rho) + \cos^2\zeta \frac{n^2}{\rho^2} J_n^2(\rho) + \dots \right.$$

$$\left. \dots + \sin^2\zeta J_n^2(\rho) \right] \tag{2.57}$$

We can now substitute in (2.52-2.57) and solve for $A_{n,I}$ and $B_{n,I}$. For our first equation (2.39),

$$-4\pi E_0 k \sin\zeta \cos\zeta (-i)^n \frac{n}{\rho} J_n(\rho) J_n'(\rho) = A_{n,I} 2\pi k^2 \sin^2\zeta \left[n^2 \frac{J_n^2(\rho)}{\rho^2} + J_n'^2(\rho) \right] - \dots$$

$$\dots - B_{n,I} 4\pi k^2 \sin^2\zeta \cos\zeta \frac{n}{\rho} J_n(\rho) J_n'(\rho)$$

$$\rightarrow A_{n,I} = B_{n,I} \left[\frac{2\cos\zeta \frac{n}{\rho} J_n(\rho) J_n'(\rho)}{\frac{n^2}{\rho^2} J_n^2(\rho) + J_n'^2(\rho)} \right] - \frac{E_0 (-i)^n}{k\sin\zeta} \left[\frac{2\cos\zeta \frac{n}{\rho} J_n(\rho) J_n'(\rho)}{\frac{n^2}{\rho^2} J_n^2(\rho) + J_n'^2(\rho)} \right]$$

To simplify the expression, we define,

$$Y = \left[\frac{2\cos\zeta \frac{n}{\rho} J_n(\rho) J_n'(\rho)}{\frac{n^2}{\rho^2} J_n^2(\rho) + J_n'^2(\rho)} \right]$$

Thus,

$$A_{n,I} = B_{n,I} Y - \frac{E_0 (-i)^n}{k\sin\zeta} Y \tag{2.58}$$

44

For our second equation (2.40),

$$2\pi E_0 k \sin\zeta \, (-i)^n \left[\cos^2\zeta J_n'^2(\rho) + \cos^2\zeta \frac{n^2}{\rho^2} J_n^2(\rho) + \sin^2\zeta J_n^2(\rho) \right] = \ldots$$

$$\ldots = -A_{n,l} \, 4\pi k^2 \sin^2\zeta \cos\zeta \frac{n}{\rho} J_n(\rho) J_n'(\rho) + \ldots$$

$$\ldots + B_{n,l} \, 2\pi k^2 \sin^2\zeta \left[\cos^2\zeta J_n'^2(\rho) + \frac{n^2}{\rho^2} \cos^2\zeta J_n^2(\rho) + \sin^2\zeta J_n^2(\rho) \right]$$

$$\rightarrow A_{n,l} = B_{n,l} \left[\frac{\cos^2\zeta J_n'^2(\rho) + \frac{n^2}{\rho^2} \cos^2\zeta J_n^2(\rho) + \sin^2\zeta J_n^2(\rho)}{2\cos\zeta \frac{n}{\rho} J_n(\rho) J_n'(\rho)} \right] - \ldots$$

$$\ldots - \frac{E_0 (-i)^n}{k\sin\zeta} \left[\frac{\cos^2\zeta J_n'^2(\rho) + \cos^2\zeta \frac{n^2}{\rho^2} J_n^2(\rho) + \sin^2\zeta J_n^2(\rho)}{2\cos\zeta \frac{n}{\rho} J_n(\rho) J_n'(\rho)} \right]$$

We can again simplify this expression by defining,

$$X = \left[\frac{\cos^2\zeta J_n'^2(\rho) + \frac{n^2}{\rho^2} \cos^2\zeta J_n^2(\rho) + \sin^2\zeta J_n^2(\rho)}{2\cos\zeta \frac{n}{\rho} J_n(\rho) J_n'(\rho)} \right]$$

Thus,

$$A_{n,l} = B_{n,l} X - \frac{E_0 (-i)^n}{k\sin\zeta} X \tag{2.59}$$

Therefore, from (2.58) and (2.59),

$$B_{n,l} Y - \frac{E_0 (-i)^n}{k\sin\zeta} Y = B_{n,l} X - \frac{E_0 (-i)^n}{k\sin\zeta} X$$

$$B_{n,l} (Y - X) = \frac{E_0 (-i)^n}{k\sin\zeta} (Y - X)$$

$$\rightarrow B_{n,l} = \frac{E_0 (-i)^n}{k\sin\zeta} \tag{2.60}$$

45

Then,

$$\rightarrow A_{n,I} = 0 \tag{2.61}$$

Thus, after all the arduous mathematics employed in this section, we find the expansion coefficients (2.60) and (2.61) are simple expressions. Upon substituting (2.60) and (2.61) into (2.38), we can now write the incident fields to be the following,

$$\mathbf{E}_{i,I} = \sum_{n=-\infty}^{\infty} E_n \mathbf{N}_n^{(1)}, \quad \mathbf{H}_{i,I} = -\frac{ik}{\omega\mu} \sum_{n=-\infty}^{\infty} E_n \mathbf{M}_n^{(1)} \tag{2.62}$$

where,

$$E_n = B_{n,I} = \frac{E_0 (-i)^n}{k\sin\zeta}$$

Internal and Scattered Fields

Now that the solutions to the incident fields are known, we can write the general form of the internal fields, $\mathbf{E}_{1,I}$ and $\mathbf{H}_{1,I}$, and the scattered fields, $\mathbf{E}_{s,I}$ and $\mathbf{H}_{s,I}$. The form of these fields is dictated by the boundary conditions, the orthogonality of the vector harmonics and the form of the incident field.

For the internal field, we again require $h = -k\cos\zeta$ to ensure continuity at the boundary of the cylinder in the z direction. We also require use of the Bessel function of the first kind, $J_n(\rho_1)$, in order to avoid a singularity at the origin as before. The variable ρ_1 is determined by the refractive index of the cylinder, m,

$$\rho_1 = r\sqrt{k_1^2 - h^2} = kr\sqrt{m^2 - \cos^2\zeta}$$

where $k_1 = mk$. The expansions for the internal fields thus take the following form,

$$\mathbf{E}_{1,I} = \sum_{n=-\infty}^{\infty} E_n \left[g_{nI} \mathbf{M}_n^{(1)} + f_{nI} \mathbf{N}_n^{(1)} \right], \quad \mathbf{H}_{1,I} = -\frac{ik_1}{\omega\mu_1} \sum_{n=-\infty}^{\infty} E_n \left[g_{nI} \mathbf{N}_n^{(1)} + f_{nI} \mathbf{M}_n^{(1)} \right] \tag{2.63}$$

where g_{nI} and f_{nI} are unknown coefficients for the internal field.

We can expand the scattered field in a similar manner. However in this case, because the scattered field is an outgoing wave from the cylinder, we no longer need to restrict ourselves to a particular Bessel function. To make use of both solutions to the Bessel equation, we use the

Hankel functions. The two Hankel functions are defined as $H_n^{(1)} = J_n + iY_n$ and $H_n^{(2)} = J_n - iY_n$. Since we are in the far-field regime, the asymptotic solutions to the Hankel functions are,

$$H_n^{(1)}(\rho_s) \approx \sqrt{\frac{2}{\pi \rho_s}} e^{i\rho_s} (-i)^n e^{-i\pi/4}$$

$$H_n^{(2)}(\rho_s) \approx \sqrt{\frac{2}{\pi \rho_s}} e^{-i\rho_s} (i)^n e^{i\pi/4}$$

where $|\rho_s| \gg n^2$. Since we are concerned with outgoing waves, we only need $H_n^{(1)}(\rho_s)$. We also note that $\rho_s = \rho$. Thus, the field expansions will take the following form,

$$\mathbf{E}_{s,I} = -\sum_{n=-\infty}^{\infty} E_n \left[ia_{nI} \, \mathbf{M}_n^{(3)} + b_{nI} \, \mathbf{N}_n^{(3)} \right], \quad \mathbf{H}_{s,I} = \frac{ik}{\omega \mu} \sum_{n=-\infty}^{\infty} E_n \left[ia_{nI} \, \mathbf{N}_n^{(3)} + b_{nI} \, \mathbf{M}_n^{(3)} \right] \qquad (2.64)$$

where a_{nI} and b_{nI} are unknown coefficients for the scattered field. The sign convention is also reversed to reflect the change in polarization of the field for an outgoing wave.

2.1.5 Application of Boundary Conditions

Solutions to Coefficients a_{nI} and b_{nI}

Now that we have the forms for all the fields present in the system (2.62-2.64), we need to solve for the unknown coefficients to obtain the field solutions. To do so, we make use of the continuity boundary conditions (2.19, 2.20) at $r = a$. Since we are operating in a cylindrical coordinate system, these boundary conditions become,

$$(\mathbf{E}_i + \mathbf{E}_s - \mathbf{E}_1)_I \times \hat{\mathbf{r}} = 0 \qquad . \qquad (2.65)$$

$$(\mathbf{H}_i + \mathbf{H}_s - \mathbf{H}_1)_I \times \hat{\mathbf{r}} = 0 \qquad (2.66)$$

The application of these boundary conditions is mathematically straight forward despite the complexity of the terms involved. The cross product with $\hat{\mathbf{r}}$ in (2.65) and (2.66) will lead to four equations. Since we have four unknown coefficients, the problem is well defined. However it should be noted that in the context of obtaining expressions for the efficiencies, we only require solutions to a_{nI} and b_{nI} since we can obtain the absorption efficiency from the extinction and scattering efficiency from (1.3). To begin, we apply (2.65) and (2.66) for a particular n,

$$\left[E_n \, \mathbf{N}_n^{(1)} - E_n \left(ia_{nI} \, \mathbf{M}_n^{(3)} + b_{nI} \, \mathbf{N}_n^{(3)} \right) - E_n \left(g_{nI} \, \mathbf{M}_n^{(1)} + f_{nI} \, \mathbf{N}_n^{(1)} \right) \right] \times \hat{\mathbf{r}} = 0 \qquad (2.67)$$

$$\left[-\frac{ik}{\omega\mu} E_n \mathbf{M}_n^{(1)} + \frac{ik}{\omega\mu} E_n \left(ia_{nl} \mathbf{N}_n^{(3)} + b_{nl} \mathbf{M}_n^{(3)} \right) + \frac{ik_1}{\omega\mu_1} E_n \left(g_{nl} \mathbf{N}_n^{(1)} + f_{nl} \mathbf{M}_n^{(1)} \right) \right] \times \hat{\mathbf{r}} = 0 \quad (2.68)$$

The general expansion of the cross product will take the following form,

$$(a\hat{\mathbf{r}} + b\hat{\boldsymbol{\varphi}} + c\hat{\mathbf{z}}) \times \hat{\mathbf{r}} = (0)\hat{\mathbf{r}} + (c)\hat{\boldsymbol{\varphi}} + (-b)\hat{\mathbf{z}} \quad (2.69)$$

From (2.69), it is obvious we will obtain two equations from the $\hat{\boldsymbol{\varphi}}$-component terms and the $\hat{\mathbf{z}}$-component terms in the vector harmonics. For the sake of brevity, we shall immediately isolate these terms and derive each equation separately from (2.67) and (2.68),

Equation 1: $\mathbf{E}_\phi$-component terms

Factoring E_n from (2.67), we obtain the following for the $\mathbf{E}_\phi$-component terms,

$$\frac{\sqrt{k^2 - h^2}}{k} \sqrt{k^2 - h^2} J_n(\rho) e^{i(n\varphi + hz)} - b_{nl} \frac{\sqrt{k^2 - h^2}}{k} \sqrt{k^2 - h^2} H_n^{(1)}(\rho) e^{i(n\varphi + hz)} - \ldots$$

$$\ldots - f_{nl} \frac{\sqrt{k_1^2 - h^2}}{k_1} \sqrt{k_1^2 - h^2} J_n(\rho_1) e^{i(n\varphi + hz)} = 0$$

Substituting $h = -k\cos\zeta$ and $k_1 = mk$ we obtain,

$$k\sin^2\zeta J_n(\rho) - b_{nl} k\sin^2\zeta H_n^{(1)}(\rho) - f_{nl} \frac{k(m^2 - \cos^2\zeta)}{m} J_n(\rho_1) = 0$$

Since ρ and ρ_1 are specified at $r = a$, we can define $x = ka$, $\xi = x\sin\zeta$ and $\eta = x\sqrt{m^2 - \cos^2\zeta}$ to simplify the expression. We multiply the previous expression by ka^2 to obtain the first equation,

$$\rightarrow \xi^2 J_n(\xi) - b_{nl} \xi^2 H_n^{(1)}(\xi) - f_{nl} \frac{\eta^2}{m} J_n(\eta) = 0$$

Equation 2: $\mathbf{E}_z$-component terms

Similarly for the $\mathbf{E}_z$-component terms,

$$nh \frac{\sqrt{k^2 - h^2}}{k} \frac{J_n(\rho)}{\rho} e^{i(n\varphi + hz)} - ia_{nl} \sqrt{k^2 - h^2} H_n^{(1)'}(\rho) e^{i(n\varphi + hz)} - \ldots$$

$$\ldots - b_{nl} nh \frac{\sqrt{k^2 - h^2}}{k} \frac{H_n^{(1)}(\rho)}{\rho} e^{i(n\varphi + hz)} - g_{nl} \sqrt{k_1^2 - h^2} J_n'(\rho_1) e^{i(n\varphi + hz)} - \ldots$$

$$\dots - f_{nl} nh \frac{\sqrt{k_1^2 - h^2}}{k_1} \frac{J_n(\rho_1)}{\rho_1} e^{i(n\varphi + hz)} = 0$$

Substituting for h and k_1 as before,

$$-nk\sin\zeta\cos\zeta \frac{J_n(\rho)}{\rho} - ia_{nl} k\sin\zeta H_n^{(1)'}(\rho) + b_{nl} nk\sin\zeta\cos\zeta \frac{H_n^{(1)}(\rho)}{\rho} - \dots$$

$$\dots - g_{nl} k\sqrt{m^2 - \cos^2\zeta} J_n'(\rho_1) + f_{nl} nk\cos\zeta \frac{\sqrt{m^2 - \cos^2\zeta}}{m} \frac{J_n(\rho_1)}{\rho_1} = 0$$

If we use the parameters previously defined for Equation 1 and multiply by a, the radius, this expression simplifies to become,

$$\rightarrow -n\cos\zeta J_n(\xi) - ia_{nl}\xi H_n^{(1)'}(\xi) + b_{nl} n\cos\zeta H_n^{(1)}(\xi) - g_{nl}\eta J_n'(\eta) + \dots$$

$$\dots + f_{nl} \frac{n}{m}\cos\zeta J_n(\eta) = 0$$

Equation 3: H_ϕ-component terms

For the magnetic field terms from (2.68), we assume $\mu_1 = \mu$,

$$-a_{nl} \frac{k}{\omega\mu} \frac{\sqrt{k^2 - h^2}}{k} \sqrt{k^2 - h^2} H_n^{(1)}(\rho) e^{i(n\varphi + hz)} + \dots$$

$$\dots + ig_{nl} \frac{k_1}{\omega\mu_1} \frac{\sqrt{k_1^2 - h^2}}{k_1} \sqrt{k_1^2 - h^2} J_n(\rho_1) e^{i(n\varphi + hz)} = 0$$

Factoring all common factors and substituting variables yields,

$$-a_{nl} k^2 \sin^2\zeta H_n^{(1)}(\rho) + ig_{nl} k^2 (m^2 - \cos^2\zeta) J_n(\rho_1) = 0$$

Multiply by a^2, we obtain,

$$\rightarrow -a_{nl}\xi^2 H_n^{(1)}(\xi) + ig_{nl}\eta^2 J_n(\eta) = 0$$

Equation 4: H_z-component terms

And finally for the H_z-component terms,

$$i\frac{k}{\omega\mu}\sqrt{k^2 - h^2} J_n'(\rho) e^{i(n\varphi + hz)} + a_{nl} \frac{k}{\omega\mu} nh \frac{\sqrt{k^2 - h^2}}{k} \frac{H_n^{(1)}(\rho)}{\rho} e^{i(n\varphi + hz)} - \dots$$

$$\dots - ib_{nl} \frac{k}{\omega\mu}\sqrt{k^2 - h^2} H_n^{(1)'}(\rho) e^{i(n\varphi + hz)} - ig_{nl} \frac{k_1}{\omega\mu_1} nh \frac{\sqrt{k_1^2 - h^2}}{k_1} \frac{J_n(\rho_1)}{\rho_1} e^{i(n\varphi + hz)} - \dots$$

$$\ldots - if_{nl}\frac{k_1}{\omega\mu_1}\sqrt{k_1^2 - h^2}J_n'(\rho_1)e^{i(n\varphi+hz)} = 0$$

Thus,

$$ik\sin\zeta J_n'(\rho) - a_{nl}nk\sin\zeta\cos\zeta\frac{H_n^{(1)}(\rho)}{\rho} - ib_{nl}k\sin\zeta H_n^{(1)'}(\rho) + \ldots$$

$$\ldots + ig_{nl}nk\cos\zeta\sqrt{m^2-\cos^2\zeta}\frac{J_n(\rho_1)}{\rho_1} - if_{nl}mk\sqrt{m^2-\cos^2\zeta}J_n'(\rho_1) = 0$$

Multiplying by a,

$$\rightarrow i\xi J_n'(\xi) - a_{nl}n\cos\zeta H_n^{(1)}(\xi) - ib_{nl}\xi H_n^{(1)'}(\xi) + ig_{nl}n\cos\zeta J_n(\eta) - if_{nl}m\eta J_n'(\eta) = 0$$

To summarize, the four equations we need to solve are,

1: $\xi^2 J_n(\xi) - b_{nl}\xi^2 H_n^{(1)}(\xi) - f_{nl}\dfrac{\eta^2}{m}J_n(\eta) = 0$ (2.70)

2: $-n\cos\zeta J_n(\xi) - ia_{nl}\xi H_n^{(1)'}(\xi) + b_{nl}n\cos\zeta H_n^{(1)}(\xi) - g_{nl}\eta J_n'(\eta) + \ldots$

$$\ldots + f_{nl}\frac{n}{m}\cos\zeta J_n(\eta) = 0$$ (2.71)

3: $-a_{nl}\xi^2 H_n^{(1)}(\xi) + ig_{nl}\eta^2 J_n(\eta) = 0$ (2.72)

4: $i\xi J_n'(\xi) - a_{nl}n\cos\zeta H_n^{(1)}(\xi) - ib_{nl}\xi H_n^{(1)'}(\xi) + ig_{nl}n\cos\zeta J_n(\eta) - if_{nl}m\eta J_n'(\eta) = 0$ (2.73)

In order to solve for a_{nl} and b_{nl}, we isolate and substitute terms in (2.70-2.73) until we obtain the solution. From (2.70),

$$f_{nl} = \frac{m\xi^2}{\eta^2 J_n(\eta)}\left[J_n(\xi) - b_{nl}H_n^{(1)}(\xi)\right]$$ (2.74)

From (2.72),

$$g_{nl} = -ia_{nl}\frac{\xi^2}{\eta^2}\frac{H_n^{(1)}(\xi)}{J_n(\eta)}$$ (2.75)

Substituting (2.74) and (2.75) into (2.71), we obtain,

$$-n\cos\zeta J_n(\xi) - ia_{nl}\xi H_n^{(1)'}(\xi) + b_{nl}n\cos\zeta H_n^{(1)}(\xi) + ia_{nl}\frac{\xi^2}{\eta^2}\frac{H_n^{(1)}(\xi)}{J_n(\eta)}\eta J_n'(\eta) + \ldots$$

$$...+\frac{m\xi^2}{\eta^2 J_n(\eta)}\Big[J_n(\xi)-b_{nl}H_n^{(1)}(\xi)\Big]\frac{n}{m}\cos\zeta J_n(\eta)=0$$

Simplifying and grouping terms we get,

$$\left[-n\cos\zeta J_n(\xi)+\frac{\xi^2}{\eta^2}n\cos\zeta J_n(\xi)\right]+ia_{nl}\left[\frac{\xi^2}{\eta}\frac{H_n^{(1)}(\xi)}{J_n(\eta)}J_n'(\eta)-\xi H_n^{(1)'}(\xi)\right]+...$$

$$...+b_{nl}\left[n\cos\zeta H_n^{(1)}(\xi)-\frac{\xi^2}{\eta^2}n\cos\zeta H_n^{(1)}(\xi)\right]=0$$

Solving for b_{nl},

$$b_{nl}=\frac{\left[-n\cos\zeta J_n(\xi)+\frac{\xi^2}{\eta^2}n\cos\zeta J_n(\xi)\right]}{\left[-n\cos\zeta H_n^{(1)}(\xi)+\frac{\xi^2}{\eta^2}n\cos\zeta H_n^{(1)}(\xi)\right]}+ia_{nl}\frac{\left[\frac{\xi^2}{\eta}\frac{H_n^{(1)}(\xi)}{J_n(\eta)}J_n'(\eta)-\xi H_n^{(1)'}(\xi)\right]}{\left[-n\cos\zeta H_n^{(1)}(\xi)+\frac{\xi^2}{\eta^2}n\cos\zeta H_n^{(1)}(\xi)\right]}$$

Simplifying,

$$b_{nl}=\frac{J_n(\xi)}{H_n^{(1)}(\xi)}-a_{nl}\frac{i\xi\left[\eta H_n^{(1)'}(\xi)J_n(\eta)-\xi H_n^{(1)}(\xi)J_n'(\eta)\right]}{n\cos\zeta\eta H_n^{(1)}(\xi)J_n(\eta)\left[\frac{\xi^2}{\eta^2}-1\right]}$$

We can simplify the expression by defining,

$$W_n=i\xi\left[\eta H_n^{(1)'}(\xi)J_n(\eta)-\xi H_n^{(1)}(\xi)J_n'(\eta)\right]$$

$$D_n=n\cos\zeta\eta H_n^{(1)}(\xi)J_n(\eta)\left[\frac{\xi^2}{\eta^2}-1\right]$$

Thus,

$$b_{nl}=\frac{J_n(\xi)}{H_n^{(1)}(\xi)}-a_{nl}\frac{W_n}{D_n} \qquad (2.76)$$

Now we substitute (2.74-2.76) into (2.73) to get,

$$i\xi J_n'(\xi)-a_{nl}n\cos\zeta H_n^{(1)}(\xi)-i\left\{\frac{J_n(\xi)}{H_n^{(1)}(\xi)}-a_{nl}\frac{W_n}{D_n}\right\}\xi H_n^{(1)'}(\xi)+...$$

$$...+a_{nl}\frac{\xi^2}{\eta^2}\frac{H_n^{(1)}(\xi)}{J_n(\eta)}n\cos\zeta J_n(\eta)-...$$

$$\ldots -i\frac{m\xi^2}{\eta^2 J_n(\eta)}\left[J_n(\xi)-\left(\frac{J_n(\xi)}{H_n^{(1)}(\xi)}-a_{nl}\frac{W_n}{D_n}\right)H_n^{(1)}(\xi)\right]m\eta J_n'(\eta)=0$$

Simplifying and grouping terms,

$$\left[i\xi J_n'(\xi)-i\xi\frac{J_n(\xi)}{H_n^{(1)}(\xi)}H_n^{(1)'}(\xi)\right]+a_{nl}\left[-n\cos\zeta H_n^{(1)}(\xi)+i\xi\frac{W_n}{D_n}H_n^{(1)'}(\xi)+\ldots\right.$$

$$\left.\ldots +\frac{\xi^2}{\eta^2}n\cos\zeta H_n^{(1)}(\xi)-i\frac{m^2\xi^2}{\eta}\frac{H_n^{(1)}(\xi)J_n'(\eta)}{J_n(\eta)}\frac{W_n}{D_n}\right]=0$$

Thus,

$$a_{nl}=\frac{\left[-i\xi J_n'(\xi)+i\xi\frac{J_n(\xi)}{H_n^{(1)}(\xi)}H_n^{(1)'}(\xi)\right]}{-n\cos\zeta H_n^{(1)}(\xi)+i\xi H_n^{(1)'}(\xi)\frac{W_n}{D_n}+\frac{\xi^2}{\eta^2}n\cos\zeta H_n^{(1)}(\xi)-i\frac{m^2\xi^2}{\eta}\frac{H_n^{(1)}(\xi)J_n'(\eta)}{J_n(\eta)}\frac{W_n}{D_n}}$$

If we multiply the numerator and denominator by $i\eta J_n(\eta)D_n$ and rearrange, we obtain,

$$a_{nl}=\frac{\xi\eta J_n'(\xi)J_n(\eta)D_n-\xi\eta\frac{J_n(\xi)}{H_n^{(1)}(\xi)}H_n^{(1)'}(\xi)J_n(\eta)D_n}{in\cos\zeta\eta H_n^{(1)}(\xi)J_n(\eta)\left[\frac{\xi^2}{\eta^2}-1\right]D_n+\xi\left[m^2\xi H_n^{(1)}(\xi)J_n'(\eta)-\eta H_n^{(1)'}(\xi)J_n(\eta)\right]W_n}$$

In the denominator we can observe D_n appears once again. In addition, we define,

$$V_n=\xi\left[m^2\xi H_n^{(1)}(\xi)J_n'(\eta)-\eta H_n^{(1)'}(\xi)J_n(\eta)\right]$$

Thus, the denominator becomes,

$$=in\cos\zeta\eta H_n^{(1)}(\xi)J_n(\eta)\left[\frac{\xi^2}{\eta^2}-1\right]D_n+\xi\left[m^2\xi H_n^{(1)}(\xi)J_n'(\eta)-\eta H_n^{(1)'}(\xi)J_n(\eta)\right]W_n$$

$$=W_nV_n+iD_n^2$$

For the numerator, if we expand D_n in the first term, we obtain,

$$=\xi\eta J_n'(\xi)J_n(\eta)D_n-\xi\eta\frac{J_n(\xi)}{H_n^{(1)}(\xi)}H_n^{(1)'}(\xi)J_n(\eta)n\cos\zeta\eta H_n^{(1)}(\xi)J_n(\eta)\left[\frac{\xi^2}{\eta^2}-1\right]$$

$$=\xi\eta J_n'(\xi)J_n(\eta)D_n-\xi\eta H_n^{(1)'}(\xi)J_n(\eta)n\cos\zeta\eta J_n(\xi)J_n(\eta)\left[\frac{\xi^2}{\eta^2}-1\right]$$

If we define,

$$C_n = n\cos\zeta\eta J_n(\xi)J_n(\eta)\left[\frac{\xi^2}{\eta^2}-1\right]$$

Then,

$$= \xi\eta J_n'(\xi)J_n(\eta)D_n - \xi\eta H_n^{(1)'}(\xi)J_n(\eta)C_n$$

In addition, we find that C_n and D_n are related by,

$$H_n^{(1)}(\xi)C_n = J_n(\xi)D_n \tag{2.77}$$

Now if we add the following terms to the numerator and use (2.77),

$$= \xi\eta J_n'(\xi)J_n(\eta)D_n - \xi\eta H_n^{(1)'}(\xi)J_n(\eta)C_n + m^2\xi^2 J_n'(\eta)H_n^{(1)}(\xi)C_n - ...$$

$$... - m^2\xi^2 J_n'(\eta)H_n^{(1)}(\xi)C_n$$

$$= \xi\left[m^2\xi J_n'(\eta)H_n^{(1)}(\xi) - \eta H_n^{(1)'}(\xi)J_n(\eta)\right]C_n - \xi\left[m^2\xi J_n'(\eta)J_n(\xi) - \eta J_n'(\xi)J_n(\eta)\right]D_n$$

Now V_n appears in the numerator. If we define,

$$B_n = \xi\left[m^2\xi J_n'(\eta)J_n(\xi) - \eta J_n'(\xi)J_n(\eta)\right]$$

The numerator becomes,

$$= C_nV_n - B_nD_n$$

Therefore, a_{nl} is thus equal to,

$$a_{nl} = \frac{C_nV_n - B_nD_n}{W_nV_n + iD_n^2}$$

Now if we substitute back into (2.76), we can find b_{nl},

$$b_{nl} = \frac{J_n(\xi)}{H_n^{(1)}(\xi)} - \frac{C_nV_n - B_nD_n}{W_nV_n + iD_n^2}\frac{W_n}{D_n}$$

$$= \frac{J_n(\xi)}{H_n^{(1)}(\xi)}\frac{W_nV_n + iD_n^2}{W_nV_n + iD_n^2} - \frac{C_nV_n\dfrac{W_n}{D_n} - W_nB_n}{W_nV_n + iD_n^2}$$

$$= \frac{\dfrac{J_n(\xi)}{H_n^{(1)}(\xi)}W_nV_n + i\dfrac{J_n(\xi)}{H_n^{(1)}(\xi)}D_n^2 - C_nV_n\dfrac{W_n}{D_n} + W_nB_n}{W_nV_n + iD_n^2}$$

If we again use (2.77),

$$= \frac{\dfrac{C_n}{D_n} W_n V_n + iC_n D_n - C_n V_n \dfrac{W_n}{D_n} + W_n B_n}{W_n V_n + iD_n^2}$$

Thus,

$$b_{nI} = \frac{W_n B_n + iC_n D_n}{W_n V_n + iD_n^2}$$

After wading through all the algebra, we finally obtain the unknown coefficients and thus the field solutions surrounding the cylinder. To summarize,

$$a_{nI} = \frac{C_n V_n - B_n D_n}{W_n V_n + iD_n^2}, b_{nI} = \frac{W_n B_n + iC_n D_n}{W_n V_n + iD_n^2} \tag{2.78}$$

where,

$$B_n = \xi \left[m^2 \xi J_n'(\eta) J_n(\xi) - \eta J_n'(\xi) J_n(\eta) \right]$$

$$C_n = n\cos\zeta \eta J_n(\xi) J_n(\eta) \left[\frac{\xi^2}{\eta^2} - 1 \right]$$

$$D_n = n\cos\zeta \eta H_n^{(1)}(\xi) J_n(\eta) \left[\frac{\xi^2}{\eta^2} - 1 \right]$$

$$V_n = \xi \left[m^2 \xi H_n^{(1)}(\xi) J_n'(\eta) - \eta H_n^{(1)'}(\xi) J_n(\eta) \right]$$

$$W_n = i\xi \left[\eta H_n^{(1)'}(\xi) J_n(\eta) - \xi H_n^{(1)}(\xi) J_n'(\eta) \right]$$

and,

$$x = ka$$

$$\xi = x\sin\zeta$$

$$\eta = x\sqrt{m^2 - \cos^2\zeta}$$

Properties of Coefficients

Now that we have the field solutions, the next step is to derive the efficiencies. However, at this juncture, it would be appropriate to note a few useful properties in the coefficients in (2.78) to aide us in this endeavor. In general, the two Bessel functions exhibit the following properties,

$$J_{-n} = (-1)^n J_n, \quad Y_{-n} = (-1)^n Y_n$$

54

From these properties, the following holds true,

$$a_{-nl} = -a_{nl}, \quad b_{-nl} = b_{nl} \tag{2.79}$$

In addition, it can be observed from (2.78) that when $n = 0$,

$$a_{0l} = 0 \tag{2.80}$$

2.1.6 Derivation of Efficiencies

General Formulation

Now that we have solutions to the fields in the system, we can determine the Poynting vector at all positions in the system thus giving us information on the rate of energy scattered and absorbed by the cylinder. From this we can determine the efficiencies of the cylinder. To start, we first formulate the Poynting vectors needed for this analysis. The Poynting vector at any point in the medium outside the particle can be written as,

$$\mathbf{S} = \frac{1}{2} \text{Re}\left\{\mathbf{E}_2 \times \mathbf{H}_2^*\right\}$$

$$\mathbf{S} = \frac{1}{2} \text{Re}\left\{\mathbf{E}_i \times \mathbf{H}_i^* + \mathbf{E}_s \times \mathbf{H}_s^* + \left(\mathbf{E}_i \times \mathbf{H}_s^* + \mathbf{E}_s \times \mathbf{H}_i^*\right)\right\} = \mathbf{S}_i + \mathbf{S}_s + \mathbf{S}_{ext} \tag{2.81}$$

where we have decomposed the total Poynting vector as a sum of three terms: $\mathbf{S}_i$ is the Poynting vector due to the incident field, $\mathbf{S}_s$ is the Poynting vector due to the scattered field and $\mathbf{S}_{ext}$ is the Poynting vector that arises from the interaction between the incident and scattered fields. The subscript *ext* denotes extinction. Note that in order to determine all the efficiencies of the particle we only need to consider the fields outside the particle. To demonstrate why this is possible, we define the total absorbed power in an imaginary concentric cylinder of radius R to be,

$$W_a = -\int_A \mathbf{S} \cdot \hat{\mathbf{r}} \, dA \tag{2.82}$$

where we assume $r \gg a$ to ensure that we are in the far-field regime. Since the medium is assumed to be non-absorbing, the total absorbed power is in fact the absorbed power by the cylinder. If we expand (2.82) using (2.81),

$$W_a = \underbrace{-\int_A \mathbf{S}_i \cdot \hat{\mathbf{r}} \, dA}_{0} - \int_A \mathbf{S}_s \cdot \hat{\mathbf{r}} \, dA - \int_A \mathbf{S}_{ext} \cdot \hat{\mathbf{r}} \, dA = \underbrace{W_i}_{0} - W_s + W_{ext} \tag{2.83}$$

55

The contribution by the incident field to the total absorbed power, W_i, as shown in (2.83) is zero for a non-absorbing medium since this contribution does not include the presence of the cylinder. Thus, upon rearranging the terms,

$$W_{ext} = W_s + W_a \tag{2.84}$$

where,

$$W_s = \int_A \mathbf{S}_s \cdot \hat{\mathbf{r}} \, dA \tag{2.85}$$

$$W_{ext} = -\int_A \mathbf{S}_{ext} \cdot \hat{\mathbf{r}} \, dA \tag{2.86}$$

From (2.84-2.86) we find that the efficiencies are,

$$Q_{sca} = \frac{W_s}{GI_i}, \quad Q_{ext} = \frac{W_{ext}}{GI_i}, Q_{abs} = Q_{ext} - Q_{sca} \tag{2.87}$$

where G is the geometric cross section of the cylinder and I_i is the incident intensity.

Derivation of Efficiencies

To determine the particular solutions to the efficiencies for a cylinder, we merely need to use the field solutions we derived in Sec. 2.1.5 and follow the procedure outlined above. To start, we derive the scattering efficiency, $Q_{sca,I}$, by determining the Poynting vector of the scattered field, $\mathbf{S}_s$, from (2.81),

$$\mathbf{S}_s = \frac{1}{2} \mathrm{Re} \left\{ \mathbf{E}_s \times \mathbf{H}_s^* \right\}$$

$$\mathbf{S}_{sI} = \frac{1}{2} \mathrm{Re} \left\{ -\sum_{n=-\infty}^{\infty} E_n \left[ia_{nI} \mathbf{M}_n^{(3)} + b_{nI} \mathbf{N}_n^{(3)} \right] \times \frac{-ik}{\omega\mu} \sum_{n=-\infty}^{\infty} E_n^* \left[-ia_{nI}^* \mathbf{N}_n^{(3)*} + b_{nI}^* \mathbf{M}_n^{(3)*} \right] \right\}$$

For now, we shall assume a particular n to simplify the derivation. In addition, from (2.85), we only need to consider the r component. Thus,

$$(\mathbf{S}_{sI})_{r,n} = \frac{1}{2} \mathrm{Re} \left\{ i \frac{|E_n|^2 k}{\omega\mu} \left[|a_{nI}|^2 \left(\mathbf{M}_n^{(3)} \times \mathbf{N}_n^{(3)*} \right)_r + ia_{nI} b_{nI}^* \left(\mathbf{M}_n^{(3)} \times \mathbf{M}_n^{(3)*} \right)_r - \dots \right. \right.$$

$$\left. \left. \dots - ia_{nI}^* b_{nI} \left(\mathbf{N}_n^{(3)} \times \mathbf{N}_n^{(3)*} \right)_r + |b_{nI}|^2 \left(\mathbf{N}_n^{(3)} \times \mathbf{M}_n^{(3)*} \right)_r \right] \right\}$$

Therefore, we need to solve the cross products of the vector harmonics. We can immediately observe that the cross product of the vector harmonic with its complex conjugate will equal zero. For the other terms,

$$\left(\mathbf{M}_n^{(3)}\times\mathbf{N}_n^{(3)*}\right)_r = \sqrt{k^2-h^2}\left[i\frac{n}{\rho}H_n^{(1)}(\rho)\hat{\mathbf{r}}-H_n^{(1)'}(\rho)\hat{\boldsymbol{\varphi}}\right]e^{i(n\varphi+hz)}\times\dots$$

$$\dots\times\frac{\sqrt{k^2-h^2}}{k}\left[-ihH_n^{(1)'*}(\rho)\hat{\mathbf{r}}-nh\frac{H_n^{(1)*}(\rho)}{\rho}\hat{\boldsymbol{\varphi}}+\sqrt{k^2-h^2}H_n^{(1)*}(\rho)\hat{\mathbf{z}}\right]e^{-i(n\varphi+hz)}$$

$$\rightarrow\left(\mathbf{M}_n^{(3)}\times\mathbf{N}_n^{(3)*}\right)_r = -\frac{\left(k^2-h^2\right)^{\frac{3}{2}}}{k}H_n^{(1)'}(\rho)H_n^{(1)*}(\rho)$$

$$\left(\mathbf{N}_n^{(3)}\times\mathbf{M}_n^{(3)*}\right)_r = \frac{\sqrt{k^2-h^2}}{k}\left[ihH_n^{(1)'}(\rho)\hat{\mathbf{r}}-nh\frac{H_n^{(1)}(\rho)}{\rho}\hat{\boldsymbol{\varphi}}+\sqrt{k^2-h^2}H_n^{(1)}(\rho)\hat{\mathbf{z}}\right]e^{i(n\varphi+hz)}\times\dots$$

$$\dots\times\sqrt{k^2-h^2}\left[-i\frac{n}{\rho}H_n^{(1)*}(\rho)\hat{\mathbf{r}}-H_n^{(1)'*}(\rho)\hat{\boldsymbol{\varphi}}\right]e^{-i(n\varphi+hz)}$$

$$\rightarrow\left(\mathbf{N}_n^{(3)}\times\mathbf{M}_n^{(3)*}\right)_r = \frac{\left(k^2-h^2\right)^{\frac{3}{2}}}{k}H_n^{(1)'*}(\rho)H_n^{(1)}(\rho)$$

Thus,

$$\left(\mathbf{S}_{sl}\right)_{r,n} = \frac{1}{2}\mathrm{Re}\left\{i\frac{|E_n|^2\left(k^2-h^2\right)^{\frac{3}{2}}}{\omega\mu}\left[-|a_{nl}|^2\,H_n^{(1)'}(\rho)H_n^{(1)*}(\rho)+|b_{nl}|^2\,H_n^{(1)'*}(\rho)H_n^{(1)}(\rho)\right]\right\}$$

We can now use the asymptotic solution to the Hankel function to simplify the expression,

$$H_n^{(1)}(\rho_s)\sim\sqrt{\frac{2}{\pi\rho_s}}e^{i\rho_s}\left(-i\right)^n e^{-i\pi/4}$$

The derivative is,

$$H_n^{(1)'}(\rho_s)\sim\left(-i\right)^n e^{-i\pi/4}\left(i\sqrt{\frac{2}{\pi\rho_s}}e^{i\rho_s}-\frac{1}{2}\sqrt{\frac{2}{\pi\rho_s}}\frac{1}{\rho_s}e^{i\rho_s}\right)$$

Thus,

$$H_n^{(1)'}(\rho)H_n^{(1)*}(\rho) = \left(-i\right)^n e^{-i\pi/4}\left(i\sqrt{\frac{2}{\pi\rho_s}}e^{i\rho_s}-\frac{1}{2}\sqrt{\frac{2}{\pi\rho_s}}\frac{1}{\rho_s}e^{i\rho_s}\right)\cdot\sqrt{\frac{2}{\pi\rho_s}}e^{-i\rho_s}\left(i\right)^n e^{i\pi/4}$$

$$\rightarrow H_n^{(1)\prime}(\rho)H_n^{(1)*}(\rho) = \frac{2}{\pi\rho_s}\left(i - \frac{1}{2\sqrt{\rho_s}}\right)$$

$$H_n^{(1)\prime*}(\rho)H_n^{(1)}(\rho) = (i)^n e^{i\pi/4}\left(-i\sqrt{\frac{2}{\pi\rho_s}}e^{-i\rho_s} - \frac{1}{2}\sqrt{\frac{2}{\pi\rho_s}}\frac{1}{\rho_s}e^{-i\rho_s}\right)\cdot\sqrt{\frac{2}{\pi\rho_s}}e^{i\rho_s}(-i)^n e^{-i\pi/4}$$

$$\rightarrow H_n^{(1)\prime*}(\rho)H_n^{(1)}(\rho) = -\frac{2}{\pi\rho_s}\left(i + \frac{1}{2\rho_s}\right)$$

Substituting,

$$\left(\mathbf{S}_{sl}\right)_{r,n} = \frac{1}{2}\mathrm{Re}\left\{i\frac{|E_n|^2\left(k^2-h^2\right)^{\frac{3}{2}}}{\omega\mu}\left[-|a_{nl}|^2\frac{2}{\pi\rho_s}\left(i-\frac{1}{2\sqrt{\rho_s}}\right)-|b_{nl}|^2\frac{2}{\pi\rho_s}\left(i+\frac{1}{2\rho_s}\right)\right]\right\}$$

Taking only the real component yields,

$$\left(\mathbf{S}_{sl}\right)_{r,n} = \frac{|E_n|^2\left(k^2-h^2\right)^{\frac{3}{2}}}{\pi\rho_s\omega\mu}\left(|a_{nl}|^2+|b_{nl}|^2\right)$$

Substituting in for E_n, h, and ρ_s leads to,

$$\left(\mathbf{S}_{sl}\right)_{r,n} = \frac{E_0^2}{\pi\omega\mu R}\left(|a_{nl}|^2+|b_{nl}|^2\right)$$

We can also define the incident intensity to be,

$$I_i = \frac{E_0^2}{2\mu c} \tag{2.88}$$

Upon substituting (2.88) and using the definition for the speed of light, c, and the wave vector, k, we find the scattered Poynting vector to be,

$$\left(\mathbf{S}_{sl}\right)_r = \frac{2I_i}{\pi k R}\sum_{n=-\infty}^{\infty}\left(|a_{nl}|^2+|b_{nl}|^2\right) \tag{2.89}$$

where we are now looking at all possible n. Now if we plug (2.89) into (2.85), we find the total scattered power to be,

$$W_{sl} = RL\int_0^{2\pi}\frac{2I_i}{\pi k R}\sum_{n=-\infty}^{\infty}\left(|a_{nl}|^2+|b_{nl}|^2\right)d\phi$$

$$W_{sl} = \frac{4LI_i}{k}\sum_{n=-\infty}^{\infty}\left(|a_{nl}|^2+|b_{nl}|^2\right) \tag{2.90}$$

58

From the definition of the scattering efficiency (2.87),

$$Q_{sca,I} = \frac{\frac{4LI_i}{k} \sum_{n=-\infty}^{\infty} \left(|a_{nI}|^2 + |b_{nI}|^2 \right)}{2aLI_i}$$

$$Q_{sca,I} = \frac{2}{x} \sum_{n=-\infty}^{\infty} \left(|a_{nI}|^2 + |b_{nI}|^2 \right)$$

Using the properties of the coefficients (2.79, 2.80), we can write,

$$Q_{sca,I} = \frac{2}{x} \left[|b_{0I}|^2 + 2\sum_{n=1}^{\infty} \left(|a_{nI}|^2 + |b_{nI}|^2 \right) \right] \tag{2.91}$$

We can derive the extinction efficiency in a similar manner using the asymptotic solution to the Bessel functions of the first and second kind,

$$J_n(\rho) \sim \sqrt{\frac{2}{\pi\rho}} \cos\left(\rho - \frac{n\pi}{2} - \frac{\pi}{4} \right)$$

$$Y_n(\rho) \sim \sqrt{\frac{2}{\pi\rho}} \sin\left(\rho - \frac{n\pi}{2} - \frac{\pi}{4} \right)$$

We find the extinction efficiency to be,

$$Q_{ext,I} = \frac{2}{x} \mathrm{Re}\left(b_{0I} + 2\sum_{n=1}^{\infty} b_{nI} \right) \tag{2.92}$$

Now that we have the scattering and extinction efficiency we can determine the absorption efficiency from (2.87). In order to utilize these expressions to calculate efficiencies for different materials, we must approximate the Bessel functions using upward and downward recurrence relations. Additionally, the number of terms n we consider is dependent on the size of the object. More information regarding the numerical calculation can be found in the appendices of Bohren and Huffman.[6]

2.1.7 Perpendicular Polarization

As mentioned before, the problem of light interacting with a cylinder includes two possible polarizations. Until now, we have dealt only with light that is polarized parallel to the cylinder axis, case I. Given that we have all the necessary knowledge to derive the efficiencies, the results will be summarized for the perpendicular polarization. Recall from (2.5) that the incident field in this case is of the form,

$$\mathbf{E}_{i,II} = E_0 \left(\sin\varphi \, \hat{\mathbf{r}} + \cos\varphi \, \hat{\boldsymbol{\varphi}} \right) e^{-ik(r\sin\zeta\cos\varphi + z\cos\zeta)}$$

If we expand the field in the same manner as the first case, we will find that,

$$\mathbf{E}_{i,II} = -i \sum_{n=-\infty}^{\infty} E_n \mathbf{M}_n^{(1)}, \qquad \mathbf{H}_{i,II} = -\frac{k}{\omega\mu} \sum_{n=-\infty}^{\infty} E_n \mathbf{N}_n^{(1)} \tag{2.93}$$

Upon applying boundary conditions, we find the coefficients to be,

$$a_{nII} = -\frac{A_n V_n - i C_n D_n}{W_n V_n + i D_n^2}, \qquad b_{nII} = -i \frac{C_n W_n + A_n D_n}{W_n V_n + i D_n^2} \tag{2.94}$$

where,

$$A_n = i\xi \left[\xi J_n'(\eta) J_n(\xi) - \eta J_n(\eta) J_n'(\xi) \right]$$

All other terms are the same as before for case I. We can again observe some notable properties in the coefficients,

$$a_{-nII} = a_{nII}, \qquad b_{-nII} = -b_{nII}, \qquad b_{0II} = 0 \tag{2.95}$$

Following the derivation of the efficiencies, we obtain the following,

$$Q_{sca,II} = \frac{2}{x} \left[|a_{0II}|^2 + 2\sum_{n=1}^{\infty} \left(|a_{nII}|^2 + |b_{nII}|^2 \right) \right] \tag{2.96}$$

$$Q_{ext,II} = \frac{2}{x} \text{Re} \left(a_{0II} + 2\sum_{n=1}^{\infty} a_{nII} \right) \tag{2.97}$$

We may also define the efficiencies for unpolarized light. This is simply the average of both polarizations using (2.91, 2.92) and (2.96, 2.97),

$$Q_{sca} = \frac{1}{2} \left(Q_{sca,I} + Q_{sca,II} \right) \tag{2.98}$$

$$Q_{ext} = \frac{1}{2} \left(Q_{ext,I} + Q_{ext,II} \right) \tag{2.99}$$

Based on the formulation of the efficiencies for both polarizations, we now have all the necessary tools to compute theoretical solutions for silicon nanowires. We again note that the code used for this calculation is based on the code provided in Bohren and Huffman translated to MATLAB.

60

2.2 Mie Theory Results for a Silicon Wire

Using the derived expressions for the Mie coefficients and the efficiencies in Sec. 2.1.5 through Sec. 2.1.7, the absorption efficiency of a silicon nanowire was calculated as a function of wavelength and radius. The wavelength was chosen to span from 300 nm to 1000 nm to capture the resonant mode enhancement in the visible and near-infrared spectrum. The radius is chosen to range from 10 nm to 500 nm. The purpose of calculating the absorption efficiency in this manner is to determine regions where enhancement occurs as well as how it changes as a function of wavelength and size. And finally, the optical constants for silicon must be specified within this wavelength range. The optical constants were obtained from the Handbook of Optical Constants[57] for intrinsic silicon are assumed to be temperature independent in the experiment. We note that the dopant concentration of the silicon nanowires used in the experiment is sufficiently low ($n < 10^{16}$) to validate the use of this data. In addition, we neglect surface roughness and assume the nanowire is homogenous. The refractive index of the surrounding medium is assumed to be unity.

The results for parallel and perpendicular polarizations are shown in Fig. 2.3 for the case of normal incidence illumination,
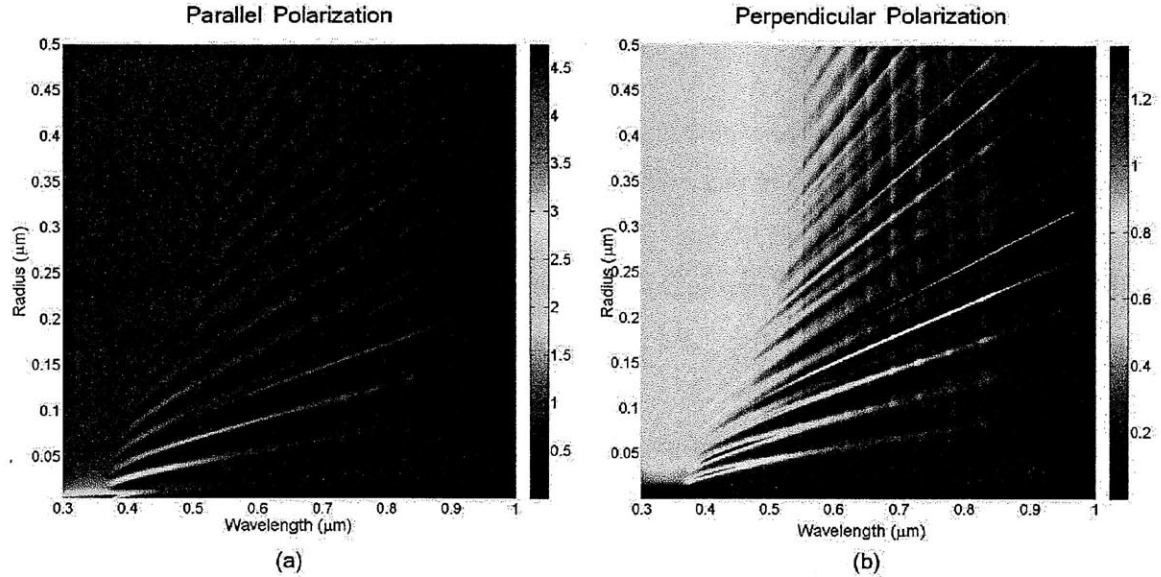
Figure 2.3: The spectral absorption efficiency, Q_{abs}, of a silicon nanowire for (a) parallel polarization and (b) perpendicular polarization at normal incidence. Note that polarization is relative to the wire axis.

From Fig. 2.3, we can observe the presence of several absorption peaks in the visible wavelength spectrum for both polarizations which corresponds to the leaky mode resonances supported in a silicon nanowire. In Fig. 2.3a, the strongest resonance for parallel polarization occurs at the lowest order mode, or Fröhlich mode, at a radius of $r = 5 \sim 8$ nm in the UV spectrum as predicted by equation (2.1) for a particle operating in the Rayleigh limit. This indicates that for very small nanowires, the dipole-field, as mentioned in Sec. 2.1, is approaching the behavior of an ideal electrostatic point dipole source. This implies the field inside the wire is uniform. As the size increases, the nanowire is able to support additional higher order leaky mode resonances in the visible wavelength spectrum. And as one would expect in a classic resonator, the higher order modes progressively lose their dipole-like behavior which ultimately results in weaker absorption.[6, 17] A similar trend can be observed for perpendicular polarization in Fig. 2.3b. In this case however, the second order mode is actually stronger than the first order mode. This is due to the field distribution in the second order mode taking a more dipole-like form compared to the first order mode. In both cases, these leaky mode resonances also exhibit a red shift as the

size of the nanowire increases. This is due to finite size effects where the Rayleigh limit is no longer applicable. It should be noted that the size independent fluctuations at the longer wavelengths are due to the optical constants used and are thus non-physical.

For the experiment conducted in this study, the light source used in the experimental setup emits unpolarized light. This will be verified in Ch. 4, Sec. 4.1.3. To determine the corresponding plot for unpolarized illumination, we simply need to average the parallel and perpendicular polarizations according to (2.98) and (2.99). The results are thus shown in Fig. 2.4,
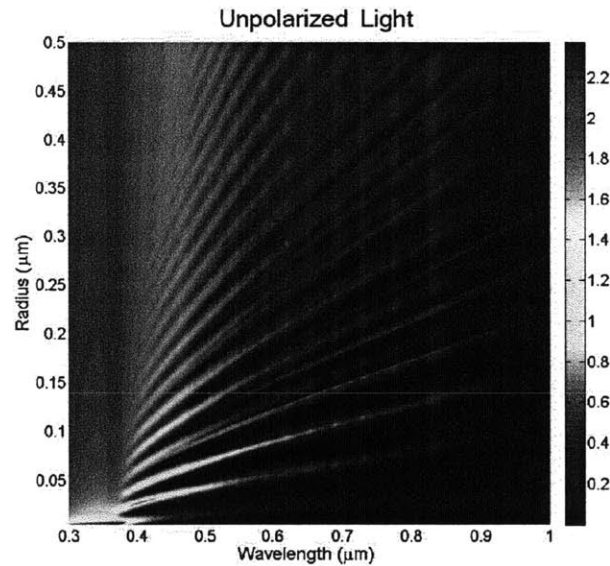
Figure 2.4: The spectral absorption efficiency, Q_{abs}, of a silicon nanowire for unpolarized illumination at normal incidence.

As expected, the same trends observed for each polarization is retained in Fig. 2.4 after averaging both polarizations. Therefore, to measure an absorption efficiency greater than 1, the size of the silicon nanowire must be small enough to capture the lower order modes at their peaks. To convey this behavior more clearly, Fig. 2.5 shows the efficiencies for silicon wire at a fixed wavelength and a fixed radius,
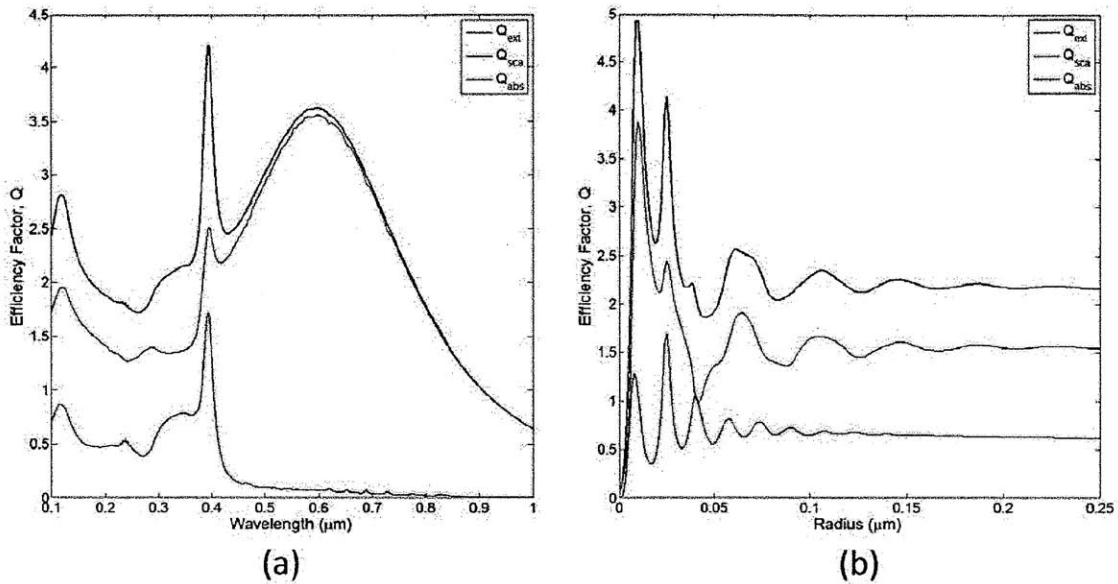
Figure 2.5: The efficiencies of a silicon wire for the following fixed parameters: (a) $R = 25\ \text{nm}$, (b) $\lambda = 392\ \text{nm}$. From (a) it can be seen that the absorption efficiency is greater than 1 in the UV range. In (b), the absorption efficiency acquires additional modes which gradually lose their dipole like behavior as the radius of the wire increases.

According to Fig. 2.4, the size of the nanowire must range from $r = 5\ \text{nm}$ to $r = 75\ \text{nm}$. However, since this experiment, as will be discussed in Ch. 3, is limited by the sensitivity of the system, the actual nanowire measured is much larger in size ($r \approx 500\ \text{nm}$). This is primarily for experimental convenience and serves as a means to validate the experimental approach taken in this study. However, it should be emphasized this is merely an intermediate step as the ultimate goal is to probe the unique optical properties of smaller radii silicon nanowires, as shown in Figs. 2.4 and 2.5.

2.3 Summary

In summary, Ch. 2 established the theoretical foundation to describe the optical properties of individual nanowires. Although the Rayleigh approximation is valid for particles exhibiting small size parameters, the well known Mie theory is used to discern potential trends in the absorption efficiency at all size parameters. A complete derivation of Mie theory for infinitely long cylindrical particles is provided. This was followed by a set of theoretical results specific to

silicon nanowires. As observed, it is possible to theoretically assess the size of the nanowire needed to maximize the absorption efficiency at a particular wavelength. These results will be used to compare experimental data in Ch. 4.

Chapter 3

Experimental Investigation

The use of atomic force microscope (AFM) cantilever thermometry can enable the direct and quantitative measure of the absorption efficiency. This is achieved by using a cantilever to measure the radiative energy absorbed by a Si nanowire when illuminated by monochromatic light. Coupled with the inherent high sensitivity of the sensor, this platform can be used to probe optical phenomena on nanometer-sized particles. In this chapter, a general overview of the experiment will be provided. It will begin with a general review on the theory behind the use of an AFM cantilever as a thermal sensor. This will be followed by a brief overture on the synthesis of the Si nanowires used in this experiment. Then, the process of attaching a nanowire to a cantilever will be described. And finally, the experimental technique will be discussed. This will include a general overview of the technique itself, the particular components used in the measurement platform and the calibrations needed to extract the absorption efficiency from the data measured.

3.1 Cantilever Theory

In this experiment, a bimorph AFM cantilever is used as a thermal sensor. These cantilevers are typically composed of two layers of materials with different thermal expansion coefficients. A variety of materials can be used. However, the most common consist of a substrate of either silicon nitride or silicon and a reflecting layer of either gold or aluminum. The deflection response of the cantilever due to a thermal expansion mismatch can be used to measure the heat transfer through the cantilever. The cantilever chip can be modeled as a thermal reservoir. As a result, the base temperature is constant. However, the tip temperature will be proportional to the cantilever deflection. If the thermal conductance of the cantilever is known, the heat flux can then be measured based on these two temperatures. Therefore, based on this principle and with proper calibration, these cantilevers can be used as both a temperature and a heat flux sensor.[32] As a point of emphasis, it is quite uncommon in the realm of thermal

sensors for there to be a sensor capable of simultaneously measuring both temperature and heat flux while neatly packaged as a single device. To measure this bending response, we use an optical detection scheme consisting of a laser reflected off the tip of the cantilever onto a position sensitive detector (PSD). When the cantilever bends, this will cause the beam spot to shift on the PSD. This shift is thus correlated with the thermal input on the cantilever. It should be noted that increasing the distance between the cantilever and the PSD will amplify the sensitivity of the system. However, this amplification is ultimately limited by the increasing beam spot size incident on the PSD.

In this particular study, we use a bimorph cantilever as a photodetector to measure the absorption efficiency of Si nanowires. Hence, we use the cantilever solely as a heat flux sensor. The particular cantilever used is a NanoWorld pyrex nitride gold coated tipless triangular cantilever (Nanoworld PNP-TR-TL-Au). This cantilever is 200 μm long and each leg is 28 μm wide. The nitride substrate is 540 nm thick and the gold coating is 60 nm thick. Figure 3.1 is an image of the cantilever as viewed under a microscope,
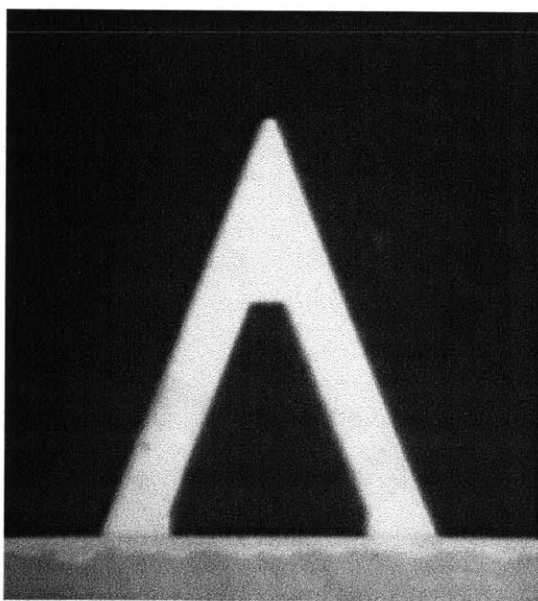
Figure 3.1: Optical microscope image of an AFM bimorph cantilever (Nanoworld PNP-TR-TL-Au). The image is taken viewing the SiN$_x$ side.

The manner in which we extract heat flux data from the bending response of the cantilever is based on a coupling of the heat conduction equation with beam theory. In the following analysis, we shall assume for the sake of simplicity that the cantilever is rectangular. This assumption was shown to be a good approximation.[28, 29] Radiation losses are also assumed to be negligible due to small changes in temperature during the experiment. Figure 3.2 shows the coordinate system we shall adopt in this analysis,
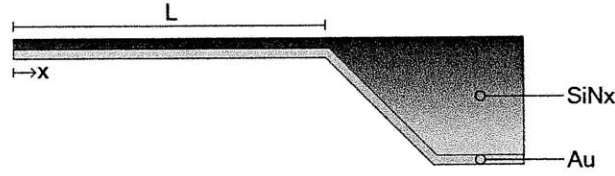
Figure 3.2: Coordinate system used in the analysis of a bimorph AFM cantilever.

where x is the position along the cantilever and L is the length of the cantilever.

From beam theory, the deflection of the cantilever can be determined by the following differential equation,[28, 58-60]

$$\frac{d^2 z(x)}{dx^2} = 6(\gamma_2 - \gamma_1)\frac{t_1 + t_2}{t_2^2 K}(T(x) - T_0) \qquad (3.1)$$

where,

$$K = 4 + 6\left(\frac{t_1}{t_2}\right) + 4\left(\frac{t_1}{t_2}\right)^2 + \frac{E_1}{E_2}\left(\frac{t_1}{t_2}\right)^3 + \frac{E_2}{E_1}\left(\frac{t_2}{t_1}\right)$$

In (3.1), $z(x)$ is the deflection of the cantilever at point x along the cantilever, $T(x)$ is the temperature distribution at point x along the cantilever, T_0 is the reference temperature at zero deflection, γ is the thermal expansion coefficient, t is the thickness of the layers and E is the Young's modulus of the layers. Based on the form of (3.1), we have neglected heat conduction in the thickness direction by virtue of the aspect ratio of the cantilever where the length is substantially larger than the thickness.

To solve (3.1), we must constrain the base of the cantilever. The boundary condition becomes the following,

BC 1: $\dfrac{dz(x=L)}{dx}=0$ (3.2)

We note here that we only solve for the slope of the bending response because the optical detection scheme we employ is determined by changes in slope rather than changes in deflection.

In addition, we must determine the temperature profile along the cantilever. This will be dependent on the heating condition we impose in the experiment. The laser we use to measure the bending response will cause heating at the tip of the cantilever. In addition, light absorbed by the nanowire will conduct as heat from the tip of the cantilever to its base. Therefore, we can assume all heating occurs at the tip of the cantilever. Although the laser spot on the cantilever is finite in size, it has been previously shown that this approximation will lead to a negligible difference provided that the laser spot is much smaller than the length of the cantilever.[40] Since the experiment is conducted in vacuum, the heat equation consists of the following form,

$$\dfrac{d^2T(x)}{dx^2}=0$$ (3.3)

The boundary conditions are,

BC 1: $\dfrac{dT(x=0)}{dx}=-\dfrac{P}{kA}$ (3.4)

BC 2: $T(x=L)=T_0$ (3.5)

where P is the absorbed power at the tip of the cantilever, k is the effective thermal conductivity and A is the cross section. Upon solving (3.3) using (3.4) and (3.5), we obtain,

$$T(x)-T_0=\dfrac{P}{G}\left(1-\dfrac{x}{L}\right)$$ (3.6)

where G is the thermal conductance of the cantilever. Now if we input (3.6) into (3.1) and solve, we will find the slope to be,

$$\dfrac{dz(x)}{dx}=6H\dfrac{P}{G}\left(x-\dfrac{x^2}{2L}-\dfrac{L}{2}\right)$$ (3.7)

where $H=(\gamma_2-\gamma_1)(t_1+t_2)/t_2^2K$. Since we only measure changes in slope at the tip, (3.7) becomes,

$$\dfrac{dz(x=0)}{dx}=-3P\dfrac{HL}{G}$$ (3.8)

69

In order to relate the slope to the beam shift on the PSD, we use the following,

$$\frac{dz(x=0)}{dx} = \frac{1}{2}\frac{\Delta d}{s}$$

(3.9)

where Δd is the beam shift on the PSD and s is the distance between the PSD and the cantilever. Therefore, from (3.8) and (3.9),

$$\Delta d = -6sP\frac{HL}{G}$$

(3.10)

Note that we have assumed a small angle approximation by virtue of the small deflections typically observed in the experiment.

From (3.10), we can observe that Δd is the parameter we measure in the experiment. It is directly proportional to the absorbed power P via material and geometric constants in the system. However, since we do not necessarily know the material properties, due to the deposition process and thin-film effects, we must conduct a calibration to account for these unknowns. This will be discussed in Sec. 3.4.3.2.

3.2 Nanowire Synthesis

In this study, Si nanowires were synthesized by Professor Ruiting Zheng at the Beijing Normal University using an electroless etching (EE) technique. This technique has been used to synthesize rough Si nanowires en masse and was made famous by studies on its thermoelectric properties.[61] We exploit the high throughput of this technique to create wires with a wide range of radii including those which theoretically exhibit enhanced absorptive properties, as mentioned in Section 2.2. In this section, a brief overview of the concept behind the technique will be provided. Further information can be found in several works by Peng et al.[62-64]

The foundation of the EE technique is based on the well established electroless metal deposition (EMD) process, typically used in industry for low cost, high quality metal coatings on silicon substrates. This process consists of several simultaneous micro-electro-chemical redox reactions that do not require electrical power input. In this particular work, an n-type silicon wafer was immersed in a solution containing silver nitrate and hydrofluoric acid (HF). Although the wafer is n-type, the dopant concentration is on the order of 10^{16}, thus the silicon is effectively intrinsic. Silver nanoclusters will form on the silicon wafer from the reduction of silver ions in the solution. This reduction is achieved by electron transfer from the HF species. While this

70

reduction occurs, the silicon substrate is simultaneously oxidized. Since HF will etch silicon oxide, the regions of the wafer that are still exposed to the HF solution will etch away. The key to etching silicon nanowires is therefore dependent on controlling this etching process.

In other solutions, such as ammonium fluoride, the silver nanoclusters exhibit a strong tendency to coalesce thus forming a continuous metallic film. This would lead to uniform etching of the wafer. However, in the case of HF, the coalescence of the metallic nanoclusters is offset by the formation of silver dendrites. As additional silver ions are deposited, the film will grow in a fractal manner such that the dendrites retain their form. Therefore, these silver dendrites form a pattern from which selective etching can proceed. It is believed that in the selective etching of silicon, these localized dendritic structures function as individual nanoscale electrolytic cells where the silver acts as a cathode and the silicon as an anode. Thus, as additional silver ions are deposited, only the regions surrounding the silver dendrites are oxidized and removed by the solution. Under proper conditions, this etching will proceed anisotropically leaving behind silver capped nanowires. Finally, any excess silver is etched in a nitric acid bath. Figure 3.3a shows a cross section of various samples made for this project courtesy of Professor Ruiting Zhen. From Fig. 3.3b it can be observed that the chaotic nature of this process has resulted in not only the creation of a variety of nanowires, but also regions of porous silicon. In addition, the length is typically on the order of 100-200 μm,
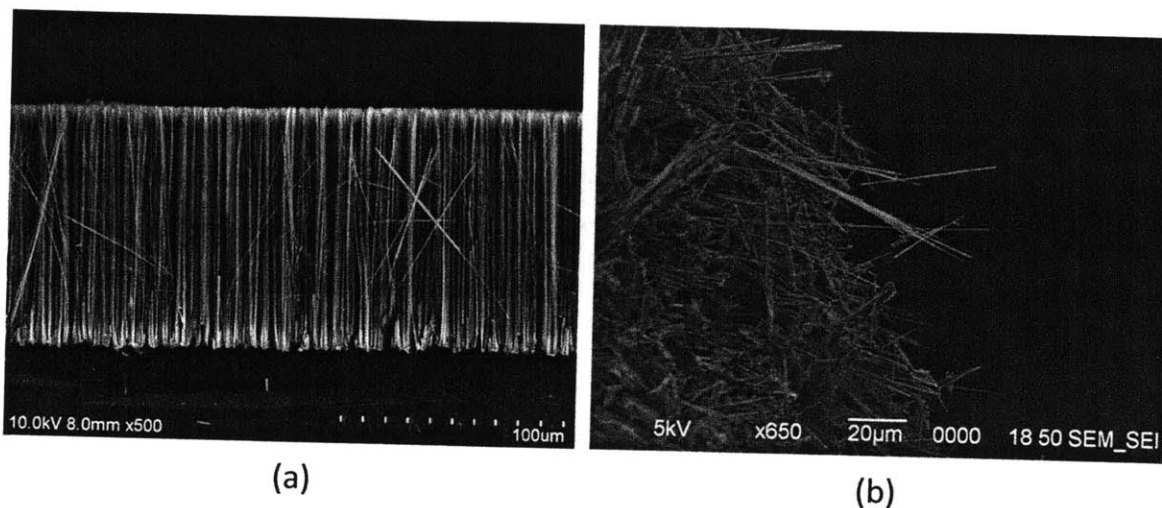
Figure 3.3: (a) A cross section image of a wafer containing Si nanowires synthesized for this study. These nanowires were synthesized with a length of 100-200 µm. (image courtesy of Professor Ruiting Zheng from the Beijing Normal University). (b) A top down view of a sample taken with an SEM. The edge of the sample was intentionally broken to dislodge wires for attachment. However, it can also be observed regions of porous silicon are also present.

3.3 Nanowire Attachment

To directly and quantitatively measure the absorption efficiency of a single nanowire, we must be able to measure the heat absorbed by the nanowire when illuminated by monochromatic light. To do so, we simply attach the nanowire to the cantilever. The nanowire thus functions not only as the absorbing specimen, but also as a conduit for heat to conduct to the cantilever. The process of attaching a nanowire to a cantilever consists of using a set of piezoelectric nanomanipulators with tungsten probe tips (Kleindiek) in a dual column focus ion beam (FIB) system (JEOL JIB-4500). In this instrument, the manipulators sit on a separate platform from the sample holder. This process was conducted in the Integrated Sciences Cleanroom and Nanofabrication Facility at Boston College.

The attachment process is based on previous manipulation and attachment of nanowires using similar manipulators.[65] Since we are interested in the optical properties of these nanowires, a particular effort was made to ensure the purity of the nanowires was retained in the attachment process. Specifically, ion implantation from the gallium ion source and possible contamination via metal deposition are common sources of impurities that may affect this

measurement. Therefore, to avoid both, an ultra high vacuum adhesive known as SemGlu (Kleindiek) was used to attach the nanowire to the cantilever. This particular adhesive is curable when exposed to a high intensity electron beam; hence, the ion beam was not needed. The acceleration voltage of the e-beam used was 5 kV.

For sample preparation, the wafer containing the nanowires was broken into smaller pieces and placed on the sample holder for the FIB. By using smaller samples, more nanowires were exposed at the edges of the samples, allowing for a greater pool of wires to choose from. In addition, a small sample of the SemGlu is placed on the sample holder. And finally, a bimorph cantilever (NanoWorld) attached to a small copper holder via silver epoxy is placed such that the gold side is exposed to the e-beam. This was to ensure an electrically conducting surface was exposed to the e-beam; otherwise, charge accumulation on the silicon nitride and the holder chip would induce bending in the cantilever. Note that the silver epoxy was baked at 80 °C for at least four hours to remove any remaining solvents in the epoxy. Alternatively, the nanowires were sonicated in a solution of ethanol and deposited onto a glass substrate. However, this method showed a tendency to fracture the wires as well as release a large amount of silicon particulates from the porous regions thus contaminating the wires.

The following will be a step-by-step description of the process used to attach a nanowire to the cantilever. All steps will be referred to Fig. 3.4,
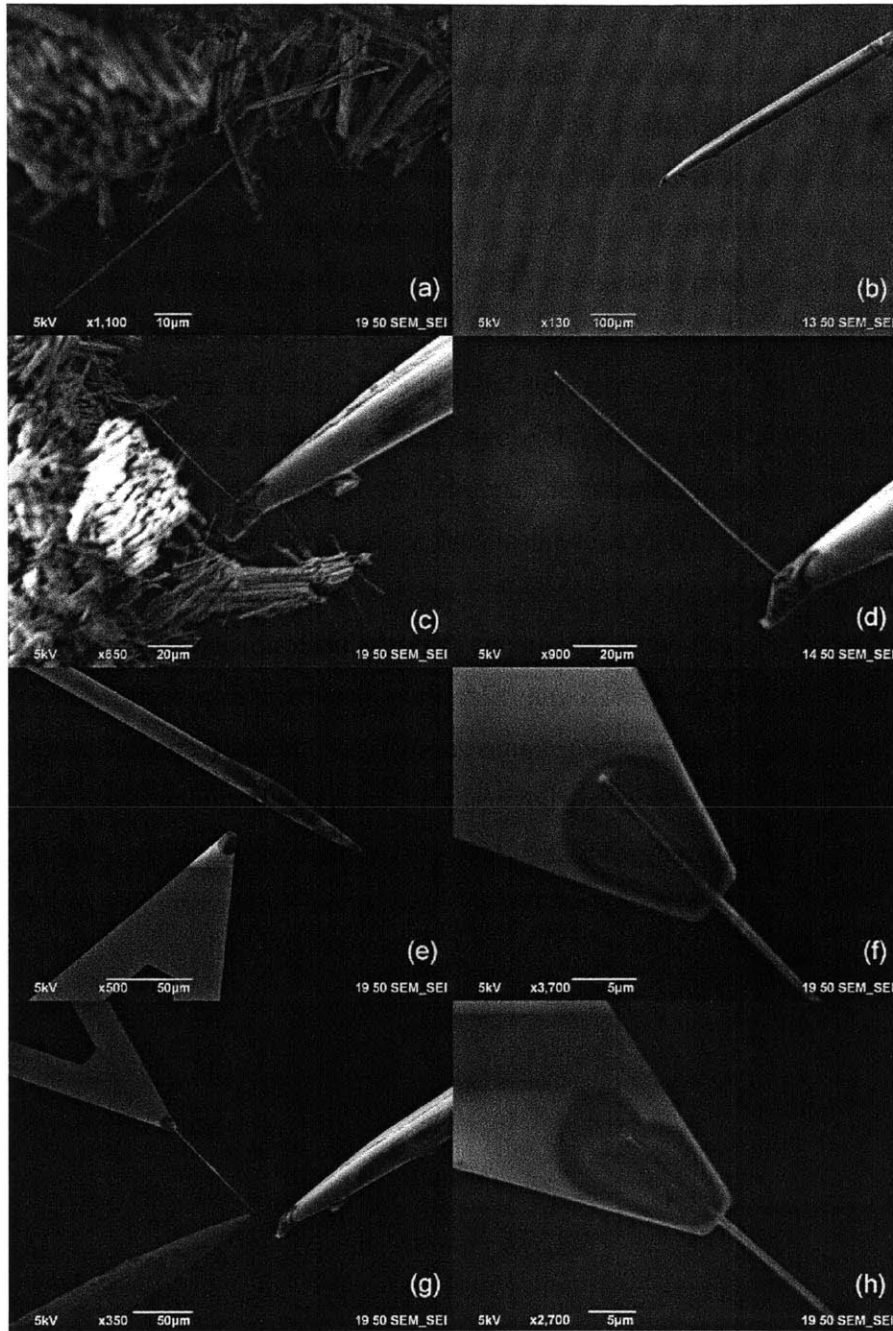
Figure 3.4: Nanowire attachment process: (a) A sufficiently long and uniform silicon nanowire at the edge of a wafer. (b) A probe tip is then coated in SemGlu by dipping the manipulator into the droplet of glue on the sample holder. (c) The probe tip is brought into contact with the nanowire such that the tip of the nanowire is immersed in the glue. The glue is then cured by enlarging the beam spot size and increasing magnification. (d) The result after breaking the nanowire free from

the wafer. (e) The cantilever is then coated with glue to attach the free end of the nanowire. (f) The nanowire is then carefully lowered until contact is made with the cantilever. The glue is once again cured. (g) To break the nanowire free, a second probe tip is used to shear the nanowire from the first probe tip. (h) An additional layer of glue is applied on top of the nanowire to ensure the nanowire is fully anchored to the cantilever.

To begin, the first step is to choose a nanowire to extract from the wafer sample. The choice is dictated by the uniformity, length and diameter of the wire. It was often observed that many wires exhibited additional wires or blocks of porous silicon attached either at its base or along its length. Thus, careful attention must be paid when assessing the uniformity of a particular nanowire. Generally, longer nanowires (~100 μm) are preferable to minimize end effects and to maximize the absorbed power to ensure a sufficiently high signal-to-noise-ratio during measurement. Ideally, the diameter of the wire should be chosen according to the range prescribed in Section 2.2 where enhancement in the absorption efficiency is theoretically observed. However, the sensitivity of the platform used in this study was limited. Therefore, to validate the operating principle of this technique, a larger diameter wire was chosen, as shown in Fig. 3.4a.

Once a nanowire is chosen, the tip of the manipulator is coated with SemGlu by repeatedly dipping the manipulator into the droplet of glue until enough is collected to immerse the nanowire. It should be noted that an excess amount of glue will not provide a stable support for the nanowire as the glue may be too thick to be sufficiently cured by the e-beam. This will cause problems when attempting to pull the nanowire from the wafer. An example of a probe tip coated in glue is shown in Fig. 3.4b.

Next, the probe tip is carefully positioned below the end of the nanowire and slowly raised until contact is made. In this manner, the immersed end of the nanowire can still be seen by the e-beam. This contact may occur suddenly due to charge accumulation between the nanowire and the probe tip. If the nanowire is not securely attached to the wafer, this effect will be even more pronounced. Once contact is made, the glue is cured by increasing both the magnification of the e-beam and the beam spot size. Curing typically takes 5-10 minutes. This is shown in Fig. 3.4c.

Once the glue is cured, the nanowire is ready to be separated from the sample wafer. The difficulty in breaking the nanowire from the wafer will vary depending on how strongly affixed the nanowire is to the wafer. Generally, larger wires tend to be more difficult to separate by virtue of their larger cross section. Therefore, the wire is generally pulled at an angle to induce some shearing at its base. In some cases, use of an additional manipulator to more controllably break the nanowire at its base may be needed. The separated nanowire is shown in Fig. 3.4d.

Now that the wire has been acquired, the next step is to use another manipulator to coat the cantilever with SemGlu. In this case, a large amount of glue should be collected onto the manipulator so that when the probe tip is in contact with the cantilever, a large drop of glue is deposited. The goal here is to deposit enough glue so that the nanowire is once again fully immersed onto the end of the cantilever. An example of a probe tip coated more heavily with glue and the resulting deposit of glue on the cantilever is shown in Fig. 3.4e. However, ascertaining whether enough glue has been placed is generally quite difficult given the opacity of the glue when viewed under an e-beam. Generally, if variations in the contour of the glue can be seen, as shown in Fig. 3.4e, this is an indication that enough glue was placed.

The next step is to attach the nanowire to the cantilever. First, the cantilever is rotated until its length is parallel with the nanowire. Then, the manipulator holding the nanowire is slowly lowered until the free end of the nanowire comes into contact with the glue on the cantilever. Charge accumulation may deflect the nanowire away from the cantilever. However, with sufficient patience, the nanowire can be placed directly on the center of the glue. Contact may not be obvious without a high quality screen capture. In most cases, the nanowire will only be partially immersed. However, if the glue surrounds the nanowire on both sides, this is generally sufficient to hold the nanowire in place once it is broken free from the probe tip. Since this attachment can be quite fragile, curing is done for at least 10 minutes to ensure the glue is fully cured. The result is shown in Fig. 3.4f.

To free the nanowire from the probe tip, a second probe tip is used to shear the nanowire at the point where the nanowire was originally glued to the first probe tip. This is done by dragging the second manipulator across the first manipulator, catching the nanowire along the way. Generally, this must be done several times until the nanowire is separated. The result is shown in Fig. 3.4g.

At this point, additional glue is placed on top to ensure the nanowire is sufficiently anchored to the cantilever, as shown in Fig. 3.4h. Once the glue is cured, the nanowire is now fully attached to the cantilever. Figure 3.5 shows a scanning electron microscope (SEM) image of the final result.

5kV   x160   100μm   19 50 SEM_SEI
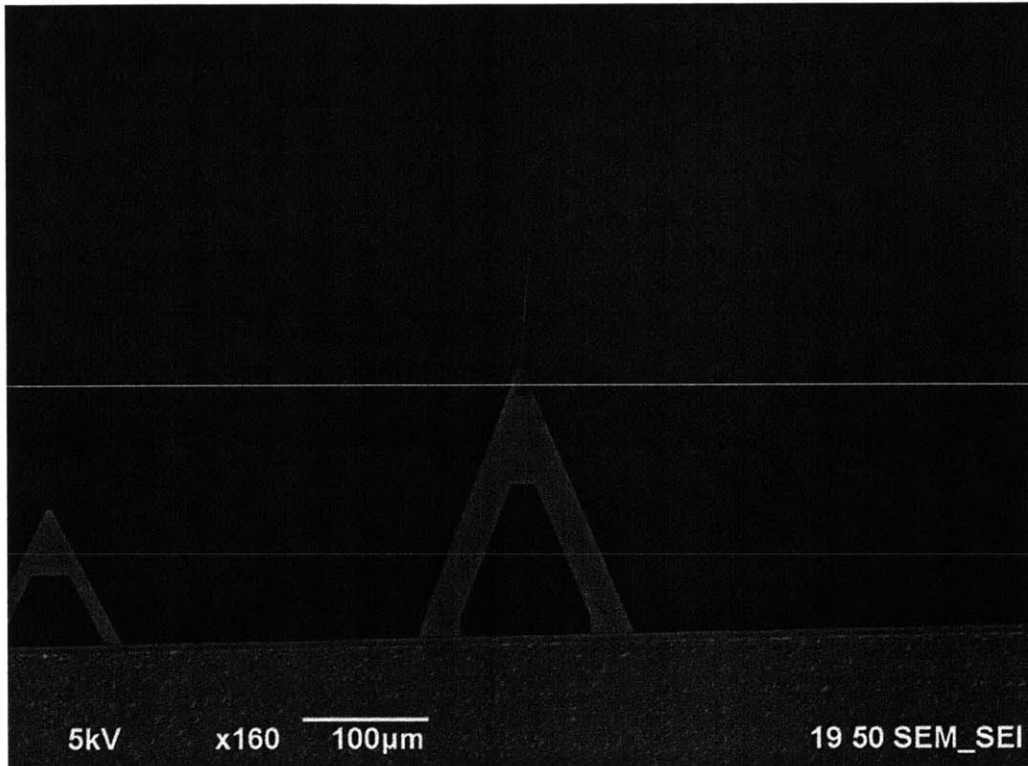
Figure 3.5: A scanning electron microscope (SEM) image of a silicon nanowire attached to an AFM bimorph cantilever.

3.4 AFM Thermometry Technique

3.4.1 Overview

Now that we have the cantilever/nanowire sample, the next step is to measure its absorption efficiency. To reiterate, AFM thermometry makes use of an AFM cantilever as a heat flux and temperature sensor. In this work, we make use of the cantilever as a photothermal detector, as originally proposed by Barnes *et al.*,[27, 28] to directly and quantitatively measure the absorption efficiency of a silicon nanowire. This is achieved by measuring the heat absorbed by

the nanowire when illuminated with monochromatic light. From (2.87), we can deduce that the absorption efficiency can be written as a ratio of the absorbed and geometric incident power,

$$Q_{abs} = \frac{P_{abs}}{P_{inc}}$$

(3.11)

where, Q_{abs} is the absorption efficiency, P_{abs} is the total power absorbed by the wire and P_{inc} is the geometric incident power. From (3.11), the absorbed power can be defined in this experiment to be,

$$P_{abs} = \frac{X(\lambda)}{\beta S_p}$$

(3.12)

where X is the measure cantilever deflection response as a function of the wavelength of light, β is a correction factor that accounts for the frequency response of the cantilever and S_p is the power sensitivity obtained from the power calibration. The geometric incident power in (3.11) is determined by,

$$P_{inc} = P_{tot}(\lambda) \cdot f$$

(3.13)

where P_{tot} is the total power from the optical fiber at a particular wavelength and f is the fraction of the beam incident on the nanowire which includes the Gaussian beam profile of the optical fiber. Therefore, to determine the absorption efficiency, Q_{abs}, we must measure the parameters in (3.12) and (3.13). The remainder of this subchapter is therefore devoted to the measurement of these parameters.

First, the experimental setup used in this study will be presented in Sec. 3.4.2. This includes a discussion on the various components and equipment used in Sec. 3.4.2.1, the methodology applied to optically align the various components to the cantilever and the nanowire in Sec. 3.4.2.2, a discussion on the implementation of frequency modulation in Sec. 3.4.2.3, and the calibration of the light source in Sec. 3.4.2.4.

This will be followed by the methods used to measure the parameters defined in (3.12) and (3.13) in Sec. 3.4.3. To measure the absorbed power, P_{abs}, in (3.12), we measure the bending response of the cantilever. When the nanowire absorbs light, the energy will conduct across the nanowire and the cantilever as heat. The small change in temperature that arises in the cantilever will cause a thermomechanical bending response. The measurement of this response will be discussed in Sec. 3.4.3.1. To correlate the bending response to an absorbed power, a power

78

calibration must be conducted. This calibration is based on varying the power of the detector laser, a known heat input, and measuring the resulting bending response. This calibration will be discussed in Sec. 3.4.3.2. In addition, since the light input in this experiment is modulated, the magnitude of the thermomechanical bending response from the cantilever will depend on the frequency of modulation. Generally, higher frequencies lead to a smaller response. As a result, a correction factor must be measured to account for this attenuation. This will be discussed in Sec. 3.4.3.3.

To measure the geometric incident power, P_{inc}, in (3.13), we must measure the total output power from the optical fiber at each wavelength. Then, the area fraction of the beam incident on the nanowire must be determined. Because the beam profile is Gaussian, a simple ratio of the nanowire cross section and the beam spot will not suffice. The method used to determine this fraction will be discussed in Sec. 3.4.3.4.

3.4.2 Experimental Setup

3.4.2.1 Component Assembly

The experimental setup used in this study mirrors closely with the original setup created by Barnes et al. [28] Figure 3.6 provides an overview of the essential components used in this setup,
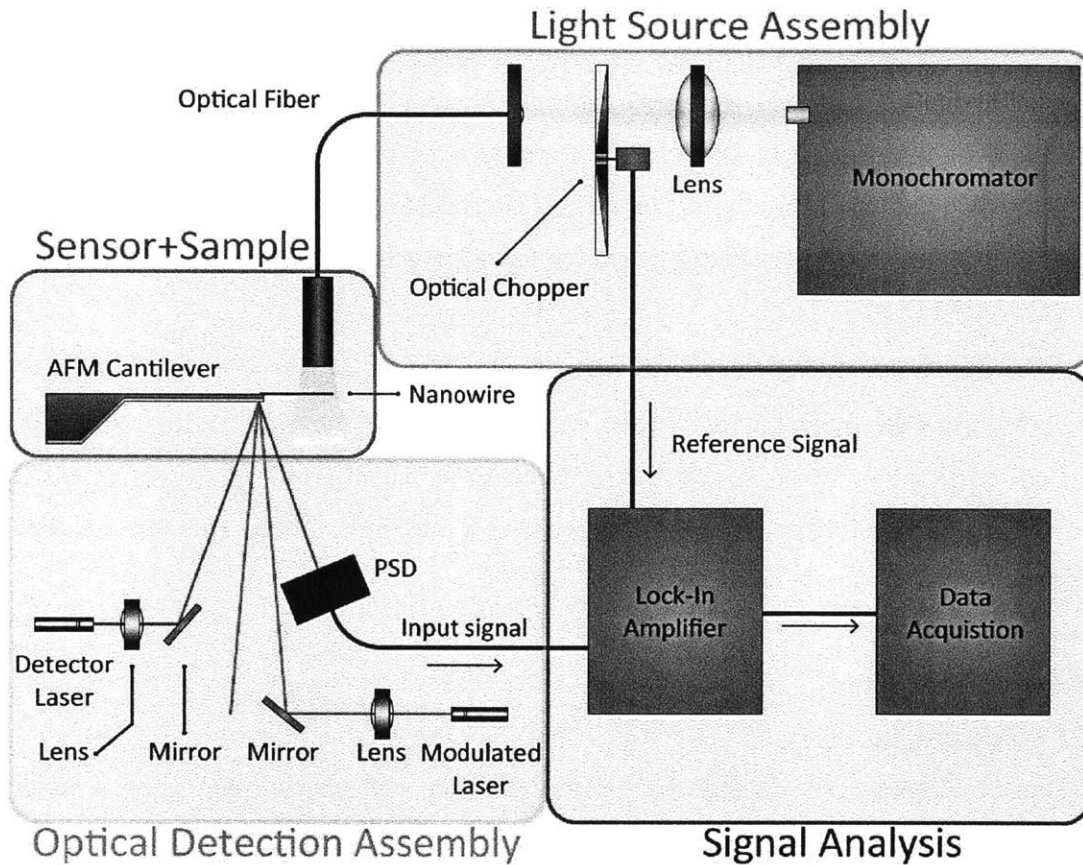
Figure 3.6: A schematic diagram of the experimental setup used in this study to measure the spectral absorptance of an individual Si nanowire. The setup itself can be broken into four assemblies. The Sensor+Sample Assembly consists of the cantilever and the nanowire attached. The Optical Detection Assembly consists of all the components used to measure the bending response of the cantilever and the frequency response correction factor. This includes a CW laser, TTL modulated laser and their respective optics. A position sensitive detector (PSD) is used to track the bending response of the cantilever. The Sensor+Sample Assembly and the Optical Detection Assembly are placed in a vacuum chamber. The Light Source Assembly consists of all the components used to control the input light source. This includes a monochromator (and its associated light source), an optical fiber, an optical fiber coupler, the optics to focus the output light from the monochromator and an optical chopper for modulation. And finally, the Signal Analysis assembly consists of the equipment used for signal analysis and acquisition. This includes an amplifier for the PSD, a lock-in amplifier, several multimeters to measure data and a computer for data acquisition.

As shown in Fig. 3.6, the setup can be grouped into four assemblies of components according to their function in the experiment. The Sensor+Sample Assembly and the Optical Detection Assembly are mounted onto an optical breadboard and placed into a vacuum chamber (Kurt J. Lesker Company, BX2424S) supported by rubber dampers and springs to minimize vibration. Vacuum is used to eliminate convection losses. The Sensor+Sample Assembly corresponds to the cantilever and nanowire sample. In order to mount the sample in the experimental setup, the small copper plate supporting the cantilever is glued onto a larger copper plate using silver epoxy. This is then mounted onto an optical breadboard such that the cantilever is horizontal and on its side. Since the copper plates and the epoxy are thermally and electrically conducting, they function as both a heat reservoir and an electrical grounding path during the experiment. Grounding is achieved through the optical mounts and the optical breadboard, which are filed down to ensure the underlying metal is exposed. A wire is then connected from the breadboard to the vacuum chamber wall.

The Optical Detection Assembly corresponds to components used to measure the bending response of the cantilever and the frequency response correction factor. To measure the bending response, a CW diode laser (Lasermate Group, LTG6354AH) is focused and aligned onto the cantilever via a mirror. An iris is placed immediately after the mirror to remove a surrounding halo present in the laser beam. The laser is then reflected onto a two dimensional position sensitive detector (PSD) (Ontrak Photonics, 2L4SP) which will measure the change in bending from the cantilever by virtue of a shift in the beam spot on the detector. Since the cantilever is typically mounted horizontally, only one axis needs to be measured during the experiment. To measure the frequency correction factor, a TTL modulated diode laser (Lasermate Group, LTC6702A5-T) is used. This laser can be operated in both continuous wave (CW) and modulated modes. As before, this laser is focused and aligned via a mirror onto the cantilever. However, due to size constraints on the breadboard, this optical path is positioned in a plane above the cantilever. As a result, the modulated laser is aligned in a plane perpendicular to the detector laser. This can be observed in Fig. 3.7a. Both lasers are powered by sourcemeters (Keithley, 2425/2430). The frequency of the TTL modulated laser is controlled with a function generator (HP, 8111A) whose input is verified using an oscilloscope (Tektronix, TDS520A).

The Light Source Assembly corresponds to the components controlling the light input incident on the nanowire. A xenon lamp source connected to a monochromator (SpectraMaster)

is used in this study. This provides light in the visible wavelength range. Since the output light is diverging, a lens is used to focus the light onto an optical fiber coupler. The light is then coupled to the optical fiber (Thorlabs, BFL48-200-custom) as shown in Fig. 3.7b. This optical fiber is then routed through an optical feedthrough into the vacuum chamber where an exposed end is mounted onto the optical breadboard, as seen in Fig. 3.7a. Since this experiment requires frequency modulation, an optical chopper, and its associated frequency modulator, (Scitec Instruments, 300) is mounted before the optical coupler.

The Signal Analysis Assembly refers to the equipment used for signal analysis and data acquisition. This consists of a position sensing amplifier (Ontrak Photonics, OT-301), a lock-in amplifier (Stanford Research Systems, SR850), a pair of multimeters (HP, 34401A and Keithley, 182) and a computer for data acquisition. Furthermore, a powermeter (Newport, 1918C/818-UV) is used in the experimental preparation, power calibration and the measurement of the geometric incident power, as will be discussed in Secs. 3.4.2.2, 3.4.3.2 and 3.4.3.4, respectively.
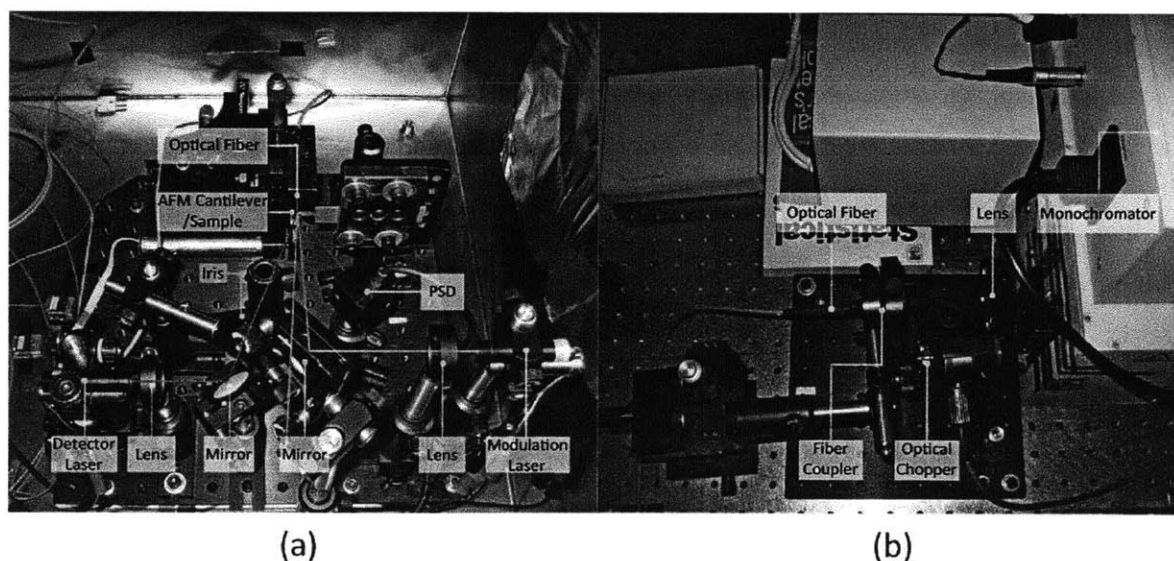
Figure 3.7: The actual assemblies used in this study. (a) An image of the Sensor+Sample Assembly and the Optical Detection Assembly as viewed in the vacuum chamber. The red and orange lines show the optical paths for the detector laser and modulation laser, respectively. (b) An image of the Light Source Assembly.

3.4.2.2 Experiment Preparation

For the experimental setup presented in Sec. 3.4.2.1, the input light source, the detector laser and the modulated laser must all be manually aligned. In all cases, an optical scope is used to view the cantilever and the optical fiber. First, the coupling efficiency of the Light Source Assembly is optimized by moving the fiber coupler using a 3-axis positioning system and measuring the output power using a powermeter. Once the power is maximized, no further changes need to be made in this part of the setup. Note that the orientation of the optical fiber, particularly with respect to the light source, is not crucial in this experiment as the light from the optical fiber is unpolarized. This will be verified in Ch. 4, Sec. 4.1.3.

The angular orientation of the input light source, i.e. the optical fiber, is fixed in this setup where the fiber axis is aligned with the y-axis as defined in Fig. 3.8. Therefore, to align the optical fiber to the nanowire, the cantilever must be positioned such that the nanowire will be illuminated at normal incidence, i.e. it must align with the x-axis. It should be noted here that light from the optical fiber will diverge within a narrow exit cone. Therefore, alignment is taken with respect to the angular component parallel with the fiber axis. The cantilever is securely clamped and positioned using an optical mount. Figure 3.8 is a top down view of the cantilever when placed into the experimental setup,
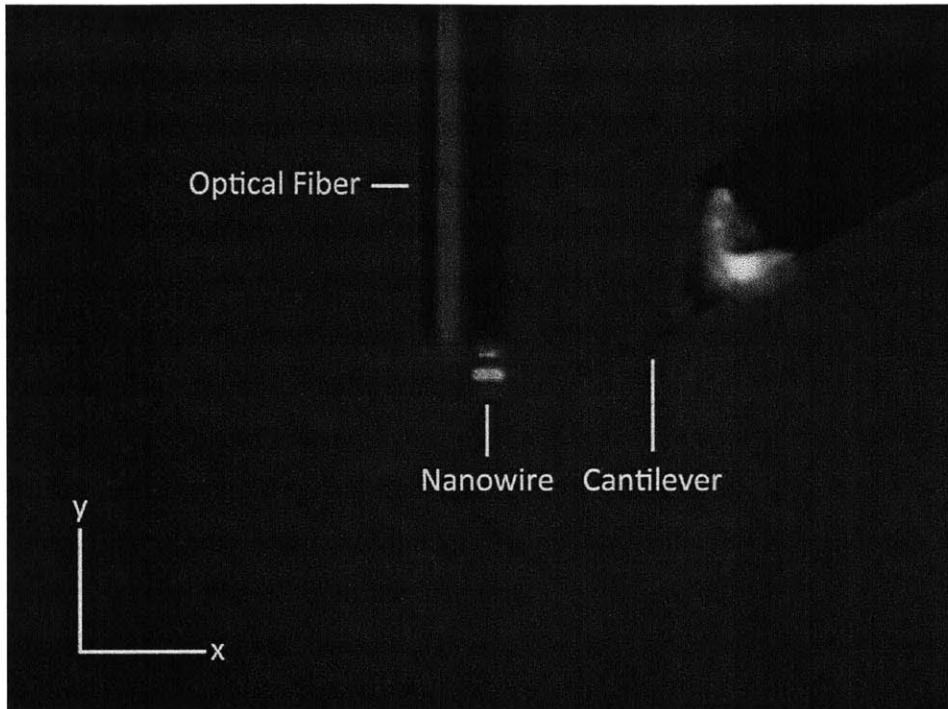
Figure 3.8: An image of the optical fiber aligned to the nanowire attached to the cantilever taken from a top-down view. Here, the optical fiber is retracted by ~100 μm to more easily view the nanowire. The nanowire can clearly be seen because of its strong scattering properties. Note that this image is of a different cantilever/sample.

Generally, the scattering efficiency of silicon nanowires with a diameter of 100–1000 nm is quite high in the visible wavelength spectrum. As a result, in Fig. 3.8, the nanowire attached to the cantilever can clearly be seen when illuminated by the optical fiber. Note that this image is a different cantilever/sample from before and is used merely as an example of what is typically observed during alignment. Since this alignment is done by eye using an optical scope with limited magnification, an inherent uncertainty arises. Fortunately, the absorption efficiency is insensitive to small variations in the angle of incidence, as will be shown in Ch. 4, Sec. 4.1.4.

Once the angular orientation of the cantilever/nanowire is close to normal incidence, the next step is to position the optical fiber via a 3–axis positioning system to illuminate a portion of the nanowire. This system consists of two manual micrometer stages for the y, z-axes and a motorized encoder mike (Oriel, 18008) for the x-axis. The goal is to illuminate 50% of the nanowire to ensure no stray light from the optical fiber will see the cantilever; otherwise, the

measured absorption efficiency will be a combination of the nanowire and the cantilever. This value was chosen for experimental ease. First, the optical fiber is positioned approximately 50 μm from the nanowire along the y-axis. This distance is chosen to be small enough to avoid problems with stray light and far enough to avoid possible force interactions between the optical fiber and nanowire/cantilever which may arise due to charging. Once again, the use of an optical scope will generally lead to an uncertainty when assessing the beam spot size due to the divergence of the beam. However, it will be later shown in Ch.4, Sec. 4.1.4 that at such a small separation distance, the divergence is negligibly small. Thus the beam spot size is effectively constant over a range of several tens of microns.

The next step is to position the optical fiber along the z-axis. Ideally, the optical fiber should be positioned so that the tip of the nanowire is centered to the optical fiber. However, the optical fiber in this experiment was manually cleaved. In order to avoid the cleave initiation point, the optical fiber was offset by 10-15 μm. Since the light from the optical fiber follows a Gaussian beam profile, uncertainty in the alignment along the z-axis could lead to more error in the final result. For a 5 μm uncertainty, this will correspond to a variation of 10% in the absorption efficiency from the area fraction parameter. This will be further discussed in Sec. 3.4.3.4.

The last step is to align the optical fiber along the x-axis. Again, uncertainty in this alignment will lead to error in the absorption efficiency. However, the area fraction parameter was found to be very sensitive to variations along the radial direction. As a result, the position of the nanowire must be known very precisely in order to avoid substantial error. Therefore, a motor mike is used to control the alignment along this axis. Although this motor includes a controller which outputs position, it was deemed to be unreliable. Instead, the optical fiber was positioned such that 50% of the nanowire was illuminated. This value was chosen as it can be verified visually with relative ease based on the light scattered by the nanowire when illuminated. The optical fiber was initially positioned such that the tip of the nanowire was at the center of the optical fiber along the x-axis. From here, the optical fiber was very slowly moved until 50% illumination was achieved.

As one can clearly see, despite efforts to improve the accuracy of aligning the optical fiber to the nanowire, a great deal of uncertainty still remains. It should be noted that alignment of the angle of incidence and the y-axis is done outside the vacuum chamber due to space

limitations. However, no obvious variation in these alignments was observed upon transferring the setup to the chamber. In addition, when the system is pumped down to vacuum, convective losses are eliminated. The temperature of the cantilever will thus change which will result in a bending response. Generally, this change is quite small (<< 1°) therefore it is not expected that this will cause significant changes in the alignment. However, these factors nonetheless add uncertainty and if nothing else provide evidence that it would be worthwhile to pursue a better method of alignment in the future.

Once the setup is situated in the vacuum chamber, the detector laser and modulated laser must be aligned to the cantilever. The detector laser emits an elliptical beam. The orientation of the laser is thus chosen in order to maximize the area illuminating the cantilever. Since the laser is partially polarized, the orientation used corresponds to a TM wave. In addition, a halo around the beam is typically observed from these lasers. As this could cause errors during the power calibration, an iris is placed immediately after the mirror to partially remove this halo. Further corrective effort is made as will be discussed in Sec. 3.4.3.2. Generally, it is preferable to choose the incident angle of the laser to be as small as possible to reduce the size of the beam spot. However, in this setup, it is imperative that stray light from the optical fiber does not hit the PSD. This will cause an error as the measured response will include both the light source and the cantilever. Based on the numerical aperture of the optical fiber, the half angle of the exit cone was found to be ~14 degrees. Therefore, a 20 degree angle of incidence was chosen to avoid this problem.

The laser was then focused and aligned to the cantilever by maximizing the sum signal, which is a measure of the total incident power on the PSD. The resulting diffraction pattern that arises due to the large beam spot size (30x50 μm) can also be used to visually verify the signal is indeed maximized. To compensate for the cantilever bending during pumpdown, the PSD is shifted until the beam is at the edge of the detector. The difference signals are used to position the beam on the PSD. As mentioned before, the sensitivity of this system can be amplified by increasing the separation distance between the cantilever and the PSD. However, this is limited by the diverging beam spot reflected by the cantilever. In this experiment, the PSD is typically placed ~7 cm from the cantilever. Fig. 3.9 is an image of the setup taken at an angle to show the position of the laser spot on the cantilever. Again, this is an image of a different cantilever/sample as before,
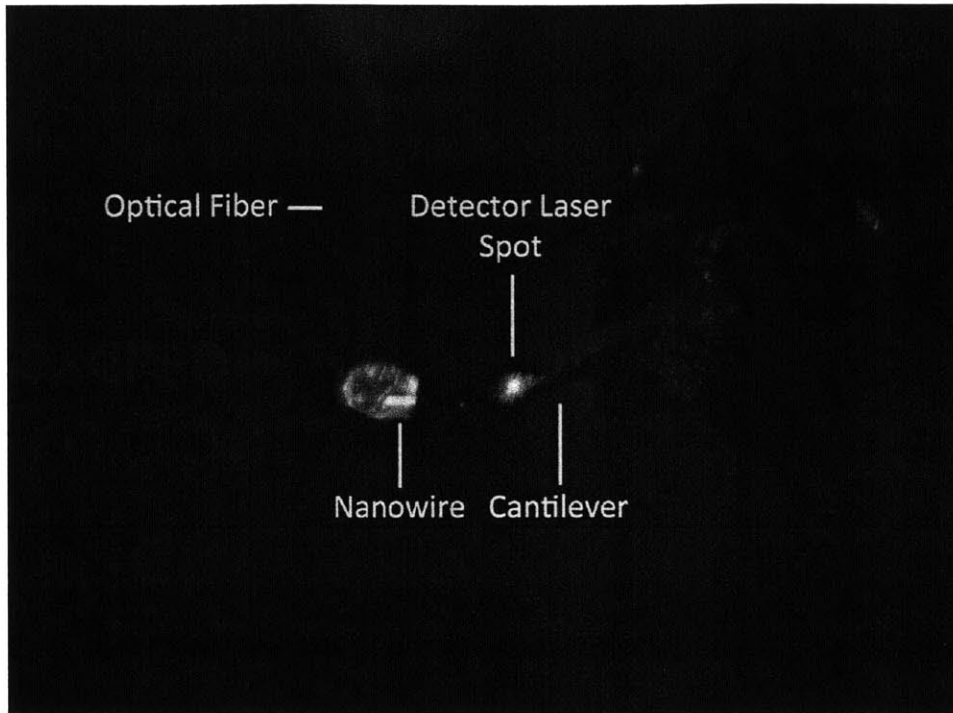
Figure 3.9: An image of the cantilever under illumination by the detector laser. The beam spot, as shown, is concentrated near the tip of the cantilever. Once again, this image is of a different cantilever/sample (see Fig. 3.8).

Finally, all that remains is aligning the modulated laser to the cantilever. In this case, the laser emits a circular beam profile. Again, the laser is focused and aligned as before. Since the frequency correction factor is measured in vacuum, the need to precisely align and focus the laser is not as stringent as the detector laser so long as the heating input is consistent throughout the entire calibration. As discussed previously, size constraints in the setup necessitated raising the laser to a plane above the cantilever. As a result, the laser is reflected by the mirror in the y–z plane. The angle of incidence is again chosen to be approximately 20 degrees. To verify the laser is focused and aligned, the laser was tested in both CW and modulated modes. If a response can be clearly observed by the cantilever via the detector laser and PSD, the modulated laser is properly aligned.

Upon completing all alignment procedures, all wires are taped down securely to the vacuum chamber to ensure no connectivity issues in vacuum and to minimize vibration noise

from loose wires. The next step is to then pump down the vacuum chamber for several hours. Once the pressure reaches ~10^5 Torr, the experiment can proceed.

3.4.2.3 Frequency Modulation and Sensitivity

In order for the cantilever to reach its maximum power sensitivity, a lock-in amplifier is used to significantly improve the signal-to-noise ratio. However, by using a lock-in amplifier, the input light source must be modulated. This is achieved using an optical chopper and its associated controller. The choice of the modulation frequency is dictated by several factors including the temporal response of the cantilever and the nanowire as well as the frequency distribution of system noise.

If we consider only the cantilever for a moment, a periodic heat input will cause the cantilever to oscillate with a certain amplitude. As the frequency of this input increases, the amplitude will decrease. This is due to the thermal response time of the cantilever where the sensor simply cannot respond quickly enough to changes in the heat input. The attenuation of the bending response due to this modulated input is what we refer to as the frequency response of the cantilever.

The modulation frequency should ideally be as low as possible. However, at lower frequencies, noise due to electrical sources, vibration, thermal drift, etc. will be more prevalent. Therefore an optimal modulation frequency range must exist. To help determine this frequency range, the thermal time constant can be estimated based on the Fourier number,[28, 66]

$$\tau \approx \frac{l^2}{2} \left(\frac{\rho_1 C_1 t_1 + \rho_2 C_2 t_2}{k_1 t_1 + k_2 t_2} \right) \tag{3.14}$$

where ρ is the density, C is the heat capacity and k is the thermal conductivity. The time constant defined in (3.14) is simply an expansion of the effective thermal diffusivity of the cantilever and represents the minimum time required for heat to diffuse across its length. The factor of 2 is a crude correction to account for the temperature variation along the length of the cantilever under a tip heating condition.[28] For the purposes of estimating the thermal time constant, we may use bulk material properties for the two layers of the cantilever. Layer 1 refers to the gold film with the following properties: $\rho_1 = 19{,}300 \; kg \cdot m^{-3}$, $C_1 = 129 \; J \cdot kg^{-1} \cdot K^{-1}$ and $k_1 = 296 \; W \cdot m^{-1} \cdot K^{-1}$. Layer 2 refers to the silicon nitride substrate with the following

88

properties: $\rho_2 = 2400\ kg \cdot m^{-3}$, $C_2 = 691\ J \cdot kg^{-1} \cdot K^{-1}$ and $k_2 = 32\ W \cdot m^{-1} \cdot K^{-1}$.[29] Using the dimensions of the cantilever mentioned previously in Sec. 3.1, the thermal time constant of the cantilever is found to be $\tau \approx 0.6\ ms$. Previous studies have experimentally measured a time constant of $\tau \approx 0.2 - 0.3\ ms$ using similar cantilevers.[28-30] The cantilever can be modeled as a first order system, therefore the cut-off frequency can be estimated to be $f = 1 / 2\pi\tau \approx 265 - 795 Hz$.

Since the attached nanowire will be used to conduct heat to the cantilever, the thermal time constant of the nanowire must be considered as well to determine the modulation frequency. The length of the nanowire is typically on the order of $l \approx 100\ \mu m$. Hochbaum et al. showed the thermal conductivity of rough silicon nanowires will be at a minimum $k \sim 10\ W \cdot m^{-1} \cdot K^{-1}$ for nanowires with a diameter of $D \sim 150\ nm$.[61] This value is a conservative estimate since a larger diameter, as is the case in this study, will result in a higher thermal conductivity. Assuming the density and the heat capacity are similar to bulk values, the thermal diffusivity to be on the order of $\alpha \sim 10^{-5}\ m^2 \cdot s^{-1}$. Therefore, the time constant will be $\tau \approx 1\ ms$ and the cut-off frequency is $f \approx 160\ Hz$.

Based on these estimations, we can conclude that the nanowire will be the dominating factor in the thermal response of the system. This value is therefore an upper bound in the frequency range. The lower bound is dictated by noise in the system. Below 100 Hz, vibration, thermal drift and electrical noise are the primary sources of noise in this system. In particular, power line noise (60 Hz) and its higher harmonics should be avoided. Therefore, the modulation frequency is chosen to be 140 Hz.

The power resolution of a bimorph cantilever for thermal measurements is fundamentally limited by the thermal noise present in the experiment.[28, 29] The thermal noise can be formulated as,

$$\sqrt{\langle z_{th}^2 \rangle} = \sqrt{\frac{4k_bTB}{k\omega_0 Q}} \tag{3.15}$$

where z_{th} is the thermal noise measured in $\text{Å}/\sqrt{Hz}$, k_b is the Boltzmann constant, T is the temperature, B is the measurement bandwidth, k is the spring constant, ω_0 is the resonant frequency and Q is the quality factor of the resonance.

Assuming thermal noise is the dominant source of noise at 140 Hz, the power sensitivity of the cantilever can be maximized by using the lock-in amplifier to minimize the measurement bandwidth. However, since a low pass filter controls the measurement bandwidth, an extremely narrow bandwidth has the effect of increasing the response time of the system. As a result, a measurement bandwidth of 2.7 mHz, corresponding to a time constant of 30 s, is chosen which is similar to previous studies.[28-30]

The spring constant and resonant frequency in (3.15) is determined by the cantilever used. Custom cantilevers can be designed to improve the power resolution further. This will be a subject of future studies. The quality factor and temperature of the system meanwhile cannot be significantly changed without implementing substantial modifications to the measurement platform.

3.4.2.4 Monochromator Calibration

The monochromator was modified by adding slits to the input and output in order to improve the wavelength resolution despite the penalty of an overall decrease in the throughput of the system. Originally, the range of the output spectrum from the monochromator was limited by the motor controlling the rotation of the diffraction grating. Therefore, the grating was manually rotated in order to shift the output spectrum to include the near infrared. As a result of these changes, the monochromator had to be recalibrated using a spectrometer (Ocean Optics, USB4000). The spectrometer uses an optical fiber as its input. This optical fiber was simply switched with the optical fiber used for the experiment. A filter was also placed along the optical path to prevent saturation of the spectrometer.

The calibration was done with respect to the numerical controls on the monochromator. Due to the finite range of the spectrometer, the calibration was conducted from 420 to 950 nm using 10 nm increments. The centerline peak in the output was used to determine the true wavelength. The full width half maximum was also measured to be 7–8 nm. Due to this finite bandwidth, the theoretical solution used to compare with the experimental results will require wavelength averaging based on this calibration, as will be discussed in Ch. 4, Sec. 4.1.2.

3.4.3 Measurement and Calibration

3.4.3.1 Absorption Measurement, X

To measure the absorption efficiency of a silicon nanowire, the cantilever bending response, X, is measured at each wavelength of the input light source. Prior to measurement, the monochromator was allowed to first thermalize for 1 hour to minimize variations in the wavelength of the light output. Although the monochromator was calibrated for a broad range, enhancement in the absorption efficiency for silicon nanowires is theoretically expected to occur within the visible wavelength spectrum. Therefore, the absorption measurement was conducted from 420 to 600 nm in 10 nm increments.

The use of a lock-in amplifier in this measurement enables control over the measurement bandwidth and by extension, the signal-to-noise ratio. As mentioned previously, the choice of a 2.6 mHz bandwidth corresponds to a time constant of 30 s. Consequently, the response of the system to changes in the light input ideally required several minutes to stabilize. However, the presence of noise near the modulation frequency manifested itself as low frequency fluctuations in the signal output. In order to obtain an accurate measurement of the bending response amplitude, more data was needed to properly average these fluctuations. Therefore, the total measurement time typically lasted several hours. Fortunately, thermal drift in the signal, which is an issue for steady state measurements, can be eliminated using the lock-in amplifier. Measurements are conducted several times where each measurement has its own corresponding calibration in vacuum.

3.4.3.2 Power Calibration, S_p

In order to extract quantitative data from the cantilever deflection response, a power calibration must be conducted. This calibration correlates the measured bending response from the PSD to a known heat input. From this correlation, we can determine the absorbed power by the nanowire for all measured wavelengths. Previously, Shen *et al.* established a procedure from which the effective thermal conductance of a cantilever can be measured directly by using a temperature and power calibration.[32] Here, we use a slightly modified process to conduct the power calibration. In essence, the idea is to vary the detector laser power and measure the resulting bending response. Then, a powermeter is used to measure the power absorbed by the cantilever for each laser power increment.

The power calibration was typically conducted in vacuum following the absorption measurement to ensure experimental conditions are similar. It is important to emphasize here that the detector laser is the only heating source in this calibration. And unlike the absorption measurement, the data was taken directly from the PSD rather than the lock-in amplifier as the deflection response was much larger. Thus, this calibration was conducted under steady state conditions. To change the laser power, the input voltage was varied from its turn-on voltage (3.8 V) to the saturation voltage (5 V). The difference and sum signals were then measured at each voltage increment.

Ideally, the absorbed power should be measured simultaneously. However, due to limitations in the platform, the absorbed power was measured under ambient conditions following the completion of all measurements in vacuum. The presence of convective losses will change the behavior of the cantilever. As a result, experiments in vacuum and ambient conditions had to be treated as separate experiments. To bridge these measurements, the sum signal can be used.

Generally, changing the laser power will lead to a corresponding change in the sum signal measured by the PSD. The difference signal can therefore be measured as a function of the sum signal in vacuum. In ambient conditions, the sum signal can be measured as a function of the absorbed power. Although there will still be a bending response, it is typically much weaker. Thus any variation can be assumed to have minimal effect on this measurement. The product of these two parameters will result in the power sensitivity,

$$S_p = \frac{X}{P_{abs}} = \frac{X}{Sum(V)} \cdot \frac{Sum(V)}{P_{abs}} \tag{3.16}$$

Cancelling the dependency on the sum signal in (3.16) is valid so long as the beam spot does not change in size or shape between vacuum and air. In addition, the beam must be fully captured by the PSD in both cases. Each term was measured several times and averaged.

In (3.16), the absorbed power, P_{abs}, was measured indirectly from the incoming, reflected and bypassed power using a powermeter and a photodiode. Figure 3.10 shows the schematic of these contributions,
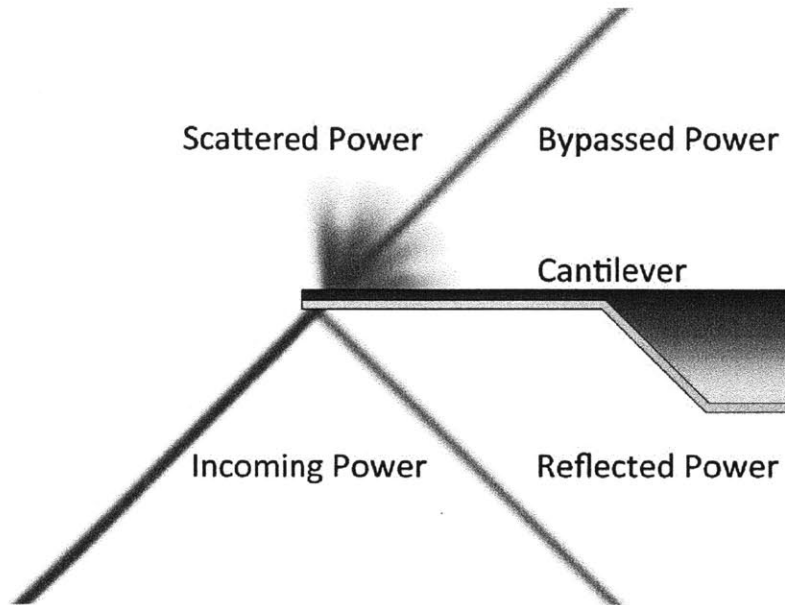
Figure 3.10: A schematic of the laser illuminating the cantilever. The cantilever will reflect, scatter or absorb the incoming power. In addition, if the laser spot is large, a portion of it will bypass the cantilever entirely. No transmission is expected as the cantilever is optically thick.

Based on these contributions, the incident power on the cantilever can be defined as,

$$P_i = P_c - P_{byp} \tag{3.17}$$

where P_i is the incident power, P_c is the incoming power and P_{byp} is the bypassed power. Because the cantilever is optically thick, no transmission will occur. The absorbed power is therefore defined as,

$$P_{abs} = P_i - P_{ref} \tag{3.18}$$

where P_{ref} is the reflected power. If the size of the beam is large, the edges of the cantilever will scatter a portion of the laser. Unfortunately this cannot be accounted for in this setup and will cause an overestimation of the absorbed power. Ideally, this source of error can be avoided if the absorptivity of the cantilever is known. In this case, the error must be minimized by ensuring the beam spot size is as small as possible.

To measure the reflected power, the photodiode is placed in the same location as the PSD. The power is then measured at the same increments previously used. The bypassed power is measured by placing the photodiode behind the cantilever. To measure the incoming power, the

photodiode is normally placed in front of the cantilever. However, because the halo around the laser is not entirely removed by the iris, the incoming power is measured behind the cantilever as well. By moving the laser off the cantilever, the effect of the halo will be cancelled upon subtracting the bypassed power from the incoming power. From these measurements, the absorbed power, P_{abs}, as a function of the laser power can be obtained using (3.17) and (3.18). Again, these measurements are done multiple times and averaged.

Given the inherent uncertainty in these measurements, the accuracy of the absorbed power can be verified by comparing the absorptivity measured with the theoretical value for gold. From the measured values, the absorptivity is defined as,

$$\alpha = \frac{P_{abs}}{P_i} \tag{3.19}$$

The theoretical absorptivity was determined using a transfer matrix model for both polarizations. The optical constants of silicon nitride and gold were obtained from the Handbook of Optical Constants.[67, 68]

The absorptivity of gold is typically quite low (0.06-0.07), thus variations in the measured value from (3.19) can have a dramatic impact on the absorption efficiency. Since the true absorptivity may vary depending on the deposition process used to create the gold film, confidence in the calibration is assessed based on how close the measured absorptivity is to the theoretical bulk value.

3.4.3.3 Frequency Response Calibration, β

The modulation of the input light source adds an additional layer of complexity as the thermal response time of the cantilever is frequency dependent. As a result, the amplitude of the deflection response is also frequency dependent. Since the power calibration is conducted at steady-state, this discrepancy will result in an underestimation of the absorbed power. Therefore, the frequency response of the cantilever must be corrected. A frequency correction factor is thus defined as follows,

$$\beta = \frac{X(f = 140 \text{ Hz})}{X(f = 0 \text{ Hz})} \tag{3.20}$$

94

where $X(f = 140\text{ Hz})$ is the amplitude of the bending response when a periodic heat input at the modulation frequency is applied and $X(f = 0\text{ Hz})$ is the amplitude of the bending response when a steady state heat input is applied. Both parameters were measured by the difference signal from the PSD as this signal is directly correlated with the bending response amplitude.

To measure β, an additional heat input is required. This is the reason for including a modulated laser in the experimental setup, as mentioned previously. Although it would be ideal to use the optical fiber itself for this measurement, the low output power simply made this impractical. The laser can be operated in both CW and modulated modes. Care must be taken to ensure that the output power is identical for both modes.

The measurement of $X(f = 0\text{ Hz})$ simply requires turning the laser on and off. The resulting change in the difference signal represents the peak-to-peak response of the cantilever. The amplitude is therefore half of this value. To measure $X(f = 140\text{ Hz})$, a frequency generator was used to create a square wave output. The amplitude was then measured by a lock-in amplifier as the frequency is high enough that averaging by the multimeters will smear this response. Once these two measurements were obtained, a simple ratio, as shown in (3.20), will result in β.

This calibration was also conducted immediately following the absorption measurement, but prior to the power calibration, to ensure experimental conditions are similar. Although the input power from the modulated laser is orders of magnitude larger than the input light source, this will not induce an error as the cantilever still operates in the linear regime. In this calibration, β was measured several times and averaged. This parameter was highly repeatable throughout the experiment.

3.4.3.4 Geometric Incident Power, P_{inc}

Recall from (3.13) the geometric incident power is defined as the product of the total power from the optical fiber at a particular wavelength and the area fraction of the beam incident on the nanowire,

$$P_{inc} = P_{tot} \cdot f$$

To measure the total power, P_{tot}, from the optical fiber, a powermeter and a photodiode were used. Due to space limitations, the optical fiber was moved as far away from the cantilever as possible. The photodiode was then placed approximately 1 cm from the end of the optical fiber to ensure optimal coverage of the detector. In this case, an attenuator attached to the photodiode was removed since the total power is small. Note that this measurement was done last as this will change the alignment of the input light source.

To measure the fraction of the beam incident on the nanowire, f, the position of the nanowire must be precisely known. This was achieved by using the dimensions of the nanowire, obtained from SEM images, and the positioning of the optical fiber to the nanowire, as discussed in Sec. 3.4.2.2. Here, the average diameter of the nanowire was used. Determination of this parameter was complicated by the fact that the beam profile of the optical fiber is Gaussian. Therefore, the standard deviation of the Gaussian, σ, at the distance separating the optical fiber and the nanowire had to be measured. This will be discussed in Ch.4, Sec. 4.1.4 when assessing the effects of variations in the angle of incidence.

Once the Gaussian profile is known, the next step is to use this information to calculate f. Using the position and the dimensions of the nanowire, we simply have to integrate the fraction of the beam incident on the nanowire. The diameter of the beam spot size was chosen to be 4σ. A larger diameter can be used, but will not appreciably change f. By assuming the beam is radially symmetric, the integral takes the following form,

$$f = \frac{1}{2\pi} \int_0^{2\pi} \left[e^{-\frac{r_2^2(\theta)}{2\sigma^2}} - e^{-\frac{r_1^2(\theta)}{2\sigma^2}} \right] d\theta \tag{3.21}$$

where the radial functions $r_1(\theta)$ and $r_2(\theta)$ define the shape of the nanowire as a function of the polar angle θ. To determine these radial functions, the cross section of the nanowire is defined by a set of lines that outline the contour of the nanowire. Lines are then radially drawn from the center of the beam spot as a function of θ. When these lines intersect the contour, the radial position of this intersection is stored in the radial functions. Since this is an integral over an area, we will always obtain a pair of intersection points, hence the two radial functions shown in (3.21). Figure 3.11 shows the intersection points for both radial functions along the contour of the measured nanowire,

96
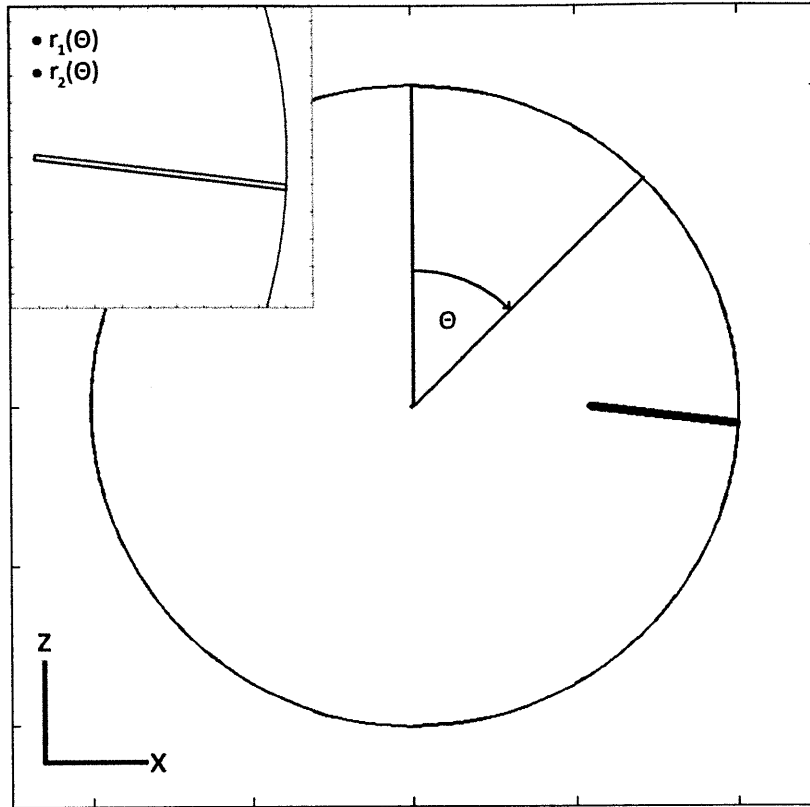
Figure 3.11: A schematic of the intersection points for the radial functions $r_1(\theta)$ and $r_2(\theta)$ used to correct for the Gaussian profile of the beam spot.

From Fig. 3.11, the nanowire is shown to be tilted at an angle. This is meant to reflect the actual orientation of the nanowire which can be seen in Fig. 3.5. Note that the integral is already normalized, thus (3.21) directly gives the area fraction.

From this calculation, it was shown that f is extremely sensitive to variations along the radial direction (x–axis) while exhibiting modest sensitivity along the lateral direction (z–axis). To reiterate, this sensitivity is an indication that the greatest source of uncertainty in this experiment comes from the alignment of the optical fiber to the nanowire.

3.5 Summary

In summary, Ch. 3 provided an overview of the experiment undertaken in this thesis. The goal of the experiment is to quantitatively and directly measure the absorption efficiency of an individual silicon nanowire. This is achieved using a bimorph cantilever to directly measure the

heat absorbed by a nanowire when illuminated with monochromatic light. A brief review of the theory for bimorph cantilevers was presented. This was followed by a description of the synthesis and attachment of the silicon nanowires. And finally, a thorough review of the AFM thermometry technique for photothermal measurements was provided. This included the preparation of the experimental setup and the choice of parameters used. Then, the methodology used to measure the various parameters needed to extract the absorption efficiency was shown. Although the current platform does not have the sensitivity to measure Si nanowires within the size range necessary to observe absorption enhancement, we can still assess the validity of this technique by measuring a larger diameter Si nanowire, as will be discussed in Ch. 4.

Chapter 4

Results and Discussion

Now that the theoretical and experimental foundation has been laid out, the next step is to assess the performance of this technique. In this chapter, the results for a larger diameter silicon nanowire will be analyzed and discussed. However, due to inherent limitations in the experimental setup, we must first modify the theoretical solutions computed in Ch. 2 to better match experimental conditions. Additional measurements will be required to assess the effects of size averaging, wavelength averaging, the polarization of the light source and the angle of incidence. This will be followed by the analysis and discussion of the experimental results.

4.1 Modification of Theory

4.1.1 Size Average

One of the key assumptions made in Mie theory is the uniformity of the wire. In reality, however, the Si nanowire samples made for this study exhibit size variation, particularly for the larger diameter wires. To account for this variation, a weighted average is used as follows,

$$Q_{abs}^{s} = \frac{1}{N}\sum_{n=1}^{N} Q_{abs}(d_n) \tag{4.1}$$

where N is the total number of points averaged along the length of the nanowire, d_n is the diameter at each point and Q_{abs}^{s} is the size averaged absorption efficiency. In (4.1), the weighted average manifests itself through the degeneracy of the diameter. The discretization of the nanowire is accomplished by first superimposing several high magnification SEM images to form a complete picture of the nanowire. The nanowire is then discretized in increments of 1% of the total nanowire length. At each point, the diameter is digitally measured according to its pixel width which is then compared to the corresponding scale bar to obtain the diameter in nanometers. This process is shown in Fig. 4.1,
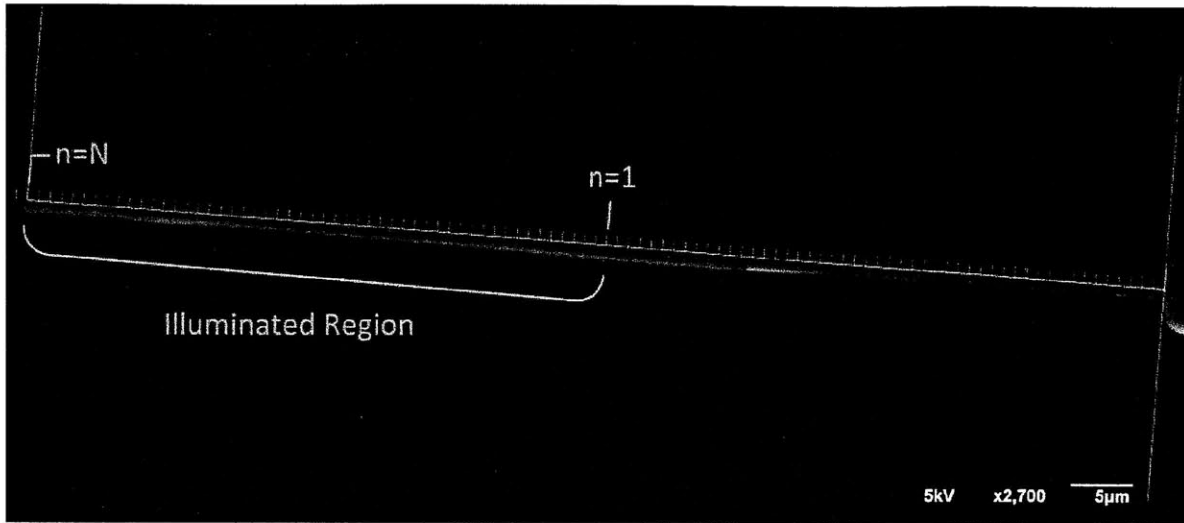
Figure 4.1: A compilation of several SEM images that form a complete picture of the nanowire. The nanowire is then discretized by the overlaid lines. The illuminated region used for size averaging is highlighted, as shown.

From Fig. 4.1, only the region illuminated by the light source is considered for size averaging. The average diameter of this region was found to be 983.1 nm with a standard deviation of 2.8 nm. Although this size averaging is a first order process, it is believed to be valid as there is no significant variation in the diameter. The size averaged absorption efficiency, Q^s_{abs}, is shown in Fig. 4.2,
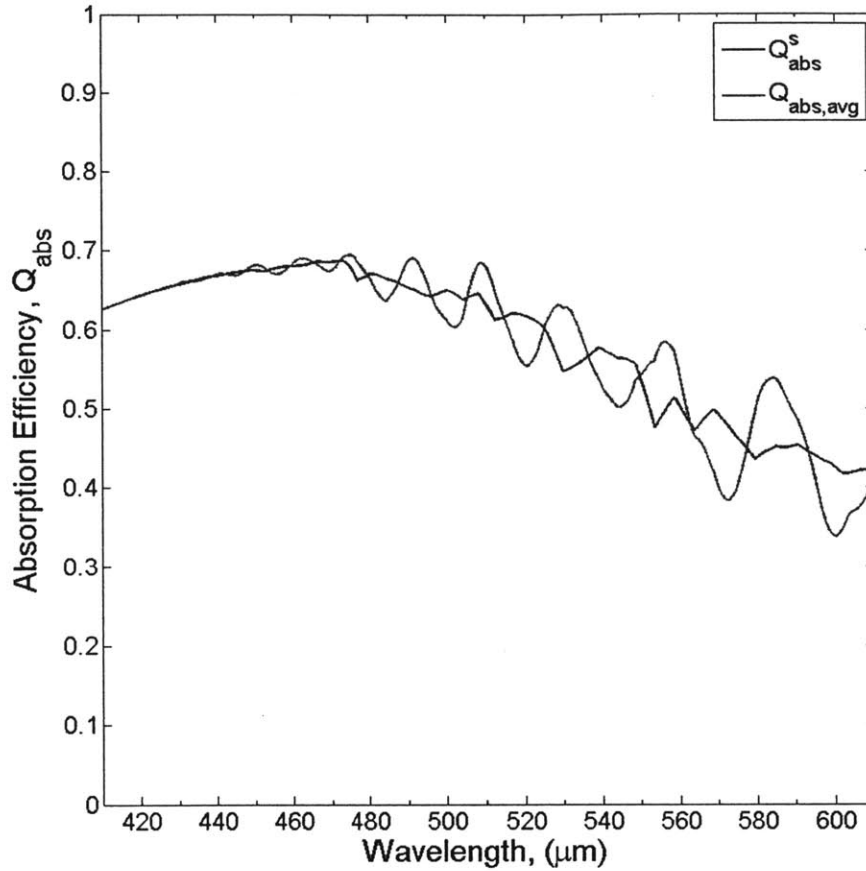
Figure 4.2: The size averaged absorption efficiency, Q^s_{abs}, obtained by (4.1) using Mie theory for silicon. This is compared with the Mie theory solution for a uniform silicon wire with a diameter of 983.1 nm.

4.1.2 Wavelength Average

In this experiment, the light from the monochromator is, ironically, not monochromatic and has a bandwidth determined by the width of the slits placed at its input and output. Although the bandwidth can be decreased to better match with theory, this will also reduce the throughput power. Since this experiment is dependent on measuring the light absorbed by the nanowire, a decrease in the light input may reduce the absorbed power to below the power sensitivity of the system. Therefore, the bandwidth of the source, or full-width half-maximum (FWHM), was set to a minimum of 7-8 nm to ensure the throughput power was unaffected. As a result, the theoretical absorption efficiency must be averaged over the bandwidth of the light source.

The FWHM at each wavelength was measured when calibrating the monochromator, as mentioned in Ch.3, Sec. 3.4.2.4. To approximate the shape of the peak, a linear fit is used whose slope is determined by the FWHM, as shown in Fig. 4.3,

(a)   (b)
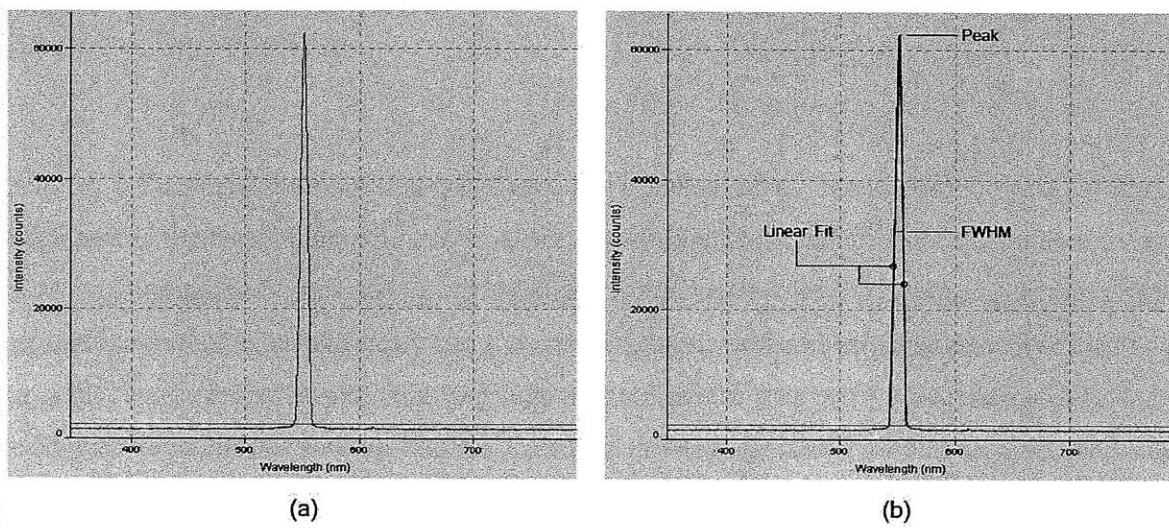
Figure 4.3: (a) An example of the monochromator output measured using an Ocean Optics spectrometer at $\lambda = 550\,\text{nm}$ (b) The linear fitting applied to the output using the full-width half-maximum (FWHM).

The wavelength is then discretized into increments of 0.1 nm and averaged as follows,

$$Q_{abs}^{\lambda} = \frac{\sum_{n=1}^{N} w_n \cdot Q_{abs}(\lambda_n)}{\sum_{n=1}^{N} w_n} \qquad (4.2)$$

where w_n is the linear fitting weight, λ_n is the wavelength and Q_{abs}^{λ} is the wavelength averaged absorption efficiency. In (4.2), the fitting is normalized and extrapolated from a weight of 0 to the peak normalized value. The size and wavelength averaged absorption efficiency, $Q_{abs}^{\lambda,s}$, is shown in Fig. 4.4,
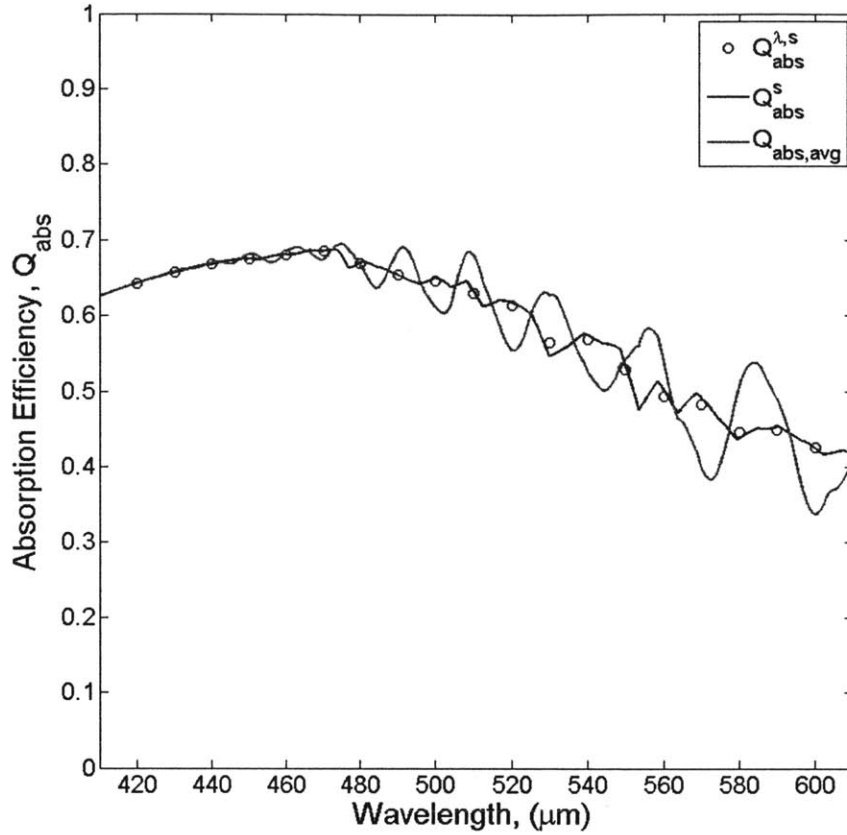
Figure 4.4: The size and wavelength averaged absorption efficiency, $Q_{abs}^{\lambda,s}$, obtained with (4.1) and (4.2) using Mie theory for silicon. This is compared with the size averaged absorption efficiency, Q_{abs}^{s}, and the Mie theory solution for a uniform silicon wire with a diameter of 983.1 nm.

4.1.3 Polarization

From Ch. 2, it was shown that the Mie solutions are polarization dependent. The absorption efficiencies calculated in Figs. 4.2 and 4.4 have assumed the incident light was perfectly unpolarized. However, in the experiment, this may not necessarily be the case. To validate this assumption, the Stokes parameters, which provides information on the polarization state, of the light source was measured. The Stokes parameters consist of four numbers typically arranged as a vector: S_0 is the intensity of the source, S_1 and S_2 are two linear polarization states and S_3 is the circular polarization state.

103

In principle, only the first three Stokes parameters (S_0, S_1, S_2) need to be measured for this experiment since a circular polarization state will not affect the final results. For the sake of completion, we measure all Stokes parameters using an optical train consisting of a half-wave plate and a linear polarizer as shown in Fig. 4.5,

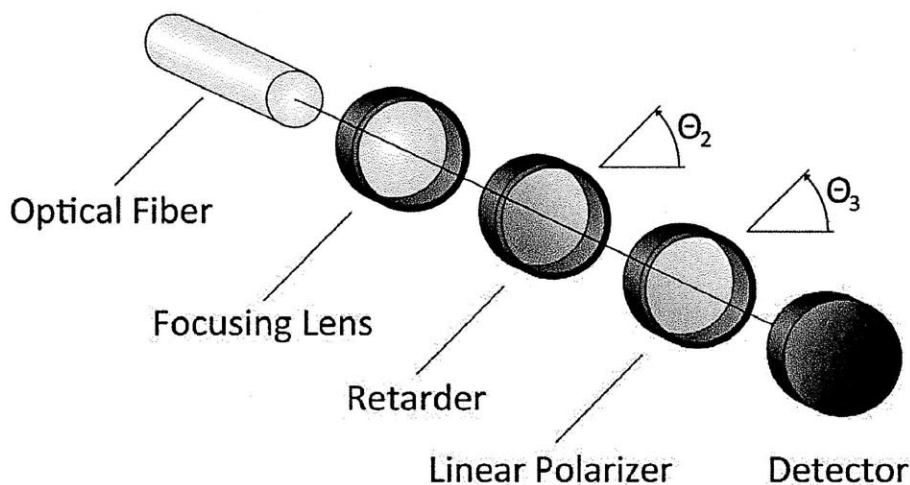Figure 4.5: Optical train system used to measure the Stokes parameters of the light source.

where a lens is used collimate the light source from the optical fiber. All angles of rotation are taken relative to the polarization axis for the linear polarizers and the fast axis for the waveplate. In typical measurements, a quarter-wave plate must be used instead of a half-wave plate in order to measure the circular polarization state. However the retardation of commercial wave plates is a strong function of wavelength and is thus only rated at a particular wavelength when used. In the case of a half wave-plate, so long as the wavelength of the source is different from its rated wavelength, the retardation will not result in a 180 degree phase shift. Therefore, a half-wave plate can still be used under these conditions to measure the circular polarization state in the system so long as the phase shift is calibrated. In addition, we expect the polarization state could vary with the wavelength of the source; hence, we measure the Stokes parameters at different wavelengths spanning the range in which we conduct our experiment at (420 nm, 500 nm, 600 nm). Note that the half-wave plate is rated at 650 nm.

To calibrate for the unknown phase shift of the half-wave plate, we use an additional linear polarizer placed in front of the half-wave plate. This system is shown in Fig. 4.6 below,
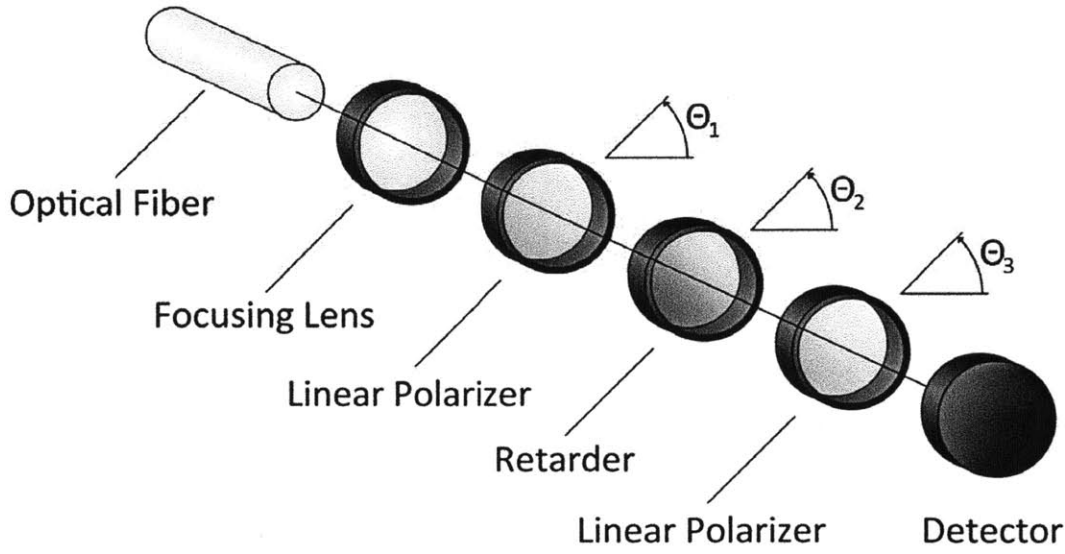
Figure 4.6: Optical train system to measure the retardation of the half-wave plate.

In general, we can obtain all Stokes parameters of the source by measuring the output intensity when the optical components are rotated to different positions. The rotation angles of the components are controlled by rotational mounts. It is in this manner that we can obtain the phase shift of the half-wave plate. To relate the source with the output intensity, we use a product of Mueller matrices representative of the optical system used. In general, the Mueller matrix for a linear polarizer rotated at an arbitrary angle is,

$$M = \frac{1}{2} \begin{bmatrix} 1 & \cos2\theta & \sin2\theta & 0 \\ \cos2\theta & \cos^2 2\theta & \sin2\theta\cos2\theta & 0 \\ \sin2\theta & \sin2\theta\cos2\theta & \sin^2 2\theta & 0 \\ 0 & 0 & 0 & 0 \end{bmatrix} \tag{4.3}$$

where θ is the angle of rotation relative to the horizontal axis. Similarly, for a wave plate, the Mueller matrix is,

$$M = \frac{1}{2} \begin{bmatrix} 1 & 0 & 0 & 0 \\ 0 & \cos^2 2\theta + \cos\phi\sin^2 2\theta & (1-\cos\phi)\sin2\theta\cos2\theta & \sin\phi\sin2\theta \\ 0 & (1-\cos\phi)\sin2\theta\cos2\theta & \sin^2 2\theta + \cos\phi\cos^2 2\theta & -\sin\phi\cos2\theta \\ 0 & -\sin\phi\sin2\theta & \sin\phi\cos2\theta & \cos\phi \end{bmatrix} \tag{4.4}$$

where ϕ is the unknown phase shift. To relate the input source to the output intensity, we multiply the Mueller matrices in the order that they are placed in the system,

$$S_o = \underbrace{M_3 M_2 M_1}_{M} S_i \tag{4.5}$$

where S_i and S_o are the Stokes vector for the input and output, respectively. Since we can only measure the output intensity, we simply need the first row of the matrix M. The result of substituting (4.3) and (4.4) into (4.5) and assuming $\theta_1 = \theta_3 = 45°$ is thus,

$$I(\theta_2) = (S_0 + S_3)(1 + \sin^2 2\theta_2 + \cos\phi\cos^2 2\theta_2) \tag{4.6}$$

To cancel S_0 and S_3, we can measure the intensity when the fast axis of the half-wave plate is positioned at $\theta_2 = 0°$ and $\theta_2 = 45°$,

$$I(\theta_2 = 0°) = (S_0 + S_3)(1 + \cos\phi)$$

$$I(\theta_2 = 45°) = (S_0 + S_3)(2)$$

If we take the ratio and rearrange terms, we obtain,

$$\cos\phi = 2\frac{I(\theta_2 = 0°)}{I(\theta_2 = 45°)} - 1 \tag{4.7}$$

We note that the absorption losses of the optical components are not accounted for in this analysis. As will be shown in the measurement, this level of accuracy is not required.

Now, to measure the Stokes parameters of the source, we follow the same procedure. From Fig. 4.5, we only need to account for the wave plate and one linear polarizer. The resulting product is,

$$I(\theta_2, \theta_3) = \frac{1}{2}S_0 + \ldots$$

$$\ldots + \frac{1}{2}S_1\left[\cos 2\theta_3\left(\cos^2 2\theta_2 + \cos\phi\sin^2 2\theta_2\right) + \sin 2\theta_3\left(1 - \cos\phi\right)\sin 2\theta_2\cos 2\theta_2\right] + \ldots$$

$$\ldots + \frac{1}{2}S_2\left[\cos 2\theta_3\left(1 - \cos\phi\right)\sin 2\theta_2\cos 2\theta_2 + \sin 2\theta_3\left(\sin^2 2\theta_2 + \cos\phi\cos^2 2\theta_2\right)\right] + \ldots$$

$$\ldots + \frac{1}{2}S_3\left[\cos 2\theta_3\sin\phi\sin 2\theta_2 - \sin 2\theta_3\sin\phi\cos 2\theta_2\right]$$

$$\tag{4.8}$$

To isolate each Stokes parameter in (4.8), the optical components are again rotated to different positions as before. Only four configurations are needed,

$$I\left(\theta_2 = 45^\circ, \theta_3 = 0^\circ\right) = \frac{1}{2}\left(S_0 + S_1\cos\phi + S_3\sin\phi\right)$$

$$I\left(\theta_2 = 45^\circ, \theta_3 = 90^\circ\right) = \frac{1}{2}\left(S_0 - S_1\cos\phi - S_3\sin\phi\right)$$

$$I\left(\theta_2 = 45^\circ, \theta_3 = 45^\circ\right) = \frac{1}{2}\left(S_0 + S_2\right)$$

(4.9)

$$I\left(\theta_2 = 0^\circ, \theta_3 = 45^\circ\right) = \frac{1}{2}\left(S_0 + S_2\cos\phi - S_3\sin\phi\right)$$

From (4.9), we can show that,

$$S_0 = I\left(\theta_2 = 45^\circ, \theta_3 = 0^\circ\right) + I\left(\theta_2 = 45^\circ, \theta_3 = 90^\circ\right)$$

$$S_1 = \frac{1}{\cos\phi}\left[I\left(\theta_2 = 45^\circ, \theta_3 = 0^\circ\right) - I\left(\theta_2 = 45^\circ, \theta_3 = 90^\circ\right) - S_3\sin\phi\right]$$

$$S_2 = 2\cdot I\left(\theta_2 = 45^\circ, \theta_3 = 45^\circ\right) - S_0$$

(4.10)

$$S_3 = \frac{1}{\sin\phi}\left[-2\cdot I\left(\theta_2 = 0^\circ, \theta_3 = 45^\circ\right) + S_0 + S_2\cos\phi\right]$$

Therefore, to determine the polarization state of the light source, we simply need to measure the intensity of the source at different optical configurations according to (4.7) and (4.10). To measure the intensity, we once again use a powermeter and a photodiode (Newport, 1918C/818-UV) calibrated at the measured wavelengths. The results are summarized in Table 4.1,

Table 4.1: The measured Stokes parameters at different wavelengths.

Wavelength (nm)	Phase Retardation (degrees)	S_0 (µW)	S_1 (µW)	S_2 (µW)	S_3 (µW)	Degree of Polarization, P
420	46.2	643.7	-22.4	12.6	7.5	0.0416
500	114.4	952.9	12.2	2.4	-4.7	0.0139
600	159.6	637.5	-7.7	17.4	-89.5	0.1436

where the degree of polarization is defined as,

$$P = \frac{\sqrt{S_1^2 + S_2^2 + S_3^2}}{S_0}$$

From Table 4.1, we can clearly see that the light source used in this experiment is for all intents and purposes unpolarized as the Stokes vector at all wavelengths is close to the ideal Stokes vector of $S_o = \begin{bmatrix} 1 & 0 & 0 & 0 \end{bmatrix}'$ for unpolarized light. Although the degree of polarization is relatively high at 600 nm, this is primarily due to the presence of a circular polarization state which does not affect the absorption efficiency in this experiment. Therefore, our original assumption that the incident light in the experiment is unpolarized is validated.

4.1.4 Angle of Incidence

As discussed in Ch.3, Sec. 3.4.2.2, the cantilever is manually positioned to align the nanowire to the optical fiber. Furthermore, light from the optical fiber will diverge within an exit cone determined by the numerical aperture. In both cases, variations in the angle of incidence must be assessed. In this section, the following analysis can be found in Collett.[69] We shall denote the light transmitted by the optical fiber as a source positioned at the tip of the optical fiber. Since the light source is Gaussian, the contributions from different angular components in the light source must be appropriately weighed. In general, we can model a fluctuating, radiating light source in the far–field limit as,

$$J^{(\infty)}(s,v) = z^2 \cdot S(\rho,z;v) \tag{4.11}$$

where $J^{(\infty)}$ is the radiant intensity, S is the spectral intensity, v is the frequency of light, z is distance from the point of interest to the source along the fiber axis and ρ is the radial distance from the source to the point of interest perpendicular to the fiber axis. Figure 4.7 shows the system under consideration,
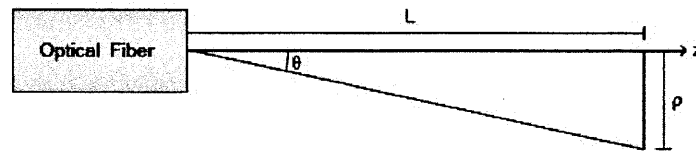

Figure 4.7: Coordinate system used to determine the radiant intensity, $J^{(\infty)}$.

From (4.11), it can be observed that $J^{(\infty)}$ is only a function of direction. Therefore, this is the parameter that can be used to assess the angular distribution of the Gaussian divergence cone. For a fixed wavelength, we can write the radiant intensity to be a function of the incident angle,

$$J^{(\infty)}(\theta) = z^2 \cdot S(z \cdot \tan\theta, z) \qquad (4.12)$$

where θ is the incident angle. To determine $J^{(\infty)}$, we must first define S, the spectral intensity appropriate for the light source in this experiment. This must account for both the Gaussian intensity profile as well as the incoherency of the light source. The incoherency is evident from the relatively large bandwidth of the source, as mentioned in Sect. 4.1.2. To account for these characteristics, we use a Gaussian-Schell model for the light source.

In this model, the spectral intensity and the coherency are both defined as Gaussian functions as follows,

$$S^0(\rho, z) = A(v)^2 \cdot e^{-\frac{\rho^2}{2\sigma_s^2}} \qquad (4.13)$$

$$g^0(\rho', z) = e^{-\frac{\rho'^2}{2\sigma_g^2}} \qquad (4.14)$$

where A is a wavelength dependent amplitude, σ_s is the standard deviation of the spatial term, $\rho' = \rho_2 - \rho_1$ is the distance between two points in the system and σ_g is the standard deviation of the coherency function at the origin of the source, as denoted by the superscript. To determine these distributions as a function of position, we use a cross-spectral intensity. In general, a cross-spectral density is a measure of the correlation between the fluctuations of different components at a given frequency,

$$W^0(\rho_1, \rho_2, v) = \left[S^0(\rho_1, v) \right]^{1/2} \left[S^0(\rho_2, v) \right]^{1/2} g^0(\rho_2 - \rho_1, v) \qquad (4.15)$$

where ρ_1 and ρ_2 denote two separated points. In the case where $\rho_1 = \rho_2$, the cross-spectral intensity is equal to the spectral intensity. Upon substituting (4.13) and (4.14) into (4.15), we can obtain the following,

$$S(\rho, z) = \frac{A^2}{\Delta(z)^2} \cdot e^{-\frac{\rho^2}{2[\sigma_s \cdot \Delta(z)]^2}} \qquad (4.16)$$

where,

$$\Delta(z) = \sqrt{1 + \left(\frac{\lambda z}{2\pi\sigma_s a}\right)^2}$$ (4.17)

and,

$$\frac{1}{a^2} = \frac{1}{(2\sigma_s)^2} + \frac{1}{\sigma_g^2}$$ (4.18)

In (4.17), λ is the wavelength of light. In (4.18), we can observe that for a spatially incoherent source, $\sigma_s >> \sigma_g$, the coherency parameter can be approximated as $a \cong \sigma_g$. Since we are operating in the far-field limit, (4.17) simplifies to become,

$$\lim_{z \to \infty} \Delta(z) = \frac{\lambda z}{2\pi\sigma_s\sigma_g}$$ (4.19)

Upon substituting (4.19) into (4.16) and subsequently (4.12), we will find the radiant intensity to be,

$$J^{(\infty)}(\theta) = \left(\frac{2\pi\sigma_s\sigma_g A}{\lambda}\right)^2 e^{-\frac{1}{2}\left(\frac{2\pi\sigma_g \tan\theta}{\lambda}\right)^2}$$

Since we are only interested in the angular dependence, this expression becomes,

$$J^{(\infty)}(\theta) \propto e^{-2\left(\frac{\pi\sigma_g \tan\theta}{\lambda}\right)^2}$$ (4.20)

From (4.20), $J^{(\infty)}$ can be determined by measuring σ_g. The wavelength is determined based on the previous calibration of the light source, as mentioned in Ch.3, Sec.3.4.2.4. To measure σ_g, we must go back to (4.16). In principle, if the standard deviation, $\sigma_s \cdot \Delta(z)$, is measured at different positions along z, we can then use (4.17) and guess values for σ_s and σ_g to fit the data.

In order to measure the standard deviation, $\sigma_s \cdot \Delta(z)$, we measure the beam profile using a knife–edge technique at a wavelength of 470 nm, which corresponds to the peak wavelength of the source. Although $J^{(\infty)}$ is wavelength dependent, the radiant intensity will not vary significantly within the narrow wavelength range the experiment is conducted at. A razor blade is mounted onto a motor mike along the x–axis to enable lateral movement relative to the optical

fiber. The blade is then positioned so that the light source is completely blocked and then retracted in increments until the light source is unblocked. At each position, the optical power is measured using a powermeter. Assuming the profile is radially symmetric, the integral of the intensity profile will be measured. Since the beam profile is Gaussian, the standard deviation, $\sigma_s \cdot \Delta(z)$, can be determined by fitting the data to an error function. Figure 4.8 shows an example set of data measured at a distance of $z = 8$ mm and the corresponding fitting,
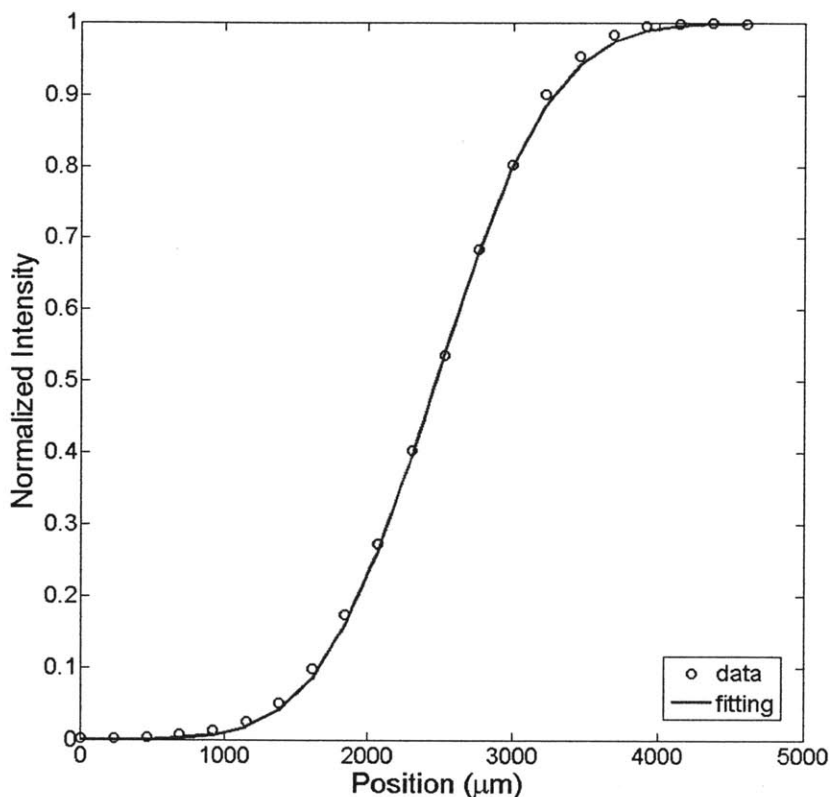
Figure 4.8: An example set of data taken at $z = 8$ mm using the beam profiling setup described. It can be clearly observed that this data corresponds to an error function, as shown by the fitting.

This measurement is then repeated at several distances by moving the optical fiber from the detector with a micrometer. Furthermore, dividing $\sigma_s \cdot \Delta(z)$ by σ_s will normalize the data such that $\Delta(z = 0) = 1$ at the origin. The collective data for the standard deviation, $\Delta(z)$, is shown in Fig. 4.9,

111
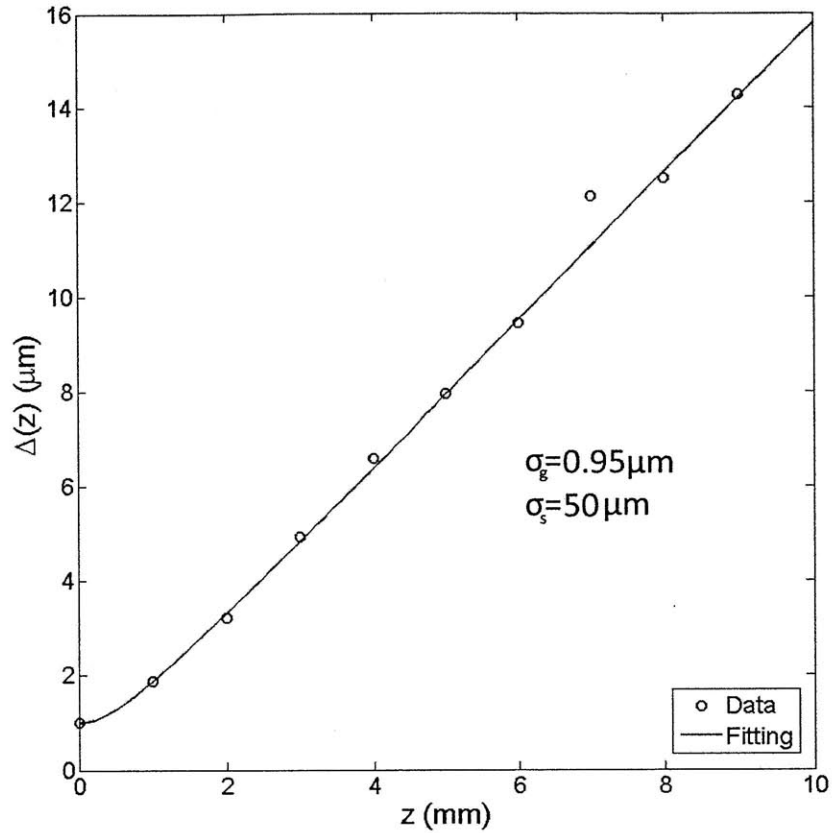
Figure 4.9: The results for $\Delta(z)$ as a function of the separation distance z. Based on the fitting the standard deviations σ_s and σ_g were determined to be $50\,\mu m$ and $0.95\,\mu m$, respectively.

From Fig. 4.9, the standard deviations σ_s and σ_g were fitted using (4.17) with values of $50\,\mu m$ and $0.95\,\mu m$, respectively. Based on this fitting, the radiant intensity, $J^{(\infty)}$, can now be determined. From (4.20), the angular distribution of the light source is shown is shown in Fig. 4.10,
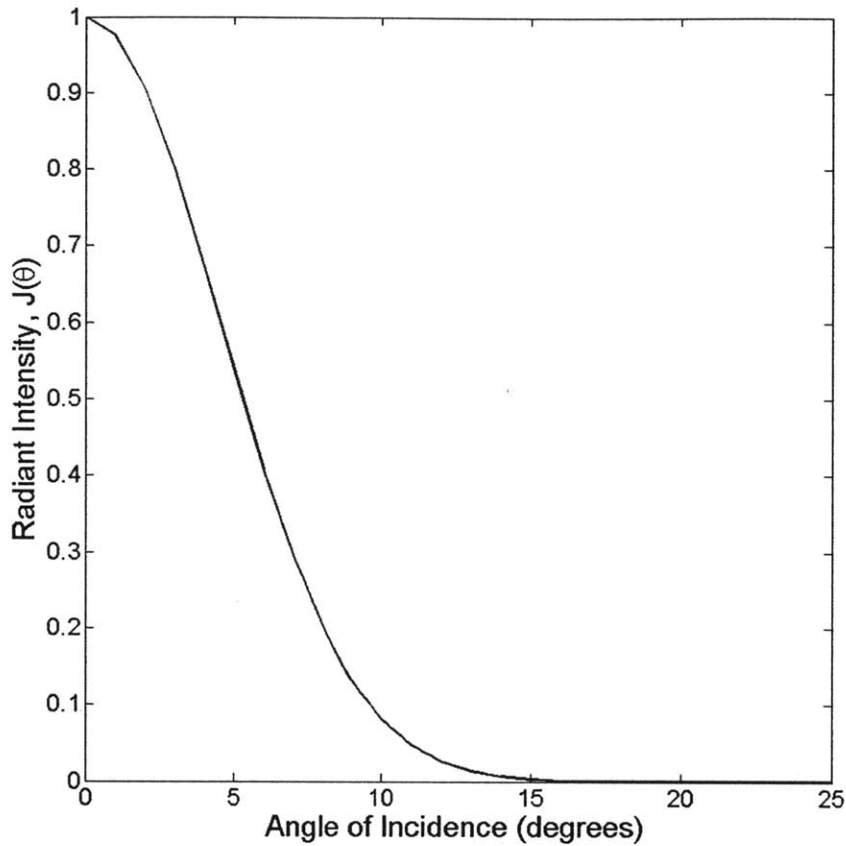
Figure 4.10: The angular distribution, $J^{(\infty)}$. As shown, angular components above 15 degrees are negligible.

As shown, angular components above 15 degrees are negligible and the most dominant components are situated near the origin. Therefore, to account for this angular distribution in the theoretical solution, we would utilize $J^{(\infty)}$ as a weighing function. However, if we were to simply calculate the Mie solution for a cylinder at the limiting angle of incidence at 15 degrees and compare with the solution at normal incidence, we can observe that the difference between solutions is quite small,
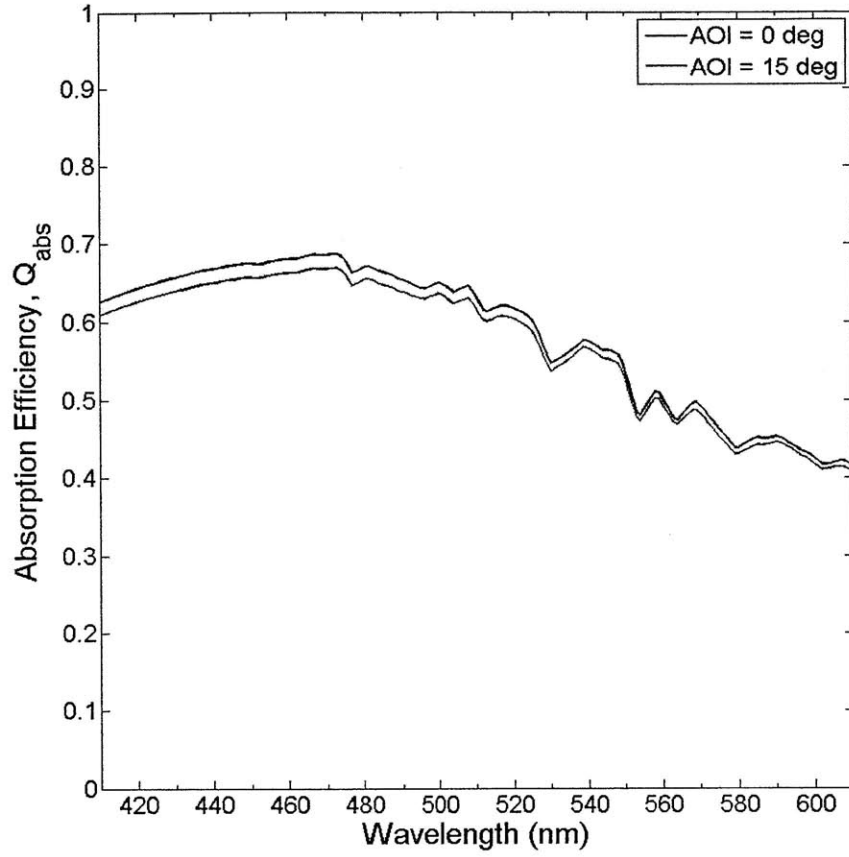
Figure 4.11: The size averaged absorption efficiency at normal incidence and at 15 degrees angle of incidence.

From Fig. 4.11, we can conclude that any variations in the angle of incidence due to the divergence cone of the optical fiber do not significantly affect the results in this experiment. Furthermore, any uncertainty in the alignment of the nanowire to the optical fiber will also not be significant. Therefore we can simply use the solution at normal incidence to compare with the experimental results.

4.2 Results/Discussion

Recall from Ch.3 the absorption efficiency can be written as follows,

$$Q_{abs}(\lambda) = \frac{P_{abs}}{P_{inc}} = \frac{\left(\dfrac{X(\lambda)}{\beta \cdot S_p}\right)}{P_{tot}(\lambda) \cdot f_{area}} \tag{4.21}$$

114

where the absorbed power and geometric incident power have been expanded into the relevant experimental parameters. Note that in (4.21), only the deflection response, X, and the total power, P_{tot}, are a function of wavelength. For the absorption measurement, the raw deflection response, X, was measured three times, as shown,
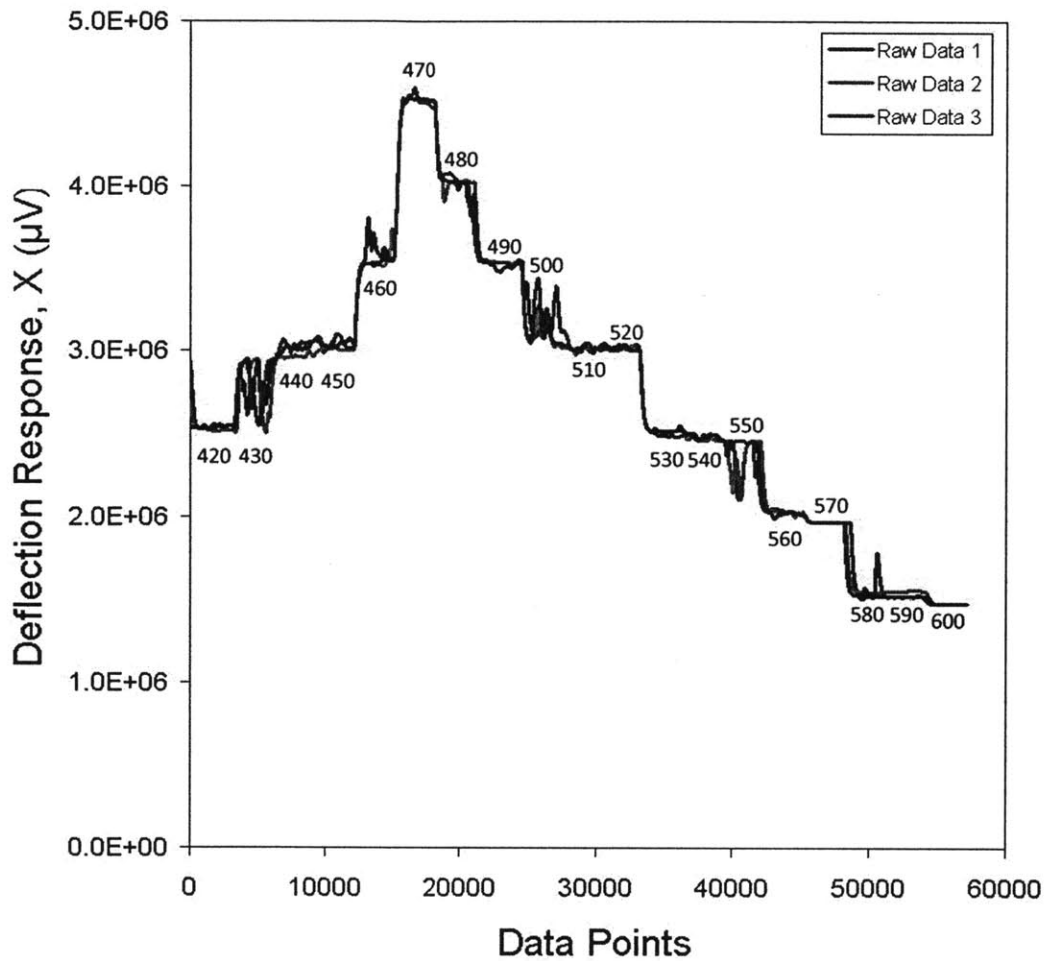
Figure 4.12: The raw deflection response, X, as measured for the absorption measurement. Each step in the data represents one wavelength interval incremented by 10 nm. The intervals are averaged. Three sets of data were taken and as shown, are highly repeatable.

From Fig. 4.12, it can be observed that the absorption measurement is highly repeatable. Furthermore, a clear trend can be observed which is indicative that the sample is well within the

power sensitivity limitations of the system. Each wavelength interval for each set of data is averaged.

The frequency correction factor, β, was then measured for each corresponding set of data to ensure the parameter was obtained under consistent experimental conditions. The measured values were $\beta = 0.4032$, 0.4032, 0.4030 for datasets 1, 2 and 3, respectively. Again, this parameter is highly repeatable throughout the entire experiment. These values indicate the significance of the cantilever frequency response as the amplitude exhibited nearly 40% attenuation. This would suggest a lower modulation frequency should be used in the future, provided the noise in the system can be reduced

A power calibration was then conducted to obtain the power sensitivity, S_p, for each dataset. As discussed in Ch.3, this calibration requires measurements in both vacuum and ambient conditions. In vacuum, measurements were again conducted for each data set to ensure consistent experimental conditions. However, in air, the measurements conducted were applied to all three datasets. The measured power sensitivities were $S_p = -104.1, -103.7, -103.9$ V/mW again for datasets 1, 2 and 3, respectively. Once again, this parameter was highly repeatable throughout the experiment. To verify the accuracy of this calibration, the absorptivity measured was on average 0.0643 for all laser powers. Using a transfer matrix model (TMM), the absorptivity at an angle of incidence of 20 degrees was theoretically predicted to be 0.0607 and 0.0694 for TE and TM polarizations, respectively. Therefore, this calibration is in good agreement with theory and can therefore be trusted.

Under ambient conditions, the geometric incident power, P_{inc}, was also measured. First, the total power from the optical fiber, P_{tot}, was measured at each wavelength. Two datasets were measured and then averaged, as shown,
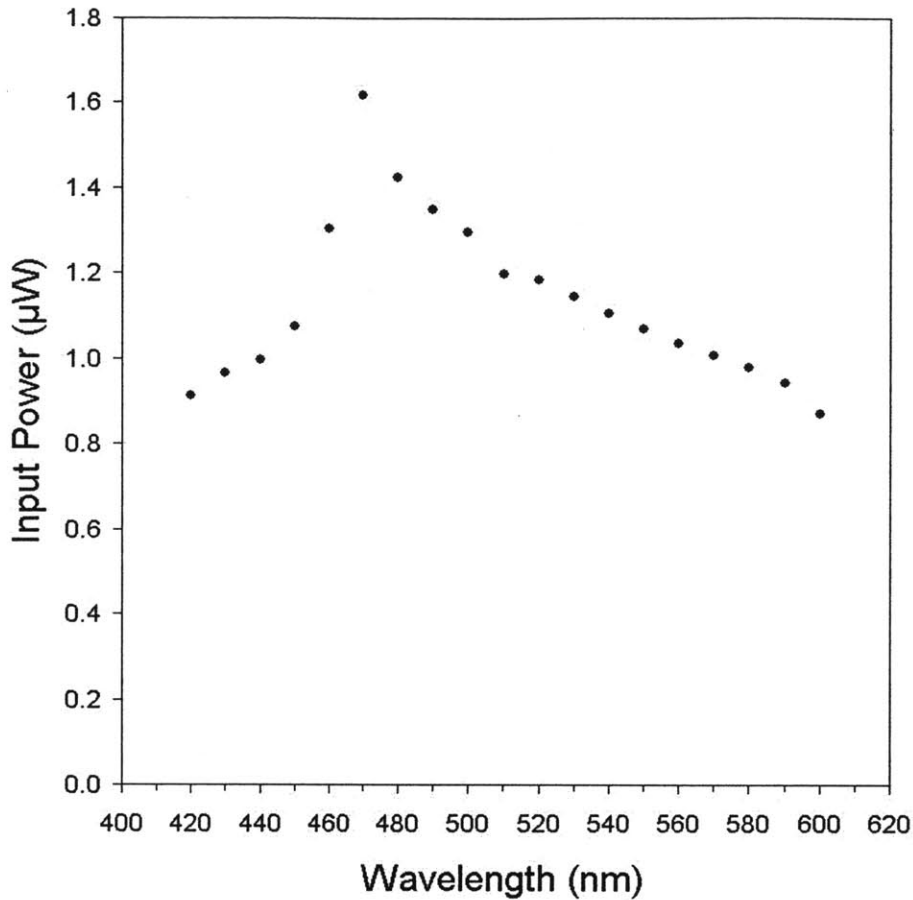
Figure 4.13: The averaged total power, P_{tot}, as measured from the optical fiber. This data is averaged only over two data sets as this was a highly repeatable measurement.

From Fig. 4.13, the light source exhibits a very strong spectral peak at 470 nm. Although this spectral peak did not increase the uncertainty at this particular wavelength, other sharp spectral features were observed within this wavelength range when calibrating the monochromator. This may be the reason for the repeatable variations observed in Fig. 4.12 which would suggest that an alternative light source with a smoother spectrum should be used. However, at present, these variations are not significant enough to require alterations to the system as the bandwidth of the light output will average these variations.

To determine the fraction of light, f, incident on the nanowire, the position and the geometry of the nanowire are used as mentioned before. The wire is approximately offset 15 μm along the z-axis. Based on this information, the fraction was determined to be

$f = 9.83 \times 10^{-4}$. Given that this fraction is quite small, uncertainty in the position of the nanowire within the beam spot could change the absorption efficiency substantially. In fact, this parameter exhibits the greatest uncertainty due to the alignment procedure, as outlined in Ch.3, Sec. 3.4.2.2, thus an improved of alignment would be a worthwhile pursuit in future studies.

From (4.21), the absorbed power by the nanowire ranged from 352 pW at 600 nm to 1.08 nW at 470 nm. Likewise, the geometric incident power ranged from 856 pW at 600 nm to 1.589 nW at 470 nm. The absorption efficiency of the nanowire is shown in Fig. 4.14,
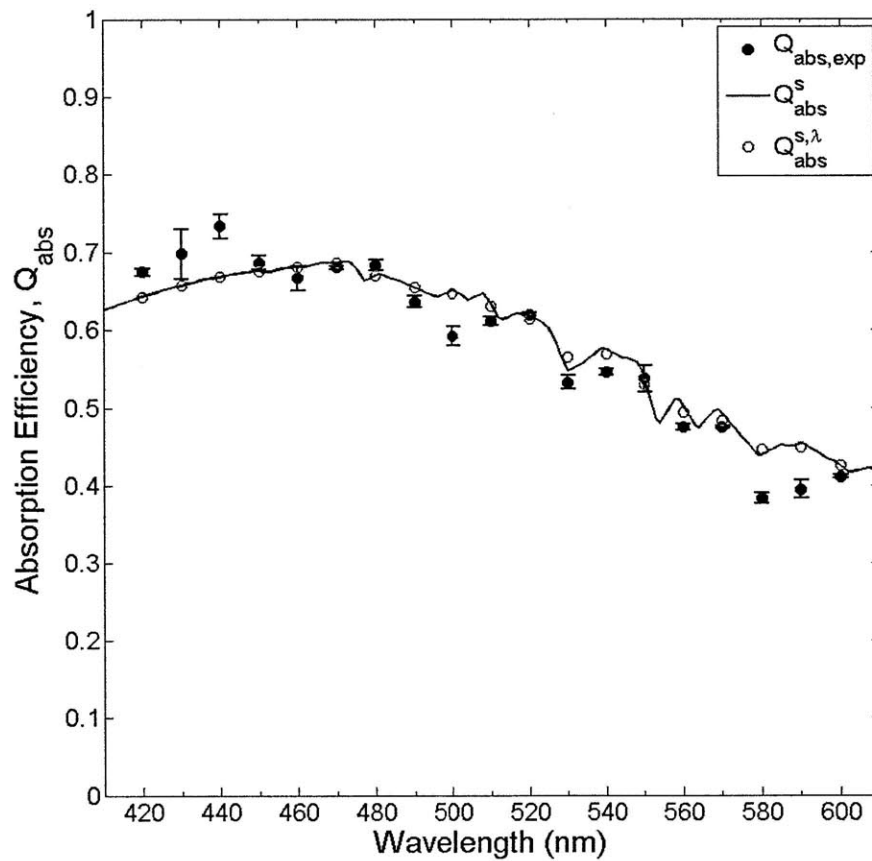
Figure 4.14: The measured absorption efficiency, $Q_{abs,\exp}$, for a silicon nanowire with an average diameter of $D = 983.1$ nm as measured along only the illuminated region. The data was averaged over three sets of data. The error bars correspond to two standard deviations (95% confidence interval) from the three data sets. This is compared to the size averaged absorption efficiency, Q_{abs}^{s}, and the size and wavelength averaged absorption efficiency, $Q_{abs}^{\lambda,s}$.

where $Q_{abs,exp}$ is the measured absorption efficiency averaged over all three datasets and compared to the averaged absorption efficiencies Q_{abs}^s and $Q_{abs}^{\lambda,s}$. The error bars correspond to two standard deviations, a 95% confidence interval, between the three datasets. Note that these error bars are not indicative of the total uncertainty present in the measurement as this may be much higher due to the issues previously mentioned.

The average absolute error was determined to be 4.69% with a minimum of 0.75% at 470 nm and a maximum of 14.2% at 580 nm. Overall, the data appears to follow the theoretical trend where the absorption efficiency peaks near 470-480 nm and decreases at longer wavelengths. However, additional spectral features at 440, 500 and 580 nm do appear which deviate from the theoretical curve. This may be due to variations in the light source or more likely differences in the nanowire, such as the optical constants due to the synthesis process, size variation effects not captured by the averaging or even contamination from the attachment process, all of which are not accounted in the theoretical solution.

Despite the differences from theory, the data, as shown in Fig. 4.14, is in overall good agreement with the theoretical curves in terms of both the magnitude as well as the trend. Although this particular Si nanowire does not exhibit any enhancement in the absorption efficiency, the data measured nonetheless validates the use of AFM thermometry to measure the absorption efficiency of nanostructures directly and quantitatively. Therefore, this sample serves as a stepping stone from which future studies on smaller, more interesting samples can now be pursued.

4.3 Summary

In summary, Ch.4 presented measured data on a larger diameter Si nanowire ($D = 983.1$ nm). First, the theoretical solutions obtained from Mie theory had to be modified to account for limitations in the experiment. This included both size averaging and wavelength averaging. Fortunately, it was demonstrated that the light source is indeed unpolarized and variations in the angle of incidence, due to the divergence of the source and misalignment, have minimal effect on the theoretical results. Based on these modifications, it was shown that the measured data is in good agreement in terms of both the magnitude and the trend. Although there are minor differences with theory, the data is nonetheless conclusive evidence that AFM thermometry can indeed be used to measure the absorptive properties of nanostructures. In order to measure

samples which exhibit absorption enhancement, additional modifications must be made as will be discussed in Ch. 5.

Chapter 5

Summary and Future Outlook

5.1 Summary

The manipulation of optical properties in photonic nanostructures remains an active field of study. In order to understand the effects of the geometry, periodicity and material choice for such structures, conventional spectroscopy techniques have been used to assess the absorptive properties. However, these techniques typically consist of either an indirect or qualitative measurement of absorption. In this work, a method based on AFM cantilever thermometry is presented which can be used to both directly and quantitatively measure the absorption efficiency of individual nanostructures. Specifically, an individual silicon nanowire was measured and shown to agree well with theory.

The motivation for the study on silicon nanowires is based on theoretical results which predict strong enhancement in absorption ($Q_{abs} > 1$) within the visible wavelength range. These results are based on the well known Mie theory. The theory consists of analytical solutions to the Maxwell equations solved for the particular case where a harmonic plane wave is incident on an infinitely long cylinder. Based on these results, it was shown that silicon nanowires support many leaky mode resonances. When the diameter of the wire is smaller than 150 nm, the lowest order modes exhibit strong dipole–like behavior which results in an absorption efficiency greater than 1. In addition, the size of the nanowire can be adjusted to tune the absorption peak within the wavelength range.

To measure the absorption efficiency, an AFM bimorph cantilever is used as a photothermal sensor. A single nanowire, synthesized using an electroless etching technique, was first attached to the cantilever. By illuminating a portion of the nanowire with monochromatic light, the absorbed power will conduct through the nanowire and the cantilever as heat. The resulting change in temperature across the cantilever will then cause the cantilever to bend which is measured optically. After appropriate calibrations, the absorption efficiency can be extracted.

Based on this method, the absorption efficiency of a silicon nanowire with a diameter of 983.1 nm was measured from 420 nm to 600 nm. A larger diameter was chosen as the current system does not have the necessary sensitivity to measure a wire with a diameter less than 150 nm. After modifying the theoretical solution to account for limitations in the experimental setup, the measured results were shown to be in good agreement with theory in terms of both the magnitude and trend. The average absolute error across the wavelength range was 4.69%. Additional spectral features were observed in the data which deviate from theory. Possible reasons may include a difference in the optical constants due to the synthesis process, size variation effects which are not accounted for in the averaging or even possibly contamination of the sample during the attachment process. Nonetheless, the results validate the use of this method to directly and quantitatively measure the absorption efficiency of individual nanostructures.

5.2 Future Outlook

The results in this thesis represent an important step towards accomplishing the ultimate goal of measuring nanostructures with an enhanced absorption efficiency. However, several modifications need to be made to the experiment before these measurements can proceed. The two key issues that must be addressed are the uncertainty and the sensitivity in the platform. A comprehensive uncertainty analysis must be conducted to assess which aspects of the experiment contribute most to the uncertainty. At present, the largest source of uncertainty is in the alignment of the optical fiber and the nanowire. Since the fraction of light incident on the sample, f, is quite small, the position of the nanowire in the incident beam spot must be known with a high degree of precision. The power calibration should also be conducted entirely in vacuum to eliminate uncertainties when correlating the PSD output between vacuum and ambient conditions. In addition, an improved set of optics should be integrated to decrease the size of the detector laser beam. This will also reduce uncertainties in the power calibration when measuring the absorbed power.

To improve the sensitivity of the platform, the signal-to-noise ratio must increase. This can be accomplished by increasing the throughput power and reducing the minimum detectable power. The throughput power can be improved by using a higher intensity light source and better optics to increase the coupling efficiency with the optical fiber. To reduce the minimum detectable power, a new cantilever can be used. Recently, a bi-arm cantilever was proposed

which decouples the sample from the bimorph, or detector.[70] The cantilever consists of a single layer silicon nitride sample arm with a bilayer silicon nitride/gold detector arm connected at its midpoint, as shown in Fig. 5.1,
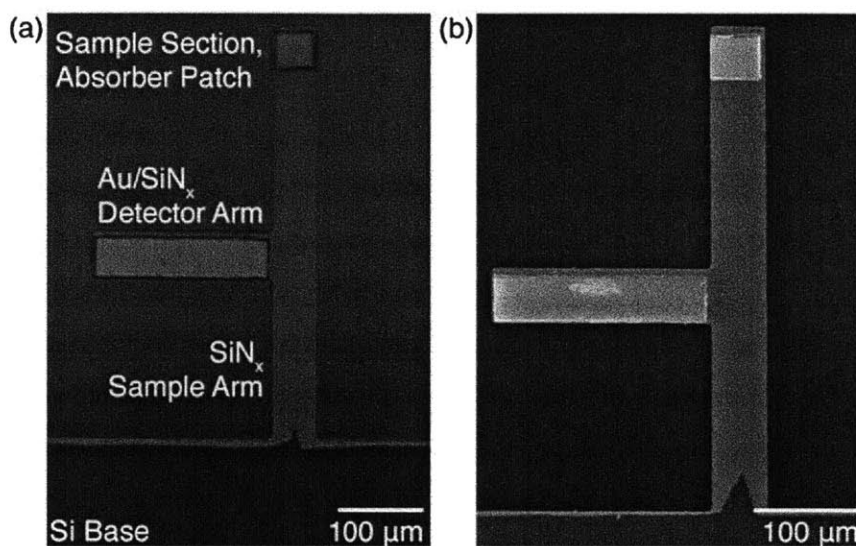

Figure 5.1: Images of the bi-arm cantilever which can be used to improve the sensitivity of the platform and to better isolate the sample from the detector arm. (a) An optical microscope image of the bi-arm cantilever. (b) A corresponding SEM image of the bi-arm cantilever.

By introducing a high thermal resistance between the detector arm and the base of the cantilever, the sensitivity improved by over one order of magnitude. The use of the sample arm can enable complete illumination of the sample and provide an easier means of attaching the sample to the cantilever. It is believed that by implementing these modifications, the system will have the sensitivity necessary to measure smaller samples.

Overall, this technique offers the advantages of direct and quantitative absorption characterization within the visible wavelength range and high sensitivity inherent in the detector. In addition, a newly proposed technique combining Fourier transform infrared (FTIR) spectroscopy and AFM cantilever thermometry was recently developed which spans the infrared wavelength range.[71] Ultimately, the hope is that the combination of these techniques will

provide a means of probing optical phenomena over a broad range of wavelengths which have been previously unattainable using conventional methods.

Bibliography

1. J. Valentine, J. Li, T. Zentgraf, G. Bartal, and X. Zhang, An optical cloak made of dielectrics. *Nat. Mater.*, 2009. **8**(7): p. 568-571.

2. R. Liu, C. Ji, J. J. Mock, J. Y. Chin, T. J. Cui, and D. R. Smith, Broadband Ground-Plane Cloak. *Science*, 2009. **323**(5912): p. 366-369.

3. V. M. Shalaev, Optical negative-index metamaterials. *Nat. Photon.*, 2007. **1**(1): p. 41-48.

4. N. Fang, H. Lee, C. Sun, and X. Zhang, Sub–Diffraction-Limited Optical Imaging with a Silver Superlens. *Science*, 2005. **308**(5721): p. 534-537.

5. M. H. Huang, S. Mao, H. Feick, H. Yan, Y. Wu, H. Kind, E. Weber, R. Russo, and P. Yang, Room-Temperature Ultraviolet Nanowire Nanolasers. *Science*, 2001. **292**(5523): p. 1897-1899.

6. C. Bohren and D. Huffman, *Absorption and Scattering of Light by Small Particles (Wiley science paperback series)* 1998: Wiley-VCH.

7. D. T. Phillips, P.J. Wyatt, and R.M. Berkman, Measurement of the Lorenz-mie scattering of a single particle: Polystyrene latex. *Journal of Colloid and Interface Science*, 1970. **34**(1): p. 159-162.

8. T. R. Marshall, C.S. Parmenter, and M. Seaver, Characterization of polymer latex aerosols by rapid measurement of 360° light scattering patterns from individual particles. *Journal of Colloid and Interface Science*, 1976. **55**(3): p. 624-636.

9. M. Bartholdi, G. C. Salzman, R. D. Hiebert, and M. Kerker, Differential light scattering photometer for rapid analysis of single particles in flow. *Appl. Opt.*, 1980. **19**(10): p. 1573-1581.

10. D. W. Schuerman, R. T. Wang, B. S. Gustafson, and R. W. Schaefer, Systematic studies of light scattering. 1: Particle shape. *Appl. Opt.*, 1981. **20**(23): p. 4039-4050.

11. C. Sönnichsen, T. Franzl, T. Wilk, G. von Plessen, J. Feldmann, O. Wilson, and P. Mulvaney, Drastic Reduction of Plasmon Damping in Gold Nanorods. *Physical Review Letters*, 2002. **88**(7): p. 077402.

12. A. D. McFarland, and R.P. Van Duyne, Single Silver Nanoparticles as Real-Time Optical Sensors with Zeptomole Sensitivity. *Nano Letters*, 2003. **3**(8): p. 1057-1062.

13. C. L. Nehl, N. K. Grady, G. P. Goodrich, F. Tam, N. J. Halas, and J. H. Hafner, Scattering Spectra of Single Gold Nanoshells. *Nano Letters*, 2004. **4**(12): p. 2355-2359.

14. C. L. Nehl, H. Liao, and J.H. Hafner, Optical Properties of Star-Shaped Gold Nanoparticles. *Nano Letters*, 2006. 6(4): p. 683-688.

15. G. Brönstrup, N. Jahr, C. Leiterer, A. Csáki, W. Fritzsche, and S. Christiansen, Optical Properties of Individual Silicon Nanowires for Photonic Devices. *ACS Nano*, 2010. 4(12): p. 7113-7122.

16. L. Cao, P. Fan, and M. L. Brongersma, Optical Coupling of Deep-Subwavelength Semiconductor Nanowires. *Nano Letters*, 2011. 11(4): p. 1463-1468.

17. L. Cao, J. S. White, J. Park, J. Schuller, B. M. Clemens, and M. L. Brongersma, Engineering light absorption in semiconductor nanowire devices. *Nat. Mater.*, 2009. 8(8): p. 643-647.

18. L. Cao, J. Park, P. Fan, B. Clemens, and M. L. Brongersma, Resonant Germanium Nanoantenna Photodetectors. *Nano Letters*, 2010. 10(4): p. 1229-1233.

19. H. T. Ng, B. Chen, J. Li, J. Han, M. Meyyappan, J. Wu, S. X. Li, and E. E. Haller, Optical properties of single-crystalline ZnO nanowires on m-sapphire. *Applied Physics Letters*, 2003. 82(13): p. 2023-2025.

20. P. Yang, H. Yan, S. Mao, R. Russo, J. Johnson, R. Saykally, N. Morris, J. Pham, R. He, and H. J. Choi, Controlled Growth of ZnO Nanowires and Their Optical Properties. *Advanced Functional Materials*, 2002. 12(5): p. 323-331.

21. M. S. Gudiksen, L. J. Lauhon, J. Wang, D. C. Smith, and C. M. Lieber, Growth of nanowire superlattice structures for nanoscale photonics and electronics. *Nature*, 2002. 415(6872): p. 617-620.

22. J. Qi, A.M. Belcher, and J.M. White, Spectroscopy of individual silicon nanowires. *Applied Physics Letters*, 2003. 82(16): p. 2616-2618.

23. T. K. Sham, S. J. Naftel, P. S. G. Kim, R. Sammynaiken, Y. H. Tang, I. Coulthard, A. Moewes, J. W. Freeland, Y. F. Hu, and S. T. Lee, Electronic structure and optical properties of silicon nanowires: A study using x-ray excited optical luminescence and x-ray emission spectroscopy. *Physical Review B*, 2004. 70(4): p. 045313.

24. L. Cao, B. Nabet, and J. E. Spanier, Enhanced Raman Scattering from Individual Semiconductor Nanocones and Nanowires. *Physical Review Letters*, 2006. 96(15): p. 157402.

25. L. Laffont, A. Lonjon, E. Dantras, P. Demont, and C. Lacabanne, Optical properties of metallic nanowires by valence electron energy loss spectroscopy. *Materials Letters*, 2011. 65(23–24): p. 3411-3414.

26. J. K. Gimzewski, C. Gerber, E. Meyer, and R. R. Schlittler, Observation of a chemical reaction using a micromechanical sensor. *Chemical Physics Letters*, 1994. 217(5–6): p. 589-594.

27. J. R. Barnes, R. J. Stephenson, M. E. Welland, C. Gerber, and J. K. Gimzewski, Photothermal spectroscopy with femtojoule sensitivity using a micromechanical device. *Nature*, 1994. **372**(6501): p. 79-81.

28. J. R. Barnes, R. J. Stephenson, C. N. Woodburn, S. J. O'Shea, M. E. Welland, T. Rayment, J. K. Gimzewski, and C. Gerber, A femtojoule calorimeter using micromechanical sensors. *Review of Scientific Instruments*, 1994. **65**(12): p. 3793-3798.

29. J. Lai, T. Perazzo, Z. Shi, and A. Majumdar, Optimization and performance of high-resolution micro-optomechanical thermal sensors. *Sensors and Actuators A: Physical*, 1997. **58**(2): p. 113-119.

30. J. Varesi, J. Lai, T. Perazzo, Z. Shi, and A. Majumdar, Photothermal measurements at picowatt resolution using uncooled micro-optomechanical sensors. *Applied Physics Letters*, 1997. **71**(3): p. 306-308.

31. M. C. LeMieux, M. E. McConney, Y. Lin, S. Singamaneni, H. Jiang, T. J. Bunning, V. V. Tsukruk, Polymeric Nanolayers as Actuators for Ultrasensitive Thermal Bimorphs. *Nano Letters*, 2006. **6**(4): p. 730-734.

32. S. Shen, A. Narayanaswamy, S. Goh, and G. Chen, Thermal conductance of bimaterial microcantilevers. *Applied Physics Letters*, 2008. **92**(6): p. 063509-3.

33. A. Narayanaswamy, and N. Gu, Heat Transfer From Freely Suspended Bimaterial Microcantilevers. *Journal of Heat Transfer*, 2011. **133**(4): p. 042401-6.

34. S. Sadat, Y. J. Chua, W. Lee, Y. Ganjeh, K. Kurabayashi, E. Meyhofer, and P. Reddy, Room temperature picowatt-resolution calorimetry. *Applied Physics Letters*, 2011. **99**(4): p. 043106-3.

35. O. Nakabeppu, M. Chandrachood, Y. Wu, J. Lai, and A. Majumdar, Scanning thermal imaging microscopy using composite cantilever probes. *Applied Physics Letters*, 1995. **66**(6): p. 694-696.

36. R. Berger, C. Gerber, J. K. Gimzewski, E. Meyer, and H. J. Guntherodt, Thermal analysis using a micromechanical calorimeter. *Applied Physics Letters*, 1996. **69**(1): p. 40-42.

37. G. Li, L. W. Burggraf, and W. P. Baker, Photothermal spectroscopy using multilayer cantilever for chemical detection. *Applied Physics Letters*, 2000. **76**(9): p. 1122-1124.

38. Z. Yang, H. Yan, S. Mao, R. Russo, J. Johnson, R. Saykally, N. Morris, J. Pham, R. He, and H. J. Choi, Optomechanical uncooled infrared imaging system: design, microfabrication, and performance. *Microelectromechanical Systems, Journal of*, 2002. **11**(2): p. 136-146.

39. A. Narayanaswamy, and G. Chen, Thermal near-field radiative transfer between two spheres. *Physical Review B*, 2008. **77**(7): p. 075125.

40. S. Shen, A. Henry, J. Tong, R. Zheng, and G. Chen, Polyethylene nanofibres with very high thermal conductivities. *Nat. Nano.*, 2010. **5**(4): p. 251-255.

41. K. Kjoller, J. R. Felts, D. Cooks, C. B. Prater, and W. P. King, High-sensitivity nanometer-scale infrared spectroscopy using a contact mode microcantilever with an internal resonator paddle. *Nanotechnology*, 2010. **21**(18): p. 185705.

42. B. Kwon, W. P. King, M. Schulmerich, and R. Bhargava, Mid-infrared thermomechanical sensitivity of microcantilevers for application to infrared spectroscopy. in *Sensors, 2010 IEEE.* 2010.

43. B. Kwon, M. Rosenberger, R. Bhargava, D. G. Cahill, and W. P. King, Dynamic thermomechanical response of bimaterial microcantilevers to periodic heating by infrared radiation. *Review of Scientific Instruments*, 2012. **83**(1): p. 015003-7.

44. M. Law, J. Goldberger, and P. Yang, Semiconductor Nanowires And Nanotube. *Annual Review of Materials Research*, 2004. **34**(1): p. 83-122.

45. L. Cao, P. Fan, E. S. Barnard, A. M. Brown, and M. L. Brongersma, Tuning the Color of Silicon Nanostructures. *Nano Letters*, 2010. **10**(7): p. 2649-2654.

46. Y. Huang, X. Duan, and C. M. Lieber, Nanowires for Integrated Multicolor Nanophotonics. *Small*, 2005. **1**(1): p. 142-147.

47. L. Hu, and G. Chen, Analysis of Optical Absorption in Silicon Nanowire Arrays for Photovoltaic Applications. *Nano Letters*, 2007. **7**(11): p. 3249-3252.

48. H. Ningfeng, L. Chenxi, and M. L. Povinelli, Broadband absorption of semiconductor nanowire arrays for photovoltaic applications. *Journal of Optics*, 2012. **14**(2): p. 024004.

49. L. Tsakalakos, J. Balch, J. Fronheiser, M. Shih, S. F. LeBoeuf, M. Pietrzykowski, P. J. Codella, B. A. Korevaar, O. V. Sulima, J. Rand, A. Davuluru, and U. Rapol, Strong broadband optical absorption in silicon nanowire films. *Journal of Nanophotonics*, 2007. **1**: p. 013552-10.

50. B. Tian, X. Zheng, T. J. Kempa, Y. Fang, N. Yu, G. Yu, J. Huang, and C. M. Lieber, Coaxial silicon nanowires as solar cells and nanoelectronic power sources. *Nature*, 2007. **449**(7164): p. 885-889.

51. E. C. Garnett, and P. Yang, Silicon Nanowire Radial p–n Junction Solar Cells. *Journal of the American Chemical Society*, 2008. **130**(29): p. 9224-9225.

52. J. B. Baxter, and E. S. Aydil, Nanowire-based dye-sensitized solar cells. *Applied Physics Letters*, 2005. **86**(5): p. 053114-3.

53. L. Vj, J. Oh, A. P. Nayak, A. M. Katzenmeyer, K. H. Gilchrist, S. Grego, N. P. Kobayashi, S. Y. Wang, A. A. Talin, N. K. Dhar, and M. S. Islam, A Perspective on Nanowire

Photodetectors: Current Status, Future Challenges, and Opportunities. *Selected Topics in Quantum Electronics, IEEE Journal of*, 2011. **17**(4): p. 1002-1032.

54. G. Mie, Beiträge zur Optik trüber Medien, speziell kolloidaler Metallösungen. *Annalen der Physik*, 1908. **330**(3): p. 377-445.

55. C. F. Bohren, How can a particle absorb more than the light incident on it? *American Journal of Physics*, 1983. **51**(4): p. 323-327.

56. D. H. Staelin, A. W. Morgenthaler, and J. A. Kong, *Electromagnetic Waves* 1994: Prentice Hall.

57. M. Auslender, and S. Hava, Chapter 6 - Doped n-Type Silicon (n-Si), in *Handbook of Optical Constants of Solids*, D.P. Edward, Editor 1997, Academic Press: Burlington. p. 155-186.

58. R. J. Roark, and W. C. Young, *Formulas for Stresses and Strain*. 5th Ed. ed1975, New York: McGraw-Hill.

59. S. Timoshenko, Analysis of Bi-Metal Thermostats. *J. Opt. Soc. Am.*, 1925. **11**(3): p. 233-255.

60. C. Wen-Hwa, M. Mehregany, and R. L. Mullen, Analysis of tip deflection and force of a bimetallic cantilever microactuator. *Journal of Micromechanics and Microengineering*, 1993. **3**(1): p. 4.

61. A. I. Hochbaum, R. Chen, R. D. Delgado, W. Liang, E. C. Garnett, M. Najarian, A. Majumdar, and P. Yang, Enhanced thermoelectric performance of rough silicon nanowires. *Nature*, 2008. **451**(7175): p. 163-167.

62. K. Q. Peng, Y. J. Yan, S. P. Gao, and J. Zhu, Synthesis of Large-Area Silicon Nanowire Arrays via Self-Assembling Nanoelectrochemistry. *Advanced Materials*, 2002. **14**(16): p. 1164-1167.

63. K. Peng, Y. Yan, S. Gao, and J. Zhu, Dendrite-Assisted Growth of Silicon Nanowires in Electroless Metal Deposition. *Advanced Functional Materials*, 2003. **13**(2): p. 127-132.

64. K. Peng, Y. Wu, H. Fang, X. Zhong, Y. Xu, J. Zhu, Uniform, Axial-Orientation Alignment of One-Dimensional Single-Crystal Silicon Nanostructure Arrays. *Angewandte Chemie International Edition*, 2005. **44**(18): p. 2737-2742.

65. A. Mavrokefalos,b T. M. Pettes, F. Zhou, and L. Shi, Four-probe measurements of the in-plane thermoelectric properties of nanofilms. *Review of Scientific Instruments*, 2007. **78**(3): p. 034901-6.

66. A. F. Mills, *Heat Transfer*. 2nd ed1999: Prentice Hall, Inc.

67. H. R. Philipp, Silicon Nitride (Si3N4) (Noncrystalline), in *Handbook of Optical Constants of Solids*, D.P. Edward, Editor 1985, Academic Press. p. 771-774.

129

68. D. W. Lynch, and W. R. Hunter, Comments on the Optical Constants of Metals and an Introduction to the Data for Several Metals, in *Handbook of Optical Constants of Solids*, D.P. Edward, Editor 1985, Academic Press. p. 286-295.

69. E. Collett, *Polarized light: fundamentals and applications* 1993: Marcel Dekker.

70. B. Burg, J. Tong, W. Hsu, P. Sambegoro, A. Mavrokefalos, and G. Chen, *Decoupled Cantilever Arms for Optomechanical Thermal Measurements*, 2012. 61/59947

71. W. Hsu, J. K. Tong, B. Liao, B. R. Burg, and G. Chen, *Direct and Quantitative Broadband Absorptance Spectroscopy of Small Objects with Multilayer Cantilever Probes*, 2012. 61/669715